Fully Coupled High-Resolution Atmosphere-Ocean-Wave Simulations of Hurricane Henri (2021): Implications for Offshore Load Assessments

Chunyong Jung[1], Pengfei Xue[1,2,3], Chenfu Huang[2,3], William Pringle[1], Mrinal Biswas[4], Geeta Nain[1,2], and Jiali Wang[1]

[1]Environmental Science Division, Argonne National Laboratory, Lemont, IL 60439, USA
[2]Department of Civil and Environmental Engineering, Michigan Technological University, Houghton, MI 49931, USA
[3]Great Lakes Research Center, Michigan Technological University, Houghton, MI 49931, USA
[4]National Center for Atmospheric Research, Boulder, CO 80310, USA

Correspondence to: Chunyong Jung (cjung2@anl.gov); Pengfei Xue (pexue@mtu.edu)

Abstract. ~~This study presents a fully coupled modelling system that integrates atmospheric, ocean, and wave models to simulate interactions during tropical cyclones and assess their implications for offshore infrastructure. The system is evaluated using Hurricane Henri (2021), chosen for its distinctive track along the U.S. northeast coast, an area with densely populated regions and offshore wind energy zones. The event is supported by extensive observations, including airborne Doppler radar, dropsondes, sea surface temperature, and ocean surface wave measurements. Three experiments with increasing complexity in atmosphere-ocean-wave coupled processes are conducted to examine their impact on storm intensity and development. Compared to atmospheric-only and atmosphere-ocean coupled simulations, the fully coupled model reduces intensity overestimations and improves the wind structure from near the surface to the upper troposphere. These improvements are due to realistic representation of complex feedback loops between the atmosphere, ocean, and waves. Wave-induced cooling of sea surface temperatures and reduced surface enthalpy flux mitigate intensity overestimation. Additionally, wave-driven surface roughness, reflected in realistic surface roughness length and drag coefficients, enhances the radial and vertical profiles of hurricane boundary layer winds. The fully coupled simulation shows promising potential for assessing risks to offshore infrastructure, featuring a more stable atmospheric boundary layer, weaker surface roughness, and lower turbulent kinetic energy. These factors allow wind veer to persist and align more closely with observations. The system also captures wind-wave misalignment, emphasizing the importance of incorporating ocean and wave components for accurate risk assessments in offshore infrastructure, such as wind turbine operations.~~

A new fully coupled modeling system, integrating atmosphere, ocean, and wave models, is presented to simulate intricate interactions during tropical cyclones and explore their potential implications for offshore infrastructure. The system is evaluated on Hurricane Henri (2021), chosen for its distinctive track along the U.S. northeast coast, an area of densely populated regions and offshore wind energy zones. Three simulation setups are compared: atmosphere-only, atmosphere–ocean, and a fully coupled atmosphere–ocean–wave model. Among them, the fully coupled model produces the most realistic results, improving not only the storm intensity near the surface but also the wind structure from the near surface to the upper atmosphere. Waves enhance ocean surface cooling with an additional 0.5 K reduction via non-breaking wave-induced vertical mixing and modify wind interactions through wave-driven surface roughness. This more realistic representation of coupled heat and energy exchanges between the atmosphere and ocean yield improved wind field patterns, which are critical for comprehensive risk assessment pertaining to offshore wind turbines. Furthermore, the coupled system reasonably captures wind-wave misalignment during the storm, with the greatest misalignment in the left-front and rear-left quadrants, while alignment occurs on the right side of the storm due to storm motion enhancing wave growth. These spatial variations highlight the need to accurately model atmosphere-ocean–wave interactions for reliable wind load assessments.

1 Introduction

Tropical cyclones (TCs) are among the costliest and deadliest natural hazards in the U.S., responsible for ~~pose a serious threat to society, bringing destructive winds, large waves, storm surges, heavy rainfall, and compound flooding. Over the past four decades (1980-2019), TCs have led U.S. disaster records, causing the highest economic losses (~~$945.9 billion~~)~~ in damages and ~~fatalities (~~6,502 from 1980 to 2019~~) among all natural hazards~~ (Smith, 2020). Although track forecasts have improved over recent decades, the ability to predict TC intensity remains ~~Climate warming further complicates TC behaviour, adding uncertainties: while TC frequency may remain stable or decline, TC intensity is likely to increase in many coastal areas, exacerbating coastal hazards and offshore energy harvesting (Knutson et al., 2010, 2019, 2020; Walsh et al., 2015, 2016; Wang et al., 2024a,b). Consequently, accurate TC prediction has become increasingly essential for effective risk analysis, disaster prevention, and infrastructure design.~~

~~Forecasting TC tracks has improved substantially over the past few decades, while predicting TC intensity remains challenging and has shown only~~ limited ~~progress~~ (DeMaria et al., 2014; Rappaport et al., 2009; Yamaguchi et al., 2017; Zao et al., 2022). A key limitation lies in the incomplete representation of atmosphere-ocean interactions in models, particularly storm-induced sea surface temperature (SST) cooling ~~Previous studies suggested that insufficient consideration of the physical processes and their subsequent heat and momentum exchanges at the atmosphere-ocean interface might be responsible for the slower progress in improving TC intensity forecasts compared to track forecasts over the decades~~ (DeMaria et al., 2007; Zhao et al., 2017, 2022). This cooling is primarily driven by vertical mixing processes caused by strong TC-generated waves, intense upper-ocean shear, and upwelling associated with divergent ocean currents (Emanuel, 1986; Schade and Emanuel, 1999; Wu et al., 2016).

While many studies have explored TC dynamics using fully coupled atmosphere-ocean-wave models (e.g., Chen et al., 2007; Fan et al., 2009; Zhao et al., 2017, 2022), few have extended these frameworks to the domain of offshore wind energy risk assessment. Despite the significant impact of air-sea interactions on surface fluxes and hurricane wind structure, they are often overlooked in applied wind energy assessments and design studies conducted under hurricane conditions (e.g., Arthur, 2021; Chen et al., 2024; Roldán et al., 2023; Sanchez Gomez et al., 2023). This simplification can result in inaccurate representations of wind loading and an underestimation of structural vulnerabilities.

One critical gap in current hurricane-focused offshore wind assessments is the impact of wind-wave misalignment on structural loads and potential damage. Such misalignment can significantly increase side-to-side turbine deflections and lead to underestimations of fatigue loads by as much as 50% in floating systems. For instance, a recent study by Shanahan and Fitzgerald (2025) found that wind-wave misalignment in floating offshore wind turbines can exceed 30° during hurricanes and reach up to ~58° along exposed western coastal zones of Ireland. Additionally, Ma and Sun (2023) used large-eddy simulations to model the coupled wind-wave loading on fixed-bottom offshore turbines, finding that under extreme events, such as hurricanes, aerodynamic loading increases: the mean bending moment at both tower and monopile rises by ~6%, the standard deviation of shear force increases by up to ~45%, and the bending movement variability increases by ~27%. These findings highlight the need for dynamic, coupled modeling approaches that can capture the evolving interactions among wind, waves, and currents, especially under extreme events, such as hurricanes (e.g., Chen et al., 2013; Barr and Chen., 2025). However, most current modeling frameworks used for wind energy risk assessment fall short in this regard. Uncoupled atmospheric models typically calculate surface roughness solely based on wind speed (e.g., via Charnock formulations), neglecting wave-induced momentum fluxes (e.g., Sanchez Gomez et al., 2023), which can bias near-surface wind fields, shear profiles, and wind veer under extreme forcing. Statistical–parametric models, while efficient for probabilistic loss estimation, represent hurricane winds using idealized radial wind profiles—such as studies that use the classic Holland model (Arthur, 2021), the two-parameter Holland formulation (Chen et al., 2024), or recent asymmetric extensions (Roldán et al., 2023). By neglecting the evolving feedback among wind, waves, and ocean currents, these approaches can underpredict or overpredict extreme gusts and rapid directional shifts that critically drive turbine loading.~~For example, Mogensen et al. (2017) and Wei et al. (2017) suggest that sea surface temperature (SST) cooling feedback process in TC modelling is a major factor contributing to bias in TC intensity forecasts. The storm extracts energy from the ocean through exchanges of heat, moisture, and momentum fluxes at the atmosphere and ocean interface. TC-driven high winds and waves enhance turbulent mixing in the upper ocean, resulting in SST cooling—often called "cold wakes"—along the storm's path. This process acts as negative feedback on storm energetics by reducing the surface enthalpy flux supply (Bender et al., 1993; Cavaleri et al., 2012; Cione and Uhlhorn, 2003; Fan et al., 2010; Schade and Emanuel, 1999). For instance, Zhu and Zhang (2006) found that cooling in SST, averaging -1.3 °C near the TC centre and along its track, statistically weakens hurricane intensity by about 25 hPa. This feedback mechanism between the atmosphere and ocean is primarily driven by vertical mixing of cooler waters from beneath the seasonal thermocline,~~

~~induced by TC-generated strong waves, large upper-ocean shears, and upwelling from divergent ocean currents (Emanuel, 1986; Schade and Emanuel, 1999; Wu et al., 2016). The reduced surface heat exchange then weakens the moist enthalpy flux from the ocean to the atmosphere, thereby diminishing TC intensity. Therefore, to realistically capture TC-induced SST cooling, the atmospheric forecast model must be coupled with a three-dimensional ocean model (e.g., Yablonsky and Ginis, 2009).~~

To address these limitations,

~~Another key ocean element in TC evolution involves ocean surface waves, which significantly affect both atmospheric and ocean dynamics. As for the impact of the waves on atmospheric dynamics, on the one hand, ocean surface waves characterize surface roughness, influencing the structure of atmospheric and marine boundary layers. This, in turn, affects atmosphere-ocean momentum and heat exchanges, upper-ocean mixing, sea spray production, and albedo (Cavaleri et al., 2012). Liu et al. (2011) found that their satellite-based latent heat flux data (XseaFlux) performed significantly better in capturing TC-associated latent heat flux by incorporating sea surface wave features such as wave breaking, wave orbital motion (non-breaking waves), and sea spray. Chen et al. (2007, 2013) emphasized the importance of wind-wave feedback under extreme conditions through directional wind-wave coupling, which enhances simulations of hurricane-induced surface winds and hurricane structure. Similarly, Zhao et al. (2017, 2022) found that wave-induced processes, including mixing and sea spray production, reduce biases in TC intensity forecasts, underscoring the essential role of ocean surface waves in atmosphere-ocean enthalpy flux exchanges and TC evolution. On the other hand, breaking waves also generate sea spray, which enhances atmosphere-ocean heat and moisture flux exchanges under tropical cyclone (TC) conditions, potentially intensifying TCs (Perrie et al., 2004, 2005; Richter and Stern, 2014; Zhao et al., 2022). However, Prakash et al. (2019) found that incorporating sea spray has only a marginal effect on storm intensity, suggesting that wave impacts on surface roughness may play a more significant role in the coupling process. This relative importance, however, requires further investigation with additional storm cases, as will be discussed in Section 6.~~

~~As for the impact of the waves on ocean dynamics, wave-induced mixing—driven by both breaking and non-breaking waves plays a key role in modulating SST, which is critical for TC development and intensity (Babanin, 2006; Qiao et al., 2004; Sullivan and McWilliams, 2010). Breaking waves create surface-level turbulence, but kinetic energy dissipates quickly with depth, limiting their influence on SST and surface heat fluxes (Craig and Banner, 1994; Zhang et al., 2007). In contrast, non-breaking waves penetrate deeper, significantly affecting SST and mixed layer depth, both of which are essential for TC intensity modification (Babanin et al., 2009; Qiao et al., 2004; Zhang et al., 2022). Additionally, waves influence the bottom boundary condition for TCs through wave-current interactions, affecting sea surface currents (Lane et al., 2007; Mellor, 2016; Olabarrieta et al., 2010; Smith, 2006) and SST through mechanisms such as radiation stress, Stokes drift, and vertical mixing (Wang et al., 2024b). Coupled wind-wave-ocean models underscore the significant impact of wind-wave-current interactions on atmosphere-ocean momentum flux and ocean responses in TCs (Fan et al., 2009).~~

~~Grid spacing is another critical factor being continually addressed as computational resources increase over time. Resolving the inner core of a TC with a grid spacing of 4 km or less has enabled the explicit representation of deep convection, leading to a more accurate depiction of TC structure in the atmospheric component (e.g., Gentry and Lackmann, 2010). In an atmosphere-ocean coupling framework, Tsartsali et al. (2022) emphasized that optimal results require higher resolutions in both ocean and atmospheric models, specifically at least eddy-permitting (~25 km) and better eddy-resolving (~8 km) ocean resolution, along with comparable atmospheric resolution, for reliable atmosphere-ocean coupling along the Gulf Stream. Additionally, Zhang et al. (2023) employed the Community Earth System Model at very high spatial resolutions (up to 3 km for the ocean and 5 km for the atmosphere) to capture major weather and climate extremes, highlighting the importance of convection-permitting resolution and sub-mesoscale ocean eddies in modelling TC dynamics and eddy-mean flow interactions.~~

~~T~~this study introduces a newly developed atmosphere-ocean-wave coupled modelling system that integrates a regional atmospheric climate model with ocean and surface wave models, both of which operate on a high-resolution unstructured mesh. This framework, while sharing similarities with the Coupled Ocean Atmosphere Wave and Sediment Transport (COAWST, Warner et al., 2010), is distinguished by several key enhancements. First, it supports regional mesh refinement, allowing ultra-high resolution ocean grids over targeted areas such as offshore wind farms. This feature provides more localized and detailed oceanic information, improving the system's utility for site-specific assessment. Second, our framework explicitly includes the effects of non-breaking wave processes in the coupling system. These processes, which require custom implementation (e.g., Xu et al., 2023), are not part of the standard COAWST model but are essential for realistically representing atmosphere-ocean-wave interactions, especially under extreme wind conditions such as those associated with TCs. ~~model in its coupled components, distinguishes itself through its ability to provide regional refinement over areas of interest (e.g., offshore wind farms). Its capability to generate ultra-high spatial resolution for the ocean mesh allows for more detailed and localized information, enhancing its applicability for site-specific analyses. In addition, we incorporate the impacts of non-breaking waves into the coupling system to enable more realistic interactions between the atmosphere, ocean, and waves. Utilizing this fully coupled system at a very high resolution (3 km for the atmosphere and 3 km for the ocean and wave models near the U.S. Northeast Coast), we investigate the effects of atmosphere-ocean-wave three-way feedback on tropical cyclone (TC) development and demonstrate its relevance in assessing potential TC-induced risks for offshore wind infrastructure. The model presented here provides a more realistic depiction of the complex interactions between the ocean, waves, and atmosphere compared to many existing statistical-parametric models (e.g., Arthur, 2021; Chen et al., 2024; Roldán et al., 2023) and idealized TC models (e.g., Sanchez Gomez et al., 2023), which often analyse wind and wave interactions separately or exclude them altogether. These limitations may result in incomplete risk assessments, as wave dynamics play a substantial role in TC behaviour and evolution, as previously discussed.~~

We apply this fully coupled system at high resolution (3km for both atmospheric and oceanic components near the U.S. Northeast Coast) to evaluate the impact of intercomponent coupling feedback on TC development, with a focus on the near-surface and lower boundary layer wind field. In this study, we selected Hurricane Henri (2021) to demonstrate the capabilities of the coupled system, providing insights into the role of wave dynamics in atmosphere-ocean modeling and their influence on storm wind structure, with a particular focus on processes at the air-sea interface and within the planetary boundary layer. Henri was a Category 1 storm that made landfall in Rhode Island on 22 August 2021. Despite its weak intensity, Henri caused heavy rainfall, flooding, and power outages across the densely populated Northeast U.S., including New York and Boston. It also passed through the offshore wind energy lease area on the northeast continental shelf. Extensive observations, including airborne Doppler radar and dropsonde data near the eyewall, enable direct comparison between modeled and observed storm structures to assess model performance and atmosphere-ocean-wave coupling.

The development of the model, including detailed information on each model component and the coupler, is described in Section 2. Section 3 describes the experimental design and data used for model validation using Hurricane Henri (2021) as a working example. In Section 4 and 5, we present results and analysis, followed by the summary and discussions ~~. Implications for potential risks to offshore wind energy is discussed in Section 5, followed by the summary and discussions~~ in Section 6.

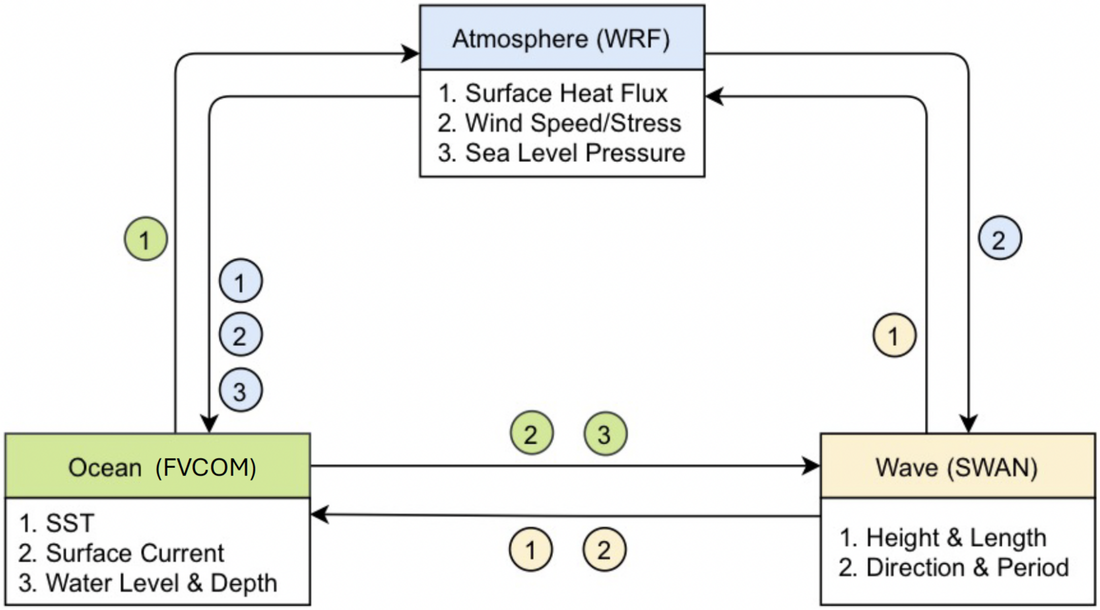

Figure 1. Schematic of coupled atmosphere-ocean-wave system and modelling used in this study.

2 Model Description

The coupled atmosphere-ocean-wave modeling~~ modelling ~~ system consists of three components: the Weather Research and Forecasting (WRF) model for atmospheric processes (WRF V4.5.1; Skamarock et al., 2019), the Finite Volume Community Ocean Model (FVCOM) for ocean circulations (V4.3.1; Chen et al., 2003, 2013)~~ for ocean circulations~~, and the third-generation Simulating WAves Nearshore (SWAN) ~~model ~~for wave dynamics (Booij et al., 1999), with data~~ and a coupler to~~ exchanged via a coupler~~ data fields~~ (Fig. 1). Hereafter, we refer to the coupled WRF-FVCOM-SWAN model as C-WFS. These components run in parallel and interact through the OASIS3-MCT coupler (Craig et al., 2017). Details on each model, recent improvements, and the coupling strategy are provided in Sections 2.1–2.2.

~~Hereinafter, we refer to the coupled WRF-FVCOM-SWAN model as C-WFS. In the three-way coupled framework of C-WFS, the model components are executed in parallel, exchanging information through the Ocean Atmosphere Sea Ice Soil3 (OASIS3)-Model Coupling Toolkit (MCT) coupler (Craig et al., 2017). We describe each component, improvements made to them, and the approach to coupling in Sections 2.1-2.2.~~

2.1 Model Components

WRF is a nonhydrostatic, quasi-compressible atmospheric model featuring boundary layer physics and various ~~with boundary layer physics schemes and a variety of physical parameterizations of ~~sub-grid scale parameterizations to simulate ~~processes for predicting ~~meso- and macroscale motions~~s of motion~~. In this study, we ~~WRF has been extensively used for operational forecasts as well as for realistic and idealized research experiments. We have ~~modified the WRF code to incorporate the ~~enable the ~~wave slope-based sea surface roughness formulation from Taylor and Yelland (2001) into several surface schemes, including~~ several surface schemes (~~MYNN (~~[~~Nakanishi and Niino, 2009; Olson et al., 2019~~]~~,) and both the original and revised MM5 schemes ~~[~~(Dyer and Hicks, 1970; Jimenez et al., 2012; Paulson, 1970; Webb, 1970~~]~~):

$$Z_0 = 1200 H_s \left(\frac{H_s}{L_p}\right)^{4.5} + \frac{0.11\upsilon}{u_*} \qquad Z_0 \le 0.00285 \tag{1}$$

where Z_0 is the surface roughness length, H_s is the significant wave height, L_p is the wavelength at the peak of spectrum, υ is kinematic viscosity, and u_* is the friction velocity. Although C-WFS includes alternative ~~Other ~~wave-based formulations (e.g., Drennan et al., 2003; 2005), our tests showed that the ~~ are also available in C-WFS but in our testing we found that the ~~capped Taylor and Yelland (2001) method yielded the optimal ~~gave the best ~~performance for our case study.

The ocean ~~model ~~component, FVCOM (V4.3.1), is a ~~prognostic, free-surface, ~~3-D, free-surface, ~~D~~prognostic~~ primitive equation~~ coastal ~~ocean ~~circulation model solves the primitive equations on ~~that is numerically solved over ~~an unstructured triangular grid using the finite-volume method. It enables dynamic interaction between ocean and atmospheric conditions throughout the simulation. In this study, we ~~Version 4.3.1 of FVCOM is used in this study, allowing ocean hydrodynamic conditions to interact freely with atmospheric conditions throughout the simulation period. We~~ modified ~~the~~ FVCOM ~~code~~ to include~~corporate~~ vertical mixing induced by ~~effects induced by~~ non-breaking waves, by adding a wave-related term to the ~~. Non-breaking wave induced mixing is added to the~~ turbulence eddy diffusivity B_v~~.~~, following ~~included in the ocean model and is expressed as (~~Ghantous and Babanin~~,~~ (2014a,b) and ~~;~~ Aijaz et al. (2017):

$$B_v = \alpha A^3 \kappa \sigma e^{3\kappa z} \tag{2}$$

where $\alpha = 0.1$, A = wave amplitude ($H_s/2$), κ = wave number (2π/L), σ= peak wave frequency ($1/T_p$), z is water depth.

The wave model component, SWAN v41.01, is a third-generation spectral wave model developed at Delft University of Technology that computes random, short-crested wind-generated waves in coastal regions and inland waters (http://swanmodel.sourceforge.net/). It solves the evolution equation of wave action density in space time, frequency and wave direction dimensions (Pringle and Kotamarthi, 2021). Various wave energy sources and sinks are modelled, including wave generation by wind, wave decay due to whitecapping, bottom friction, depth-induced wave breaking, and energy redistribution through nonlinear wind-wave interactions.

2.2 Coupler and Coupling

OASIS3-MCT is a parallelized coupler that synchronizes ~~enables the simultaneous coupling of~~ 2-D and 3-D field exchanges~~s~~. Figure 1 outlines the ~~provides a schematic illustration of the~~ C-WFS coupling framework and ~~, detailing the quantities~~ exchanged variables~~within the coupling framework~~. WRF provides FVCOM with surface forcing—including friction velocity, winds, sea level pressure, heat fluxes, and radiation fluxes—while receiving SST from FVCOM as over-ocean boundary conditions. WRF also supplies wind fields to SWAN for wave simulations. In return, SWAN sends significant wave height and peak wavelength to WRF, which uses them to calculate sea surface roughness based on Equation 1. FVCOM uses wave fields from SWAN to compute radiation stress gradients, Stokes velocities, wave-enhanced bottom stresses, and non-breaking wave-induced mixing; breaking wave mixing is included via stress gradients. FVCOM also provides surface currents to SWAN, enabling Doppler shift effects from currents on wave behavior. This integrated coupling improves wave prediction accuracy by capturing wave-current interactions more realistically.

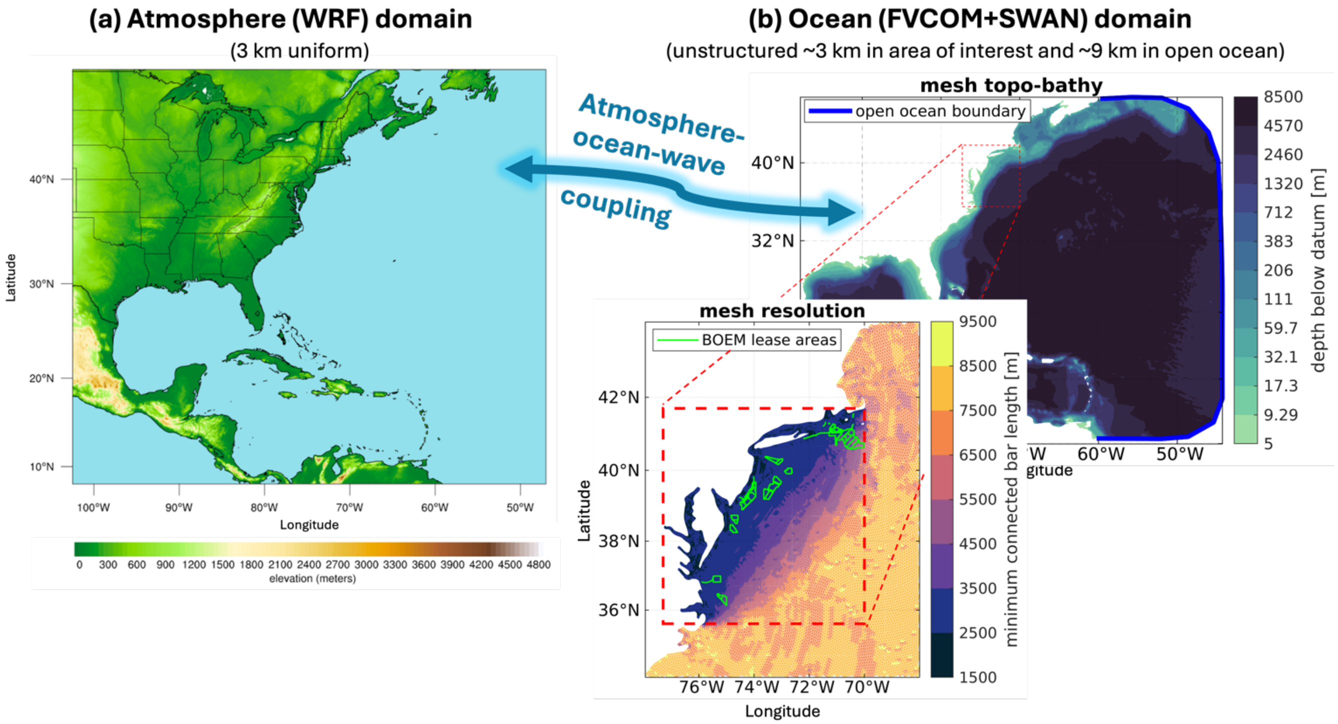

Figure 2. (a) WRF model domain with terrain height elevation, and (b) FVCOM and SWAN domain with bathymetric depths and a zoom-in to the refined mesh grid along the northern U.S. East Coast and BOEM offshore lease areas.

~~The friction velocity, surface winds, sea level pressure, latent and sensible heat fluxes, and shortwave and longwave radiation fluxes predicted by WRF are transferred to FVCOM as surface forcing, while FVCOM provides sea surface temperature (SST) to WRF as over-ocean boundary conditions. WRF supplies wind fields to drive SWAN for wave simulation, while SWAN provides significant wave height and wavelength at the peak of the spectrum to WRF, which uses them to calculate sea surface roughness based on equation (1). The wave fields are used by FVCOM to compute radiation stress gradients, enabling wave-driven flows, Stokes velocities for mass flux transport, wave-enhanced bottom stresses, and non-breaking wave-induced mixing. Breaking wave-induced mixing is incorporated as a part of radiation stress gradients. Additionally, FVCOM provides sea surface currents to SWAN, allowing for the inclusion of Doppler effects from background currents on surface waves. This integration enables SWAN to better account for how ocean current movement affects wave behaviour, resulting in more accurate wave predictions.~~

3 Application of C-WFS Modelling System

~~This section describes the C-WFS setup used to simulate Hurricane Henri (2021). Henri reached Category 1 on the Saffir-Simpson scale and made landfall in Rhode Island, U.S. on 22nd August 2021. Despite its relatively weak intensity, the storm brought very heavy rainfall over the Northeastern U.S., including New England, causing widespread flooding and power~~

~~outages in the densely populated regions, such as New York and Boston. Moreover, Henri is one of the recent TCs to pass through the offshore leased wind energy area in the U.S. northeast continental shelf. During this hurricane, comprehensive observation datasets were collected, including airborne measurements such as doppler radars and dropsondes that reached the eyewall and core. These conditions and datasets allow for direct comparisons between the modelled and observed TC structures, providing insights into model performance and the coupling effects due to atmosphere-ocean-wave interactions.~~

3.1 Experimental Design and Configuration

To evaluate~~explore~~ the integrated impact of ~~effects of~~ ocean and wave~~ocean surface wave related physical~~ processes on TC simulations, three experiments were ~~a set of three model simulations is~~ performed. Experiment ‘A’ (atmosphere only) uses WRF ~~standalone simulation is named as experiment ‘A’, in which the event is modelled using WRF alone with prescribed SST at~~with 6-hourly updated SST~~ intervals~~. ~~In experiment~~ ‘AO~~,~~’ couples WRF ~~is coupled~~ with FVCOM, enabling atmosphere-ocean interaction but no wave effects. ~~variable exchange as shown in Fig. 1, but without considering ocean surface wave-related physical processes. Experiment~~ ‘AOW’ fully couples ~~is a multi-way fully coupled experiment, in which~~ WRF, FVCOM, and SWAN via ~~exchange variables with each other every hour through the~~ OASIS3-MCT, allowing hourly multi-way atmosphere-ocean-wave exchanges~~Coupler to allow direct and indirect atmosphere-ocean-wave interactions, as discussed in Section 2~~.

WRF is configured with a 3 km ~~All simulations are initialized at 18:00 UTC on August 19, 2021, within a domain encompassing the western North Atlantic Ocean. The atmospheric domain features a~~ horizontal resolution and 46 vertical levels (12 below 100 m), covering much of the North Atlantic basin ~~of 3 km~~ (Fig. 2a). It uses ~~The ocean domain, which covers a substantial portion of the WRF ocean domain, employs an unstructured triangular grid with resolutions ranging from 3 km near the coast to 9 km in the open ocean, effectively resolving the complex coastline of the U.S. Northeast Coast (Fig. 2b). Initial and boundary conditions for the atmosphere model are obtained from the~~ 6-hourly 0.25° NCEP (National Centers for Environmental Prediction) Global Forecast System (GFS; NCEP, 2015) analysis data for atmospheric initial and boundary condtions, with SSTs prescribed from GFS in ‘A’. The model employs ~~. Note that the prescribed SST for experiment ‘A’ is provided by GFS at 6-hourly intervals. The atmosphere is represented by 46 stretched vertical levels topped at 50 hPa with 12 layers below 100 metres. The physics selected for this study include the WRF single-moment 6-class microphysics scheme (~~WSM6 microphysics~~;~~ (Hong and Lim, 2006), RRTM radiation ~~the Rapid Radiative Transfer Model for GCMs longwave and shortwave schemes~~ (Iacono et al., 2008), ~~the~~ Yonsei University PBL (Hong et al., 2006), and the Eta similarity surface layer scheme ~~which is based on the revised MM5 Monin-Obukhov scheme~~ (Jimenez et al., 2012). ~~The land surface processes are modelled by the Noah (Chen and Dudhia, 2001).~~ No cumulus parameterization~~s~~ is~~are~~ used, as ~~in our WRF setup, as previous studies have demonstrated that a resolution of~~ 4 km resolution or less supports ~~is adequately~~ convection-permitting simulations ~~in WRF for simulating extreme events~~ (Akinsanola et al., 2024; Kouadio et al., 2020; Qing and Wang, 2021; Sun et al., 2016).

The ocean domain (FVCOM) covers most of the WRF domain, with horizontal resolution ranging from ~9 km in the open ocean to ~3 km over the continental shelf. It uses 40 sigma vertical layers to capture steep coastal bathymetry. Vertical mixing processes are simulated using the Mellor–Yamada level-2.5 (MY25) turbulence closure model (Mellor and Yamada, 1982), and horizontal diffusivity is computed using the Smagorinsky numerical formulation (Smagorinsky, 1963). Initial and boundary conditions for currents, temperature, salinity, and water level are provided by 1/12° HYCOM (Hybrid Coordinate Ocean Model) analysis data (Cummings and Smedstad, 2014).

The wave model domain matches the FVCOM domain, using ~12 km horizontal resolution. The wave spectrum is divided into 36 directional and 24 frequency bins (0.04–1 Hz). Wave physics include Komen et al. (1984) for growth and whitecapping, Madsen et al. (1988) for bottom friction, and a constant depth-limiting breaker index, all with default settings. Swell boundary conditions are omitted due to minimal impact at the eastern boundary, and the model is initialized from a quiescent state.

All experiments were initialized at 18:00 UTC on 19 August, 2021, and simulated for 102 hours. Nudging techniques were intentionally omitted to better isolate the effects of atmosphere–ocean–wave coupling on TC characteristics. Additional tests using various physics schemes and forcing datasets (e.g., ERA5) confirmed the robustness and low sensitivity of the results to model configuration choices, although the supporting results are not presented in this manuscript.

~~Initial conditions for the ocean model fields of currents, water level, salinity, and temperature and boundary conditions for currents, salinity, and temperature are derived from the (1/12)°×(1/12)° resolution HYbrid Coordinate Ocean Model (HYCOM; Cummings and Smedstad, 2014) analysis data (http://hycom.org/dataserver/) simulations. The ocean domain employs varying horizontal resolution of ~9 km in the open ocean down to ~3 km over the continental shelf in the area of interest (Fig. 2b). The ocean is represented vertically with 40 sigma layers, enabling the model to accurately reflect the abrupt changes in coastal bathymetry. Vertical mixing processes are simulated using the Mellor–Yamada level-2.5 (MY25) turbulence closure model (Mellor and Yamada, 1982), and horizontal diffusivity is computed using the Smagorinsky numerical formulation (Smagorinsky, 1963).~~

~~For this study, the wave model domain covers the same geographic extent as the FVCOM domain with approximately 12 km horizontal resolution. The wave spectrum is discretized into 36 directional bins and 24 frequency bins on the interval [0.04,1] Hz. We use Komen et al. (1984) wave growth and whitecapping physics, Madsen et al. (1988) bottom friction, and a constant depth-limiting wave breaker index, all with their default parameters. Lateral boundary conditions for swell are not applied due to their insignificance at the eastern boundary.~~

~~All experiments involved a 102-hour integration, initialized from the same conditions at 18:00 UTC on August 19, 2021. Following initialization, the simulations evolved freely throughout the entire 102-hour hindcast period without any technical interventions. While nudging techniques, such as spectral nudging of variables such as wind, air temperature, and geopotential height, are valuable for improving modelled tracks, they were intentionally not applied in this study. This decision reflects the focus on exploring the impacts of multi-factor coupling between the atmosphere, ocean, and waves on tropical cyclone (TC) characteristics. Applying nudging could complicate efforts to isolate the specific coupling effects of ocean and wave processes on TC behaviour.~~

~~Several additional simulations were conducted using different planetary boundary layer and microphysics parameterizations, as well as various forcing data (e.g., ERA5 reanalysis data, the fifth generation of ECMWF atmospheric reanalyses of the~~

~~global climate). The results consistently showed that the overall conclusions of this study remained unchanged, demonstrating the robustness of the findings and their low sensitivity to these configuration choices.~~

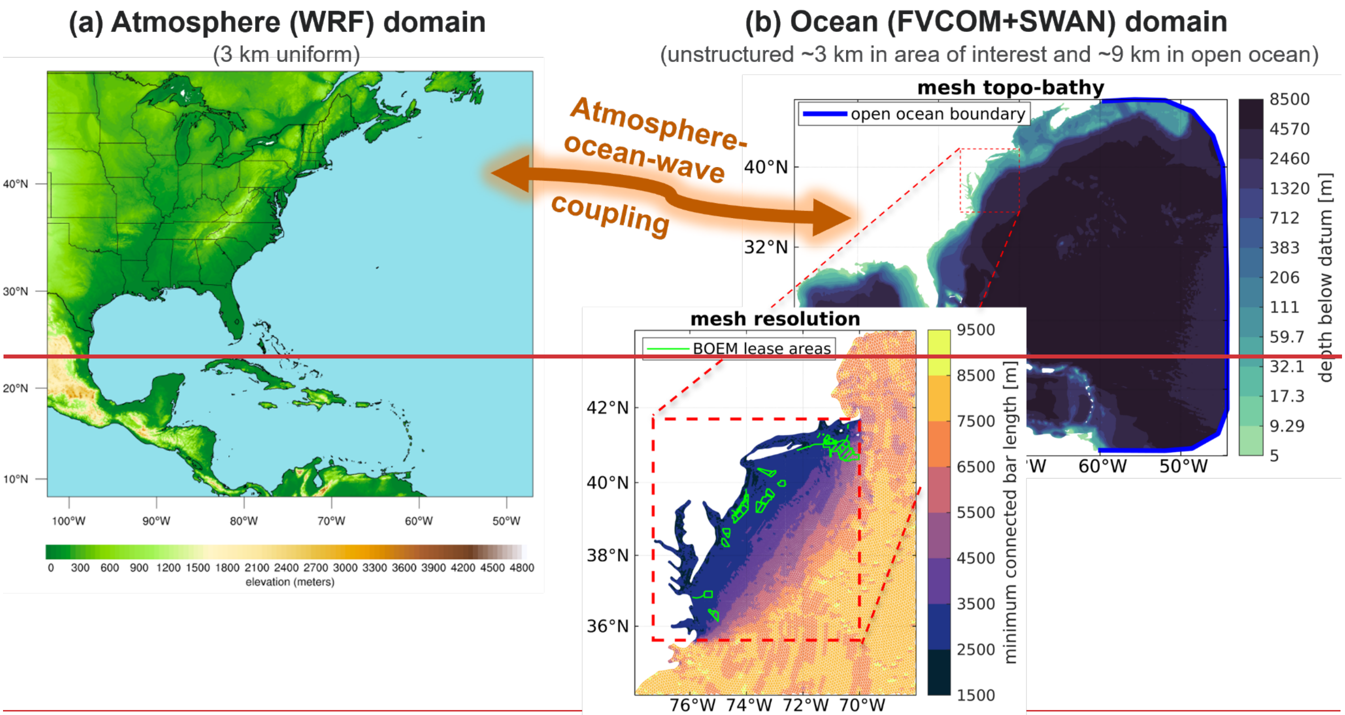

~~**Figure 2. (a) WRF model domain with terrain height elevation, and (b) FVCOM and SWAN domain with bathymetric depths and a zoom-in to the refined mesh grid along the northern U.S. East Coast and BOEM offshore lease areas.**~~

3.2 Method and Data

~~The ~~M~~m~~odel results are evaluated against several observational~~s~~ ~~using multiple~~ datasets, including International Best Track Archive for Climate Stewardship (IBTrACS; Knapp et al., 2010), which provides TC position, minimum sea level pressure (SLP), and maximum 10-m sustained winds at ~~and airborne observations. IBTrACS is the most complete global collection of TCs, providing TC best position, minimum sea level pressure (SLP), maximum sustained wind speeds, and translation speed at mostly~~ 6-hour~~ly~~ intervals, and airborne observations. ~~.~~The airborne ~~observations~~ data include the Tropical Cyclone Radar Archive of Doppler Analyses with Recentering (TC-RADAR; ~~) dataset (~~Fischer et al., 2022) and dropsondes from NOAA's Hurricane Research Division. ~~aircraft provided by the National Oceanic Atmospheric Administration's (NOAA) Hurricane Research Division (HRD).~~ TC-RADAR contains ~~is a comprehensive database of airborne observations of TCs, featuring data from the~~ X-band ~~tail~~ Doppler radar data from~~on~~ NOAA's WP-3D aircraft, scanning ~~. This radar scans~~ in ~~both~~ front and back directions to produce ~~, enabling~~ detailed 3-D analyses of ~~the inner-core structure of~~ TC inner-core structure.~~s. Typically, e~~Each mission typically includes 3-4 center passes, with storm-centered "cecentering" techniques used to generated ridded analyses. ~~through the centre of the storm. For each central pass, an analysis is created using a technique called "recentring," which~~

~~provides analyses on storm-cantered grids.~~ Our simulations adopt the same storm-cantered coordinates for direct comparison. ~~We utilize storm-centred coordinates for our simulations, aligning the grids of TC-RADAR to enable direct comparison of the 3-D storm structure between the simulations and TC-RADAR. To align with the storm-centred grids of the TC-RADAR analyses, a~~A 300 km × 300 km grid is centered on the grid cell with minimum SLP in each dataset. To fill the 0~~–~~ ~~box is centered on the grid cell with the minimum SLP in each dataset. To provide seamless observations from the surface up to~~ 0.5 km altitude gap not captured by radar, we include dropsonde data. Due to slight differences in storm track and speed between the model and ~~— the range not covered by TC-RADAR — we use dropsonde data as well. In this study, the model generates tracks and translational speeds that differ slightly from the~~ observations (Fig. 3), ~~.~~ dropsonde positions are adjusted relative to the storm center (e.g., Creasey and Elsberry, 2017). Seven dropsondes (shown in Fig. 3d) from a single flight across the storm center were selected fro evaluation; this flight crossed the storm from east to west within 50 minutes from from 23:21 UTC on 21 to 00:11 UTC on 22 August 2020 (with exact times indicated in Fig 3d), 12 hours before peak intensity.

~~Therefore, the positions of the dropsondes are adjusted relative to the storm centre rather than using their actual deployment locations. Here, we selected the seven dropsonde observations shown as blue and colour dots in Fig. 3d for the assessment because they were deployed from a single flight across the storm centre. This flight spanned from the eastern to the western edge within 50 minutes, just 12 hours before the storm reached its peak intensity.~~

Modelled ocean surface waves are compared with observations from two National Data Buoy Center (NDBC; NDBC, 2008) buoys, 41001 and 41002, located on the left of the storm track on the continental slope. While there are more buoy locations, our focus is on the variation of storm-induced winds and waves along Henri's track. We exclude stations near the U.S Northeast Coast due the models' track bias after 22nd August (more discussion in Section 4). The buoy data provides surface wind and wave information, including surface wind speed, significant wave height, and peak wave period and direction. In addition to in-situ NDBC buoy measurements, we compiled a series of daily SST data from the Operational Sea Surface Temperature and Ice Analysis (OSTIA; Good et al., 2020) at 0.05° × 0.05° resolution to determine the pre- and post-storm environment as well as the difference between them.

The radius of maximum wind (RMW) defines the location of the maximum winds in a TC and is critical to understanding intensity change as well as hazard impacts. In this study, we azimuthally average the vertical profiles of the seven dropsondes and the simulations of wind speed relative to RMW to define the areas within and beyond the eyewall, allowing for a detailed comparison of the storm's inner- and outer-core regions.

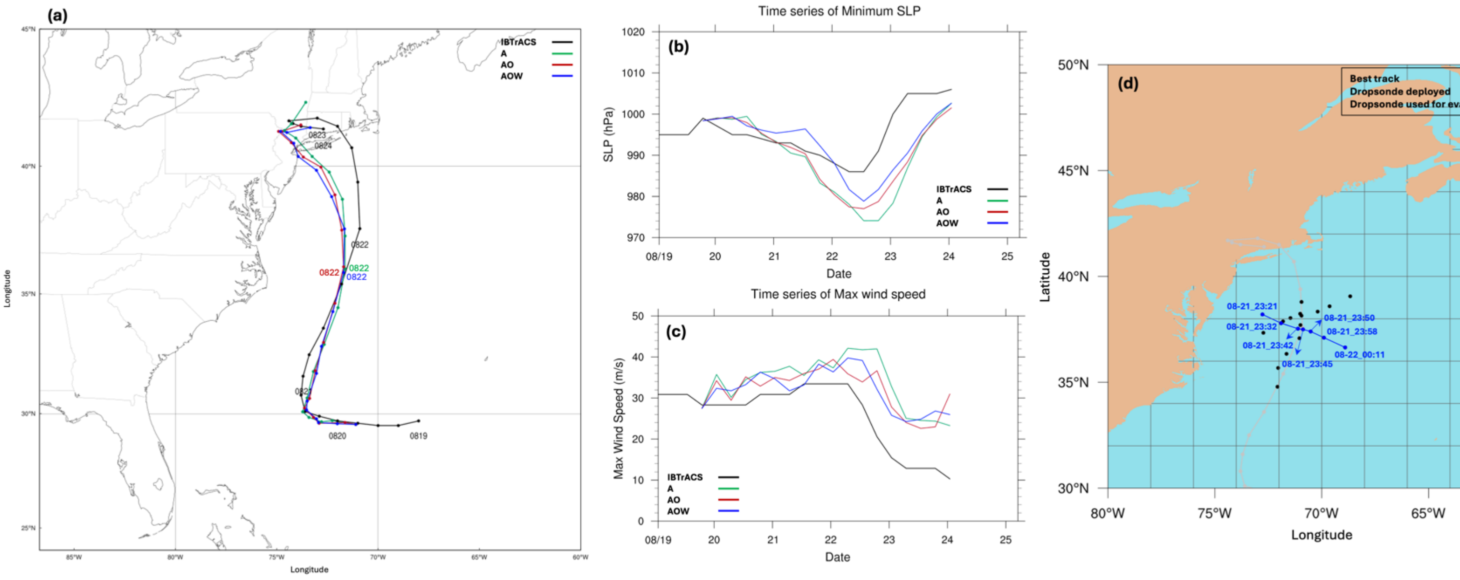

Figure 3. Comparison of simulated (a) track, (b) minimum sea-level pressure (SLP), and (c) maximum 10-m wind speed of Hurricane Henri with IBTrACS Best Track data from 18 UTC 19 to 00 UTC 24 August 2021. Black lines show IBTrACS data; green, red, and blue lines represent experiments 'A,' 'AO,' and 'AOW,' respectively. Panel (d) shows the IBTrACS track (grey) along with dropsonde positions (black and blue dots). The seven dropsondes shown in blue were released during a single NOAA WP-3D flight that traversed the storm center from east to west over approximately 50 minutes, with exact release times indicated in panel (d). These dropsondes were used to evaluate model performance.

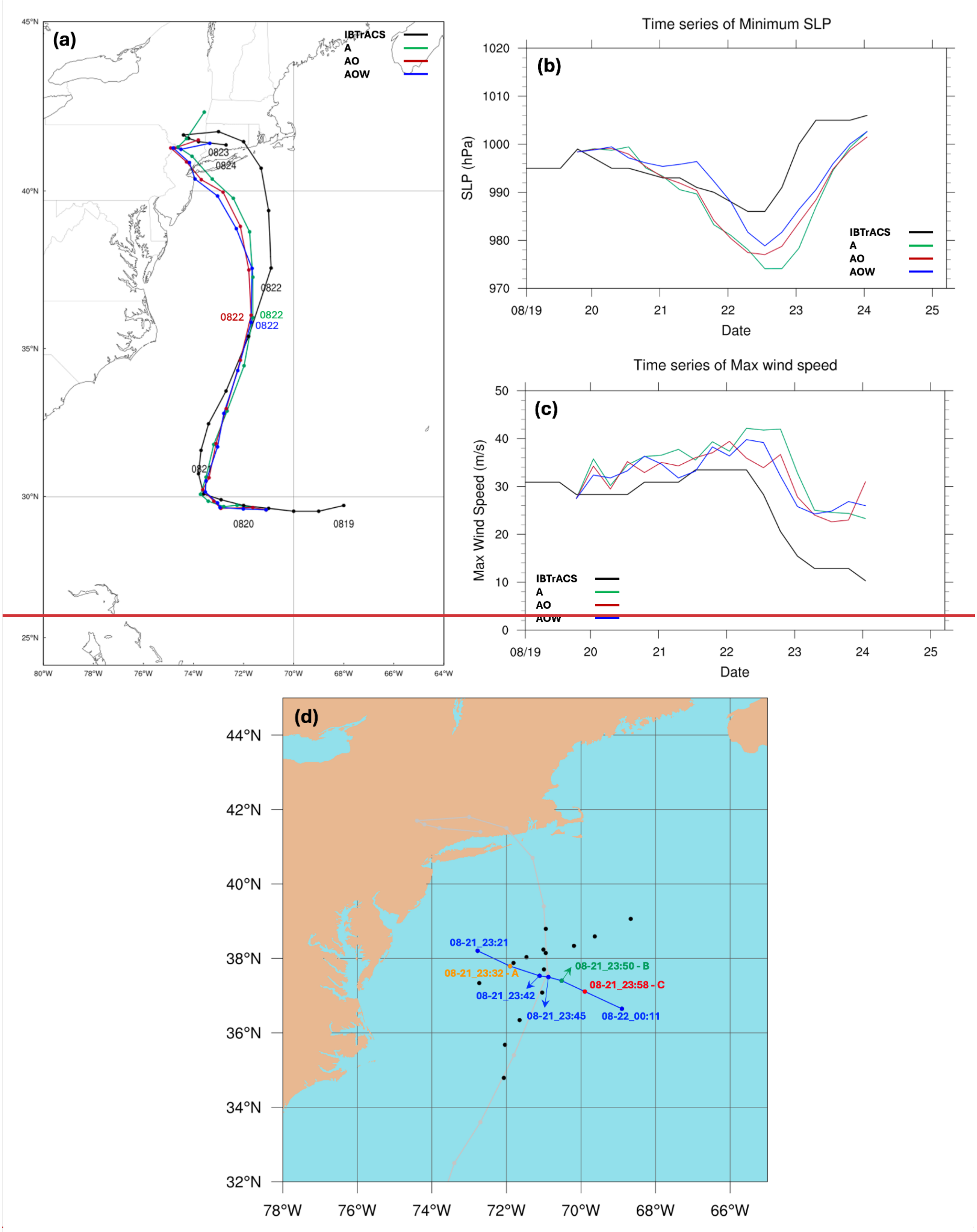
(a)
IBTrACS
A
AO
AOW
0823
0824
0822
0822
0822
0822
0821
0820
0819
45°N
40°N
35°N
30°N
25°N
80°W
78°W
76°W
74°W
72°W
70°W
68°W
66°W
64°W
Time series of Minimum SLP
(b)
SLP (hPa)
1020
1010
1000
990
980
970
08/19
20
21
22
23
24
25
Date
IBTrACS
A
AO
AOW
Time series of Max wind speed
(c)
Max Wind Speed (m/s)
50
40
30
20
10
0
08/19
20
21
22
23
24
25
Date
IBTrACS
A
AO
AOW
(d)
44°N
42°N
40°N
38°N
36°N
34°N
32°N
78°W
76°W
74°W
72°W
70°W
68°W
66°W
08-21_23:21
08-21_23:32 - A
08-21_23:42
08-21_23:45
08-21_23:50 - B
08-21_23:58 - C
08-22_00:11

~~**Figure 3. Comparison of the simulated (a) track, (b) minimum sea-level pressure (SLP), and (c) maximum surface wind speed of Hurricane Henri with the best track during the period from 18 UTC on 19 August to 00 UTC on 24th August 2021. Black lines represent values derived from IBTrACS observations. Green lines indicate the experiment ‘A,’ red lines depict the experiment ‘AO,’ and blue lines show the experiment ‘AOW.’ Figure (d) describes IBTrACS best track (grey line and dots) and dropsonde deployed positions (black and colour dots) during Hurricane Henri. Seven dropsondes (blue and colour dots) along the blue line are selected to assess model performance.**~~

4 Model Validation

4.1 Track and Intensity~~, and Storm Structure~~

~~4.1.1 Track and Intensity~~

Figure 3 presents the tracks, SLP minima, and surface wind speed maxima derived from the three simulations alongside IBTrACS. The results indicate that variations in Henri's tracks across the three experiments are minimal (Fig. 3), consistent with previous findings suggesting that TC tracks are predominantly controlled by large-scale atmospheric circulation processes, rather than by atmosphere-ocean interactions at the temporal and spatial scales resolved in these models (e.g., Zambon et al., 2014). The root-mean square error (RMSE, Table 1) of position indicates all three simulations have similar track errors, with values of 123.7 km for ‘A’, 119.4 km for ‘AO’, and 126.1 km for ‘AOW.’ Higher errors stem mainly from ~~The relatively high error values are mainly due to significant~~ deviations ~~from the observed track~~ after 00 UTC on 22~~nd~~ August, likely due to ~~. These deviations are likely linked to~~ biases in midlatitude upper-level atmospheric wave patterns (e.g., ~~, such as~~ troughs and ridges) affecting the storm ~~, and their interactions with the storm, as the storms are deeply~~ embedded in the baroclinic zone. Preliminary tests show spectral nudging can reduce track errors. ~~that applying zonal and meridional nudging to winds, geopotential heights, and air temperature above the boundary layer can effectively improve track accuracy.~~ However, as the study focuses on ~~previously discussed, the primary objective of this study is to explore~~ atmosphere-ocean-wave interactions in Hurricane Henri’s evolution, all simulations are conducted without nudging, and subsequent analyses reflect those unconstrained results. ~~simulating the evolution and development of Hurricane Henri. Consequently, all results presented in the following sections are derived from simulations conducted without the use of any nudging techniques.~~

~~In terms of m~~Minimum SLP shows ~~for the simulation of Henri’s intensity (Fig. 3b),~~ noticeable differences between the mode~~l~~led storms ~~begin to emerge~~ 12 hours after the simulation starts (Fig. 3b). While all three simulated storms show an overestimation throughout nearly the entire lifecycle of the storm, especially when they reach their peak at 12 UTC on 22~~nd~~ August, the magnitude of this overestimation is reduced in ‘AO’ and ‘AOW’ ~~experiments~~ compared to ‘A.’ In ‘AOW’, the overestimation of minimum SLP is delayed until 00 UTC on 22~~nd~~ August, after which it reaches the ~~. It then reaches the~~ weakest peak minimum SLP among the three. This results in ~~value, resulting in~~ the lowest RMSE in minimum SLP (Table 1). ~~among the three simulations (Table 1).~~ These temporal trends also apply to the maximum surface wind speed (Fig. 3c and Table 1), demonstrating a reduction in overestimation of maximum surface wind speed in both ‘AO’ and ‘AOW’ ~~experiments~~

compared to ‘A.’ Between the experiments ‘AO’ and ‘AOW,’ while ‘AOW’ generally exhibits weaker wind speeds compared to ‘AO,’ it becomes stronger as the storm approaches and reaches its peak intensity, in contrast to the findings for minimum SLP. The potential physical processes underlying this discrepancy are discussed in Section 4.3. ~~It is important to note that the maximum wind speeds recorded in the three simulations represent the peak values at a given time on an hourly basis, which do not fully capture the sustained wind conditions or the broader characteristics of the simulated storms. On the other hand, the observed maximum wind speeds are recorded at a single location and time step, which may not adequately reflect the full extent of potential damage caused by high wind conditions. Therefore, a more thorough evaluation of storm structure, both near the surface and across multiple altitudes, is necessary to provide a more complete assessment of the model's performance.~~

TABLE 1. Root mean square error (RMSE) for each simulation in terms of minimum sea level pressure (hPa), maximum surface wind speed (m s^{-1}), and cyclone track (km).

Experiment	**Minimum sea level pressure (hPa)**	**Maximum surface wind speed (m/s)**	**Cyclone track (km)**
A	**9.4**	**10.2**	**123.7**
AO	**7.9**	**8.7**	**119.4**
AOW	**6.4**	**8.3**	**126.1**

~~TABLE 1. Root mean square error (RMSE) for each simulation in terms of minimum sea level pressure (hPa), maximum surface wind speed (m s^{-1}), and cyclone track (km).~~

~~Experiment~~	~~Minimum sea level pressure (hPa)~~	~~Maximum surface wind speed (m/s)~~	~~Cyclone track (km)~~
~~A~~	~~9.4~~	~~10.2~~	~~123.7~~
~~AO~~	~~7.9~~	~~8.7~~	~~119.4~~
~~AOW~~	~~6.4~~	~~8.3~~	~~126.1~~

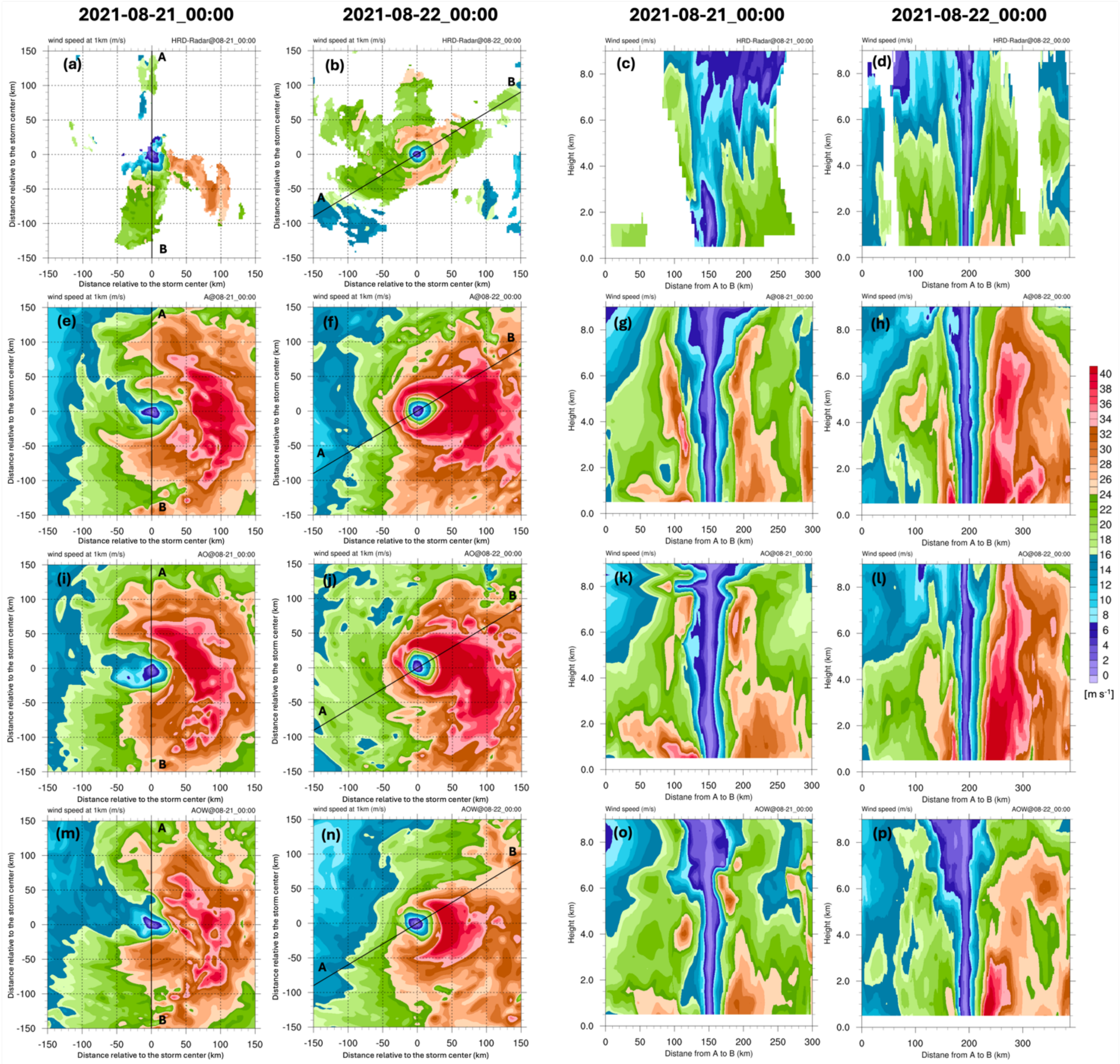

Figure 4. NOAA WP-3D airborne Doppler radar (TC-RADAR) wind speeds at the 1-km level are shown in the top row, with model-simulated wind speeds from the 'A' (second row), 'AO' (third row), and 'AOW' (fourth row) simulations of Hurricane Henri (2021) at 00 UTC on 21 (first and third columns) and 22 August (second and fourth columns). Vertical cross-sections along the A–B line (marked in the left two panels) are shown in the right two columns. All horizontal fields are plotted in a 300 × 300 km storm-centered domain.

4.~~1.~~2 Storm Wind Structure

Figures 4a–d show 1-km level wind speeds and vertical profiles from ~~Here we examine the model's performance in simulating the three-dimensional storm structure of Henri. Figures 4a-d show the airborne Doppler radar-observed (~~TC-RADAR~~)~~ at ~~wind speeds at 1-km level and vertical profiles in Henri at~~ 00 UTC on 21st and 22nd August 2021, along the black lines shown in Figs. 4a-b. On 21 August, observations reveal a strongly asymmetric wind field, with the highest winds concentrated on the storm's right side. This asymmetry results from the combination of Henri's cyclonic circulation and its poleward motion, which enhances wind speeds on the right through additive forward momentum. The vertical cross-section (Fig. 4c) along the line A–B shows wind speeds >20 m s^{-1} largely confined below 4 km on the southern side but extending to 8 km on the northern side. By 00 UTC on 22 August, 12 hours before its minimum central pressure, Henri's wind field becomes more symmetric and compact, with a closed eyewall and winds exceeding 24 m s^{-1} (Figs. 4b,d). A clear calm zone is evident within the eyewall, extending up to 9 km. Strong winds are more evenly distributed around the center, but remain strongest on the right. Corresponding model-simulated wind profiles and 1-km level horizontal wind fields at both times are shown in Figs. 4e–p. ~~On 21st August, the storm shows a distinct asymmetric distribution of strong winds, primarily concentrated on the right side—a characteristic of a tropical storm transitioning into a hurricane (Fig. 4a). This asymmetry is largely due to the combination of the storm's poleward movement and its cyclonic circulation. As Henri moves northward during this period, the winds on the right side effectively combine with the storm's forward motion, leading to higher wind speeds. The vertical cross-section of wind speed along the line from A to B, shown in Fig. 4a, offers a different perspective by contrasting the winds between the northern and southern areas. It shows that wind speeds exceeding 20 m s~~$^{-1}$ ~~are mostly concentrated below 4-km level in the southern part, while strong winds extend up to 8-km level in the northern part at this time (Fig. 4c). At 00 UTC on 22nd August—12 hours before reaching peak minimum SLP intensity, Henri exhibited a compact and nearly closed distribution of strong winds exceeding 24 m s~~$^{-1}$ ~~along the eyewall. This demonstrates a more organized, symmetric appearance, while relatively weaker wind zones remain on the left side (Figs. 4b,d). The vertical cross-section clearly illustrates the structural changes that Henri underwent; it reveals a distinct calm wind zone within the eyewall, extending up to 9-km level. Areas of strong wind speeds exceeding 24 m s~~$^{-1}$ ~~are relatively evenly distributed relative to the centre, with the strongest winds located on the right side. The corresponding simulated vertical profiles and horizontal distributions of wind speed at 1-km level at 00 UTC 21st and 22nd August 2021 are shown in Figs. 4e-p.~~

All three simulated storms reasonably capture Henri's ~~the~~ structural evolution—from a broad, asymmetric wind pattern with strong right-side winds at 00 UTC 21 August (as seen in TC-RADAR) to a more compact, symmetric structure by 00 UTC 22

August. ~~changes that Henri underwent, including the transition in wind distribution from a wide, open, asymmetric pattern with strong wind zones on the right side observed at 00 UTC on 21st in TC-RADAR to a more compact, closed, symmetric structure as it intensifies observed at 00 UTC on 22nd August in TC-RADAR.~~ However, the simulations, especially ~~ed storms noticeably overestimate intensity horizontally and vertically, especially the~~ experiments ‘A’ and ‘AO,~~.~~’ overestimate wind intensity both horizontally and vertically. The fully coupled run~~simulation~~ ‘AOW’ reduces this bias, producing more realistic radial wind profiles at 1 km along line A–B and achieving the highest Pearson correlations with TC-RADAR (r = 0.95 for horizontal distribution and 0.72 for vertical cross-section). To To assess wind distribution more comprehensively, we use probability density functions (PDFs) across all available TC-RADAR grid cells (0.5–9 km altitude within a 300 × 300 km domain centered on the storm). All simulations skew toward higher wind intensities, but ‘AOW’ shows improved performance, especially in the upper tail, suggesting reduced wind bias during storm intensification (Fig. 5).

~~notably mitigates the overestimation with better radial wind profiles at the 1-km level along the line from A to B for both times (Fig. A1), and higher Pearson correlation coefficients (r) of 0.95 and 0.72, respectively – the highest correlations among the three simulations at both times. For a more comprehensive examination, we assess the wind distribution using probability density function (PDF) considering all available observation grid cells horizontally and vertically within the 300 km x 300 km domain relative to the storm centre, from 0.5 km to 9 km above the ground provided by TC-RADAR (Fig. 5). The PDF distribution clearly shows that all three simulated wind distributions skew toward higher intensities compared to the observed data at both times. However, it is evident that ‘AOW’ reduces the overestimation, particularly in the upper tail, indicating that ‘AOW’ improves the wind bias during the storm’s development.~~

While ~~the~~ TC-RADAR provides rich ~~comprehensive observations in both~~ horizontal and vertical coverage, ~~dimensions,~~it only samples above 0.5-km, limiting surface-level validation. Dropsonde data help ~~the lowest level of TC-RADAR for this storm is 0.5-km above the ground. This height limits us to validate modelled winds at heights that hurricanes pose actual risks to offshore infrastructure and human activities. Dropsonde observations from aircraft can~~ bridge this gap. Figure S2 ~~6~~ shows ~~the~~ vertical cross-sections up to an altitude of 3.2 km along the blue line in Fig. 3d: consistent with TC-RADAR, strongest winds appear 10–30 km east of the center, while much weaker winds dominate the western side. These asymmetries are captured in all simulations, though generally overestimated.

A~~ of observed and simulated wind speed along the blue line shown in Fig. 3d. Consistent with TC-RADAR observations at higher altitudes, the dropsonde observation also shows that the strongest winds are on the eastern side, approximately 10 to 30 km from the storm centre, with intensity gradually decreasing toward the edge. On the other hand, much weaker speeds are observed on the western side, ranging from -10 to -200 km (Fig. 6a). The observed patterns are reasonably captured in all three simulations, though they are generally overestimated. The a~~zimuthally averaged vertical profiles (Fig. 6) ~~of simulated wind speeds~~ in the inner-eyewall (~~defined as region within~~ $0.2 \leq r/RMW \leq 1$) and ~~the~~ outer-eyewall ($2 \leq r/RMW \leq 2.5$) regions at the dropsonde locations further confirm that all simulations overestimate low-level winds (below 2 km). ~~are also evaluated (Fig 7). In both the inner- and outer-eyewall regions, it is evident that all three simulations overestimate wind speeds in the low troposphere (below 2 km).~~ However, ‘AOW’ aligns more closely with observations, particularly in the outer-eyewall. This

This improvement is critical for offshore wind energy, where accurate wind profiles near hub height are essential for turbine design, placement, and risk mitigation in storm-prone regions.

~~compared to the other two simulations in both the inner- and outer-eyewall regions. Notably, in the outer-eyewall region, 'AOW' is much closer to the observed values. These insights are particularly relevant for offshore wind resources, as accurate wind profiles at hub heights and below are crucial for optimizing turbine placement and enhancing energy generation efficiency in storm prone areas. A better representation of wind profiles, especially in the low troposphere and near the surface, not only helps in predicting potential impacts on the turbines but also informs better design and operational strategies.~~

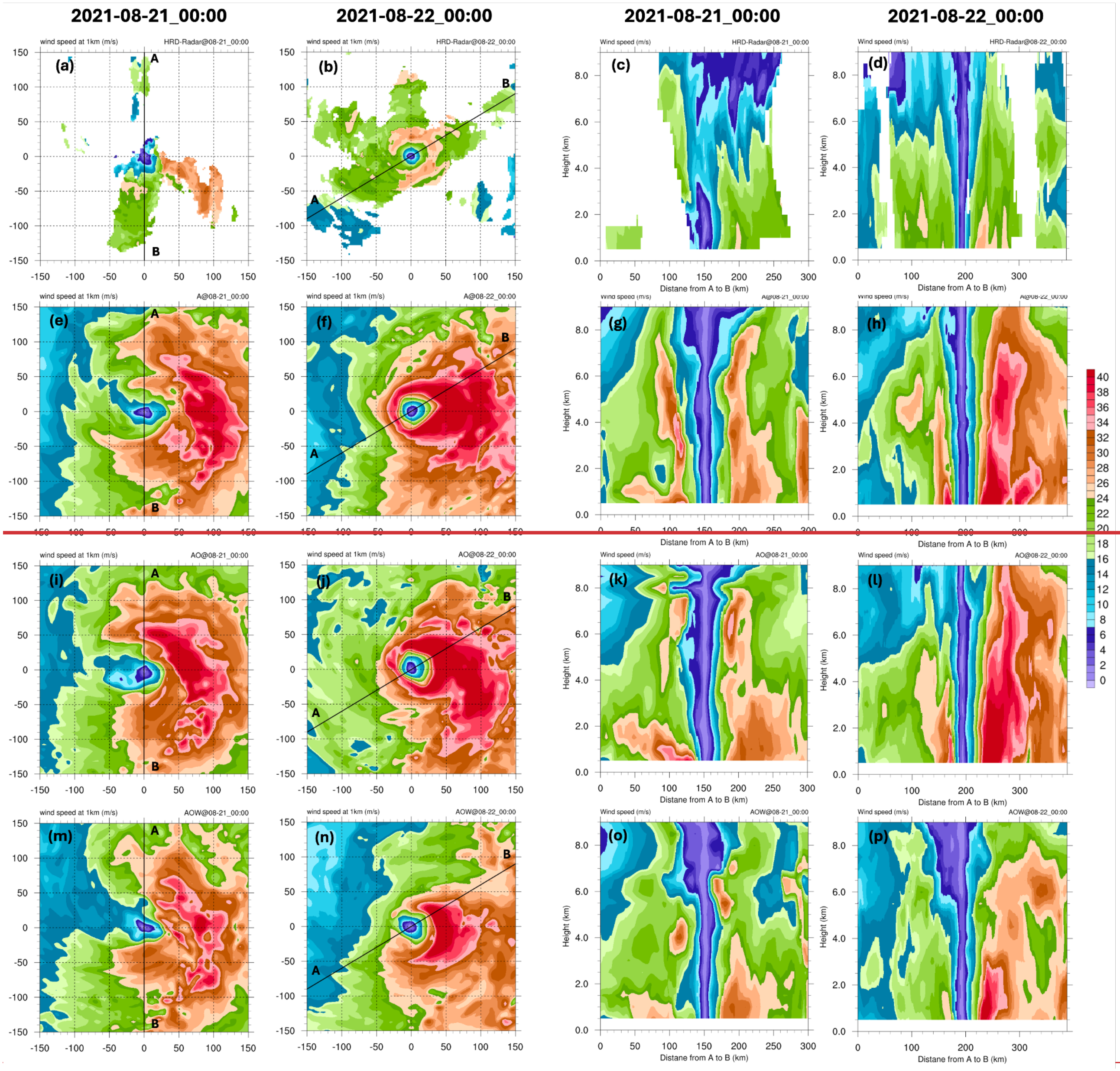

~~Figure 4. NOAA WP-3D airborne Doppler radar-observed (TC-RADAR) wind speeds at the 1-km level are shown in the first row, along with the corresponding model-simulated wind speeds for Hurricane Henri (2021) from the 'A' simulation (second row), 'AO' simulation (third row), and 'AOW' simulation (fourth row) at 00 UTC on August 21 (first and third columns) and 00 UTC on August 22 (second and fourth columns). The vertical cross-sections of wind speeds along the line from point A to B, indicated in the leftmost two columns, are presented in the rightmost two columns. All horizontal distributions are displayed in a 300 km × 300 km storm-centred coordinate.~~

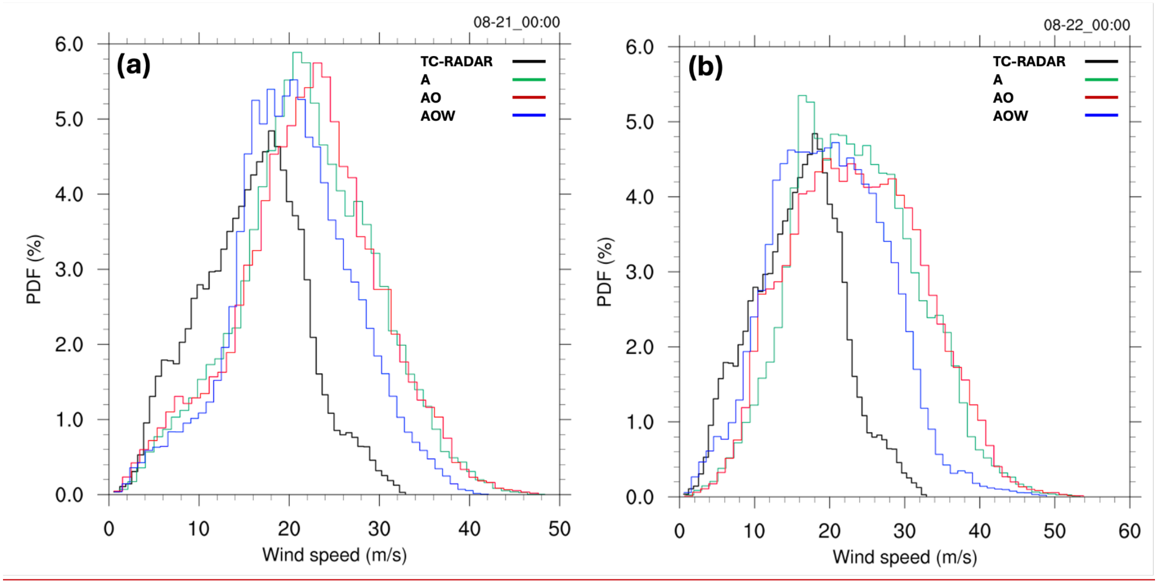

Figure 5: Probability density function of wind speed in a 300 km x 300 km storm-centered coordinate, considering vertical levels from 0.5 km to 9 km above the ground, for 00 UTC on 21 (a) and 22 August (b) 2021. The data are derived from TC-RADAR (black lines), experiment 'A' (green lines), experiment 'AO' (red lines), and experiment 'AOW' (blue lines).

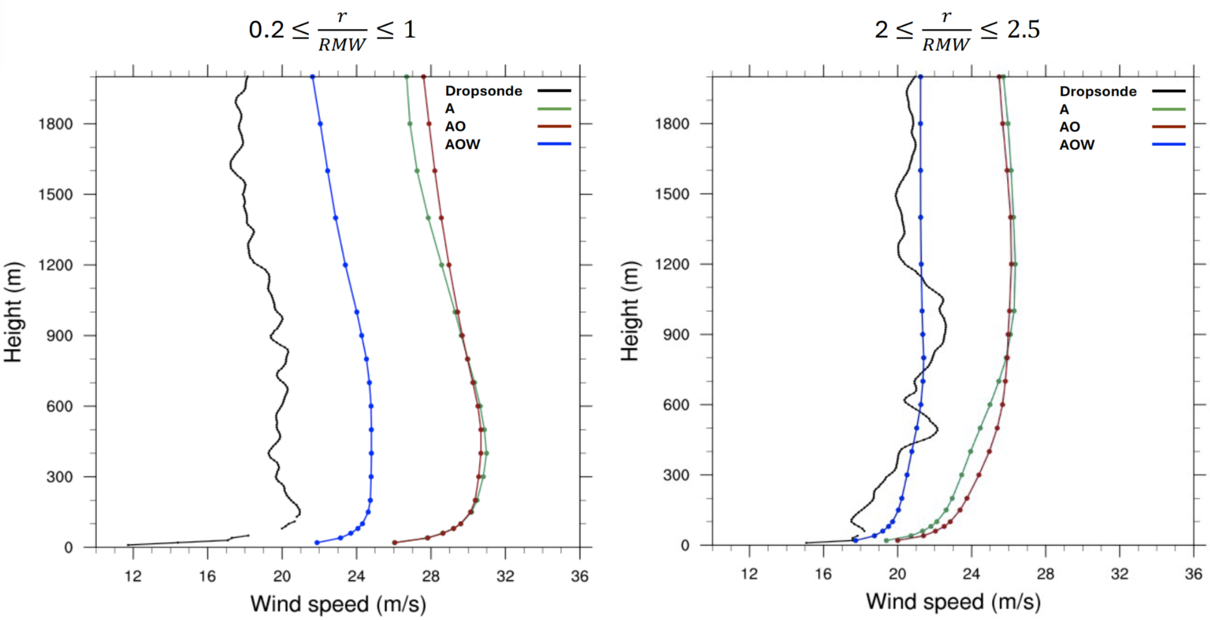

Figure 6. Vertical profiles of azimuthally averaged wind speed for dropsondes (black lines), experiment 'A' (green lines), experiment 'AO' (red lines), and experiment 'AOW' (blue lines). The vertical profiles are azimuthally averaged in the inner-eyewall region (left; 0.2≤r/RMW≤1) and the outer-eyewall regions (right; 2≤r/RMW≤2.5), based on the locations of the seven dropsondes highlighted in blue dots in Fig. 3d at 00 UTC on 22 August 2021. RMW indicates radius of maximum wind, and r shows radius relative to the storm center.

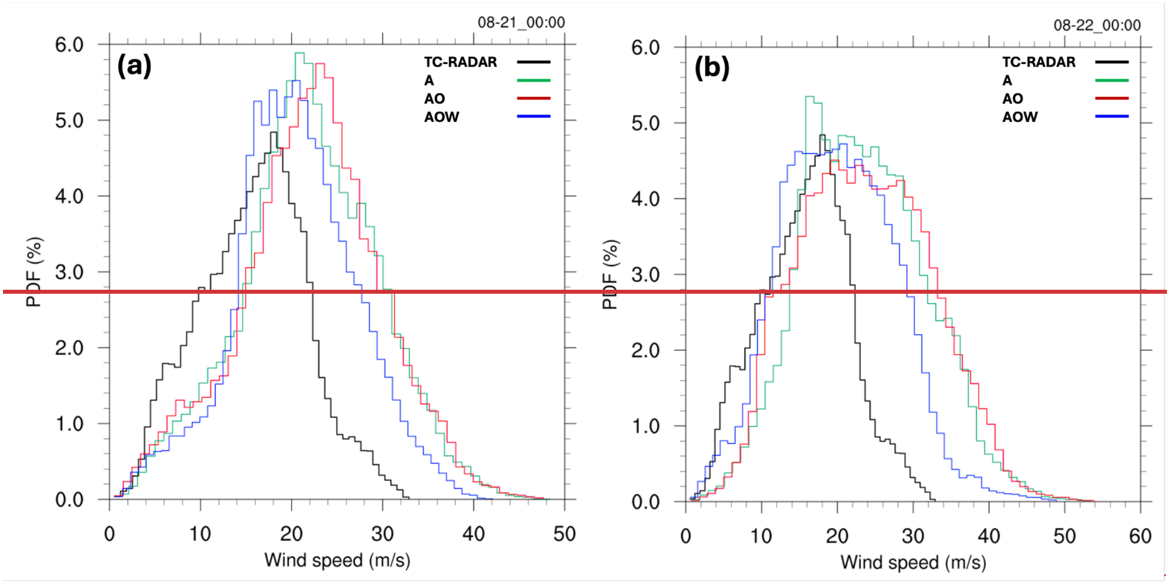

~~**Figure 5. Probability density function of wind speed in a 300 km x 300 km storm-centered coordinate, considering vertical levels from 0.5 km to 9 km above the ground, for 00 UTC on 21 August (a) and 22 August (b) 2021. The data are derived from TC-RADAR (black lines), experiment 'A' (green lines), experiment 'AO' (red lines), and experiment 'AOW' (blue lines).**~~

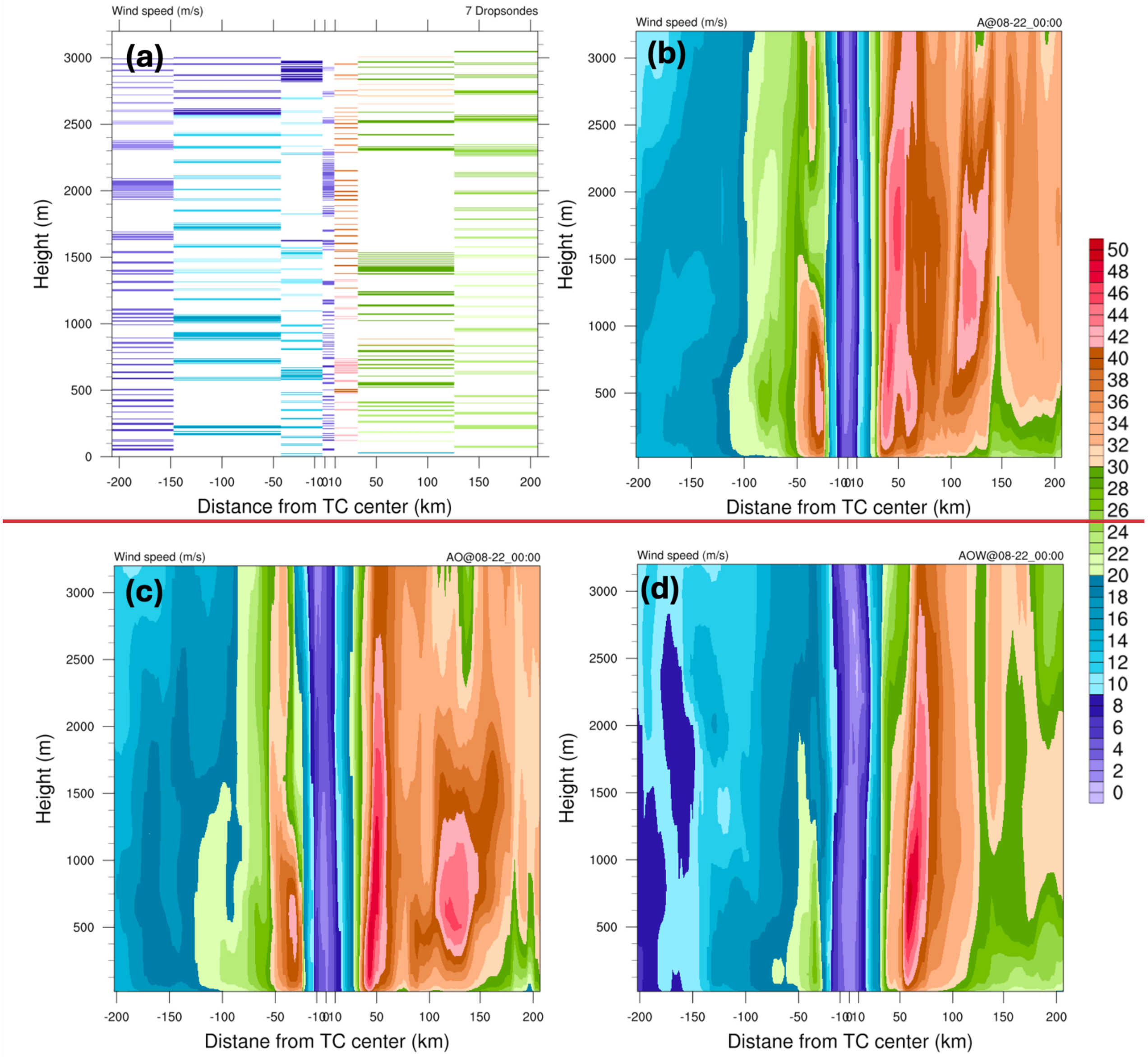

~~Figure 6. Vertical cross-sections of (a) observed wind speed along the locations of the seven dropsondes, shown as colored dots in Fig. 3(d). The times of the first and last dropsondes are 23:23 UTC on 21 August and 00:11 UTC on 22 August, respectively. Corresponding cross-sections from (b) experiment 'A', (c) experiment 'AO', and (d) experiment 'AOW' are shown.~~

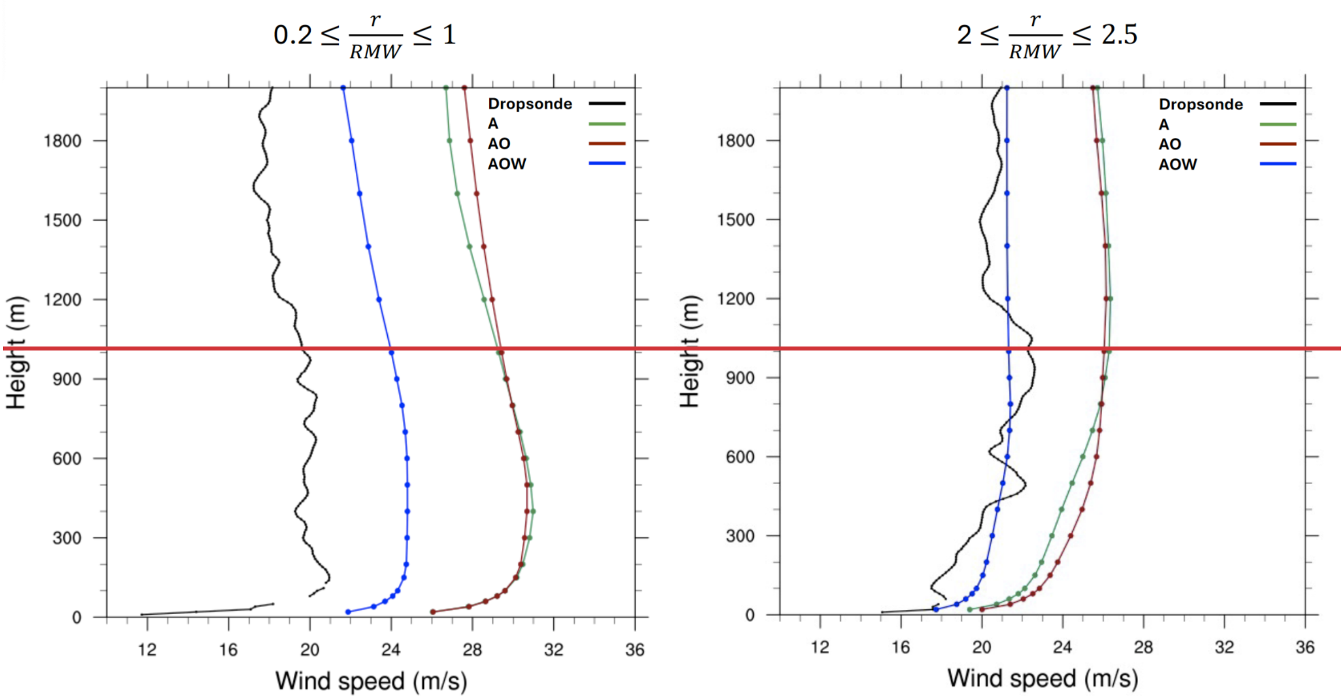

~~**Figure 7. Vertical profiles of azimuthally averaged wind speed for dropsondes (black lines), experiment 'A' (green lines), experiment 'AO' (red lines), and experiment 'AOW' (blue lines). The vertical profiles are azimuthally averaged in the inner-eyewall region (left; 0.2≤r/RMW≤1) and the outer-eyewall regions (right; 2≤r/RMW≤2.5) on 22nd August 2021.**~~

4.3~~2~~ Sea Surface Temperature~~ and Waves~~

~~4.2.1 Sea Surface Temperature~~

From the ocean's perspective, SST and surface roughness are key factors influencing TC intensity, as they directly affect the exchange of heat, moisture, and momentum between the ocean and the storm ~~Several factors influence TC intensity, with SST and ocean surface roughness being among the most important, as they directly affect the heat and moisture available to fuel the storm~~ (Zambon et al., 2014, 2021; Zhao et al., 2022). The main distinction among the three simulations lies in how SST and ocean surface roughness are represented, influencing surface enthalpy and momentum fluxes through air-sea interactions. Accordingly, SST is used both as an indicator of storm evolution and as a dynamic driver of intensity across the three simulations. Therefore, evaluating how well the coupled model reproduces observed SST is critical for assessing its ability to realistically capture ocean dynamics and storm–ocean interactions.~~In our model configurations, the primary difference between the simulations lies in the treatment of SST and sea surface roughness, which ultimately impacts surface enthalpy and momentum fluxes through atmosphere-ocean interaction feedback. Therefore, we use SST as both a primary indicator and a driving mechanism of storm intensity to analyse the differences in Henri's intensity modelled by the three experiments.~~

Figure ~~8~~7 shows the SST distribution across the simulation domain for all three experiments, along with OSTIA observations from 12 UTC on 20 to 12 UTC on 23 August 2020. Since OSTIA provides daily SST data, the statistics in Table 2 represents an average over these four days. In experiment ‘A’, the SST is derived from GFS, and is technically driven by observed SST data. Therefore, it captures key large-scale features well, such as the Gulf Stream and warm waters along the Gulf Coast. However, it consistently underestimates SST across the domain during this period. In addition, its relatively low resolution (0.25°) limits its ability to capture small-scale SST patterns, contributing to the higher RMSE values shown in Table 2.

The ocean-coupled simulations ('AO' and 'AOW'), which are driven by oceanic initial and boundary conditions from the HYCOM analysis, successfully capture major SST features such as the Gulf Stream and Gulf Coast, with enhanced spatial detail. This improved representation contributes to lower RMSE values compared to the atmosphere-only simulation ('A') (Table 2). However, both 'AO' and 'AOW' tend to overestimate SSTs in the open North Atlantic and underestimate them near the northeastern U.S. coast (Figs. 7d, l, p), likely due to cold wakes generated by the simulated storms and deviations in their tracks from observations. Nevertheless, the ocean-coupled simulations reasonably reproduce the observed SST, with RMSE values of 0.564 and 0.577 for ‘AO’ and ‘AOW’, respectively—lower than that of 'A'—while maintaining comparable pattern correlation overall (Table 2).

To assess the potential influence of track biases on SST and MSLP, we first examined 'A' simulation. It exhibits overintensification of MSLP, a consequence of its simulated track failing to coincide with the observed cold wakes in the GFS data. This misalignment prevents the realistic capture of crucial atmosphere-ocean heat and moisture exchanges. Conversely, ocean-coupled simulations ('AO' and 'AOW') more accurately represent storm-induced modifications to surface energy and momentum fluxes. By explicitly modeling SST cooling along their simulated storm paths, these coupled runs achieve a more realistic depiction of storm intensity. In particular, 'AOW' simulation shows enhanced SST cooling around the time of peak intensity and thereafter, further contributing to a reduction in MSLP. Spatial and temporal averaging of SST within a 300 km × 300 km storm-centered domain from 12 UTC on 21 August to 12 UTC on 22 August indicates an SST of 299.7 K for ‘AOW’, compared to 300.2 K previously—representing a 0.5 K reduction and bringing it closer to the OSTIA value of 299.1 K (Table 3). Details of the storm-centered SST distributions are provided in the Supplementary Information. This improved performance in 'AOW' can be attributed to the effect of wave-induced vertical mixing, which effectively brings cooler subsurface water to the surface, aligning with our previous discussion and prior research (e.g., Wada et al., 2010; Zambon et al., 2014)

Table 2. Temporally averaged root mean square error (RMSE) and Pearson product- moment coefficient of linear correlation (r) for SST in each simulation compared to OSTIA SST observations from 12 UTC on 20 to 12 UTC 23 August, 2021.

Experiment	RMSE	Pattern Correlation
A	0.631	0.992
AO	0.564	0.991
AOW	0.577	0.990

Table 3. Spatially averaged SST (K) derived from A, AO, AOW, and OSTIA observation in a 300 km x 300 km storm-centered coordinate at 12 UTC 20, 12 UTC 21, and 12 UTC 22 August.

Experiment	12 UTC 20 August	12 UTC 21 August	12 UTC 22 August
A	302.01	301.81	299.37
AO	301.79	301.83	298.47
AOW	301.76	301.70	297.70
OSTIA	302.15	301.43	296.76

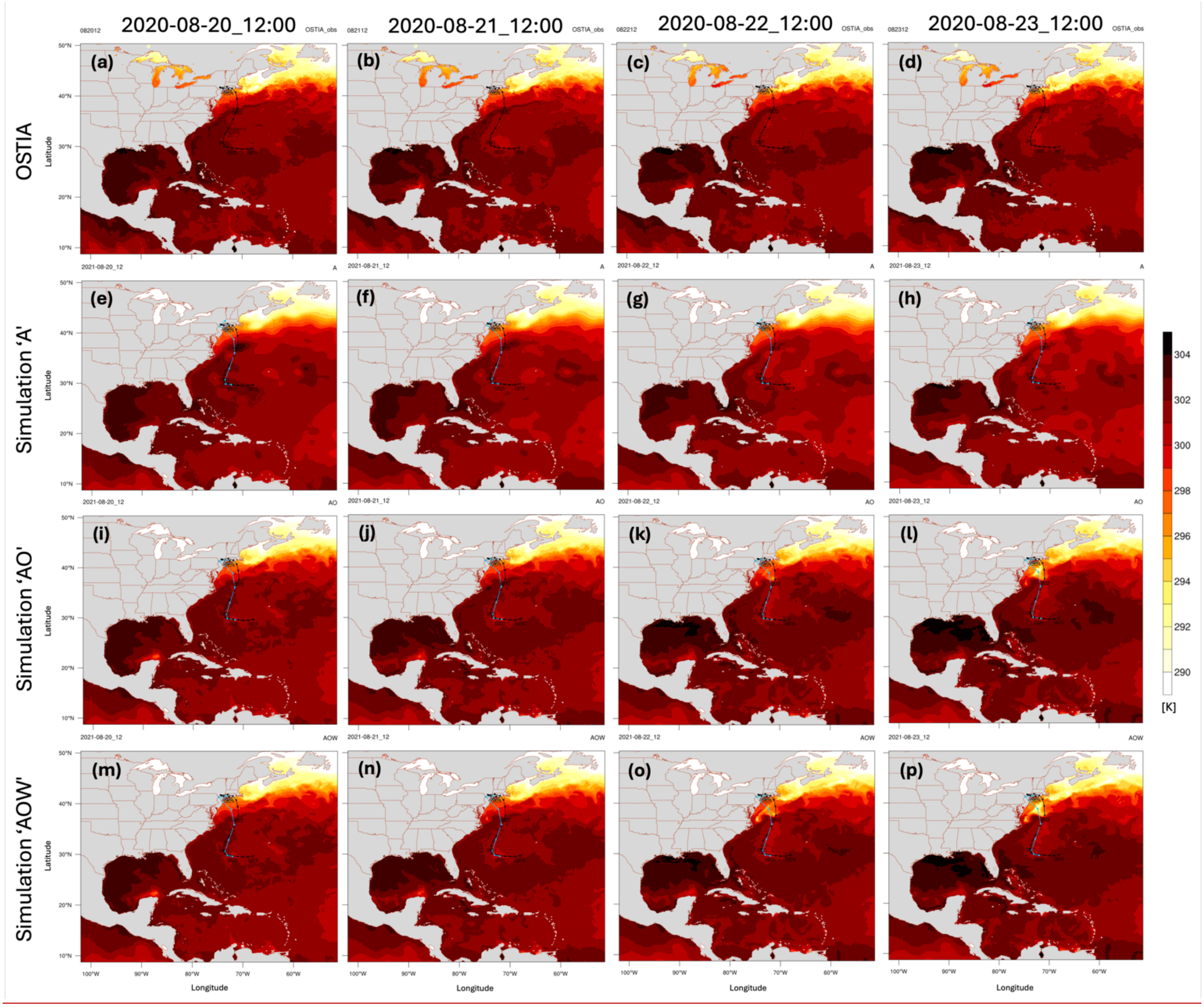

Figure 7. Vertical SST distribution (K) for OSTIA (top panel), 'A' (second panel), 'AO' (third panel) and 'AOW' (bottom panel) at 12 UTC on 20 (first column), 21 (second column), 22 (third column), and 24 August 2020 (fourth column). The black dots and lines indicate the best track derived from IBTrACS. The light blue dots and lines depict simulated storm locations and tracks.

~~illustrates the distribution of SST over the entire simulation domain for all three simulations, along with OSTIA observation at 12 UTC on 20th August (pre-storm) and 12 UTC on 23rd August (post-storm). The figure also shows the differences of SST between post- and pre-storm periods. Overall, all three simulations reasonably represent the SST distribution in both pre- and post-storm periods, effectively capturing the intensity and spatial extent of the Gulf Stream and surrounding warm SST zones (Fig. 8). Notably, both 'AO' and 'AOW' simulations adequately resolve cooler SSTs along the storm tracks, with comparable RMSEs and pattern correlations in comparison with SST in 'A' (Table 2). However, the two coupled simulations tend to overestimate cooling as the storms approach the U.S. Northeast Coast (Fig. 8f,i,l).~~

~~Figure 9 displays the distribution of SST for the four datasets in a 300 km x 300 km storm-centred at 24-hour intervals from 12 UTC on 20th August to 12 UTC on 22nd August. The area-averaged SST in the storm-centred coordinate is calculated and OSTIA and listed in Table 3. At 12 UTC on 20th August, Henri turned northward and continued to strengthen with the aid of relaxed wind shear and high SST associated with the Gulf Stream (Pasch, 2022; Fig. 9a). OSTIA well illustrates the warm SST, with values exceeding 302.2 K (29.05 °C) on the southern side of the storm (Fig. 10i). However, none of the three simulations accurately capture the southern warm SST distribution due to differences in their translation speeds and corresponding locations, as well as biases in SST (Fig. 3a and 8-9). In addition, the two coupled simulations overpredict the cold wakes on both southern and eastern sides of the storm (Figs. 9c-d), resulting in weaker minimum SLP compared to the observation at this time (Fig. 3b). As the storm moved north-northeastward, the Gulf Stream and the surrounding warm waters allowed it to deepen gradually, reaching its peak minimum SLP around 12 UTC 22nd August. It then weakened rapidly as it interacted with land masses, making landfall in Rhode Island (Figs. 3 and 8). While the warm waters and cold wakes associated with the storm are generally captured in all three simulations, the magnitude and spatial extent of the storm produced cold wakes are mostly weaker, leading to an over-intensification of all simulated storms compared to the observation until they make landfall (Figs. 9e-l). The overestimations are also partly due to the biases in track, making the simulated storms approach the coast along different paths, which affect their intensity and interaction with the surrounding environment. Note that SST in 'A' is updated by GFS reanalysis data at 6-hour intervals. Although the SST in GFS is derived from observation-based reanalysis data, its distribution and magnitude differ from those of OSTIA (Fig. 8). This discrepancy likely arises from variations in observational data sources and spatial resolution. OSTIA SST is generated using a combination of satellite observations and in situ measurements (e.g., buoys, ships), offering high-resolution analysis at a 1/20° grid. In contrast, GFS SST features a coarser resolution of 0.25° and predominantly relies on global ocean models and reanalysis datasets, which may not incorporate the same observational data sources as OSTIA. Although all three simulations overestimate the intensity of Henri, the experiment 'AOW' noticeably reduces the overestimation during the development as well as weakening stages, as previously discussed. This might be due to the greater cooling of SST associated with wave-induced vertical mixing, bringing cold water up to the surface consistent with prior studies (e.g., Wada et al., 2010; Zambon et al., 2014; Figs. 10d and h).~~

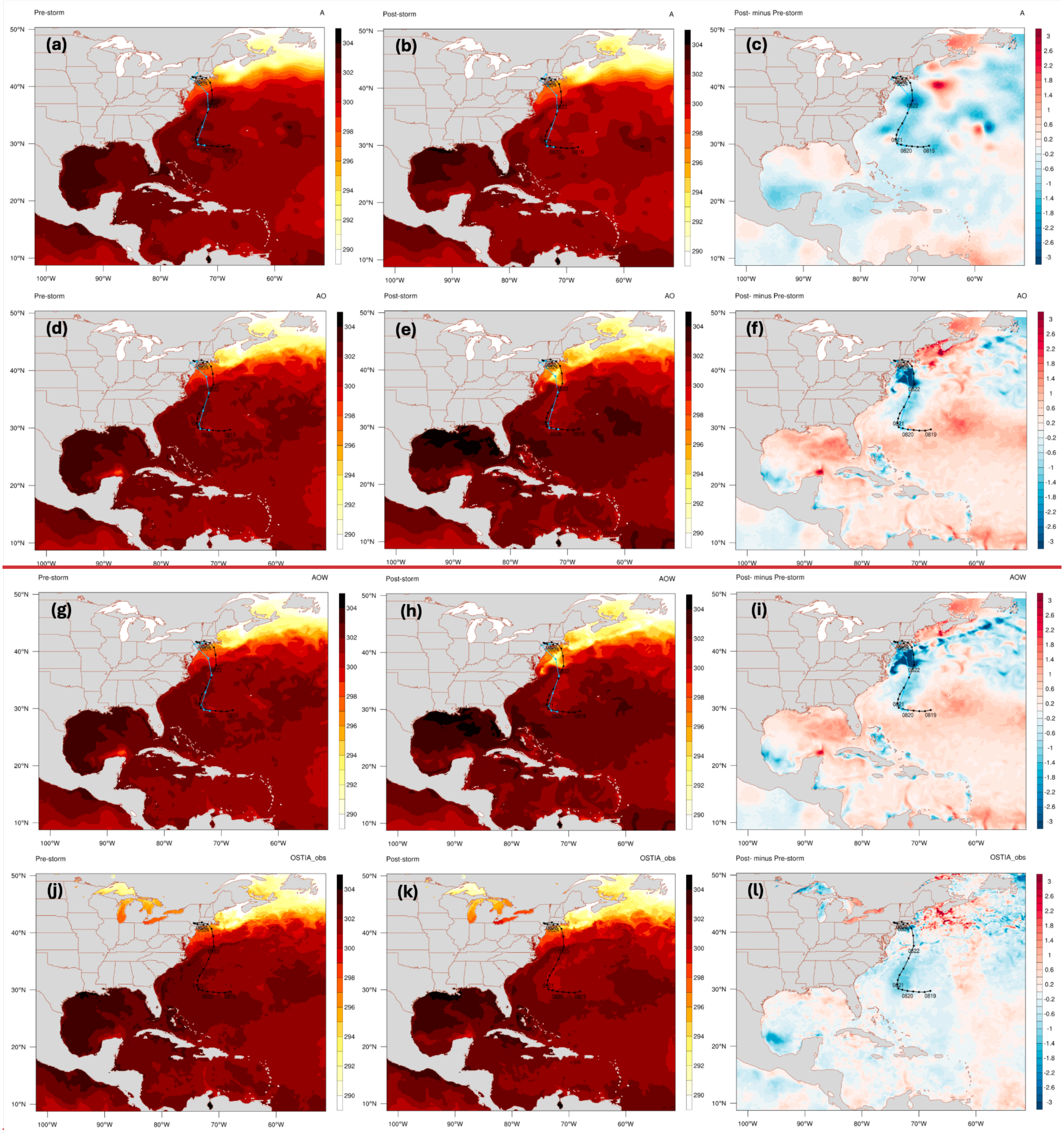

~~Figure 8. SST comparisons for various experiments: 'A' (SST updated by GFS at 6-hour intervals, first row), 'AO' (atmosphere-ocean model coupling, second row), 'AOW' (atmosphere-ocean-wave model coupling, third row), and OSTIA SST observation (fourth row). The first column shows SST at 12 UTC on 20th August (pre-storm), the second column displays SST at 12 UTC 23rd August (post-storm), the third column presents change in SST between pre-storm and post-storm. The black dots and lines indicate the best track derived from IBTrACS. The light blue dots and lines depict simulated storm locations and tracks.~~

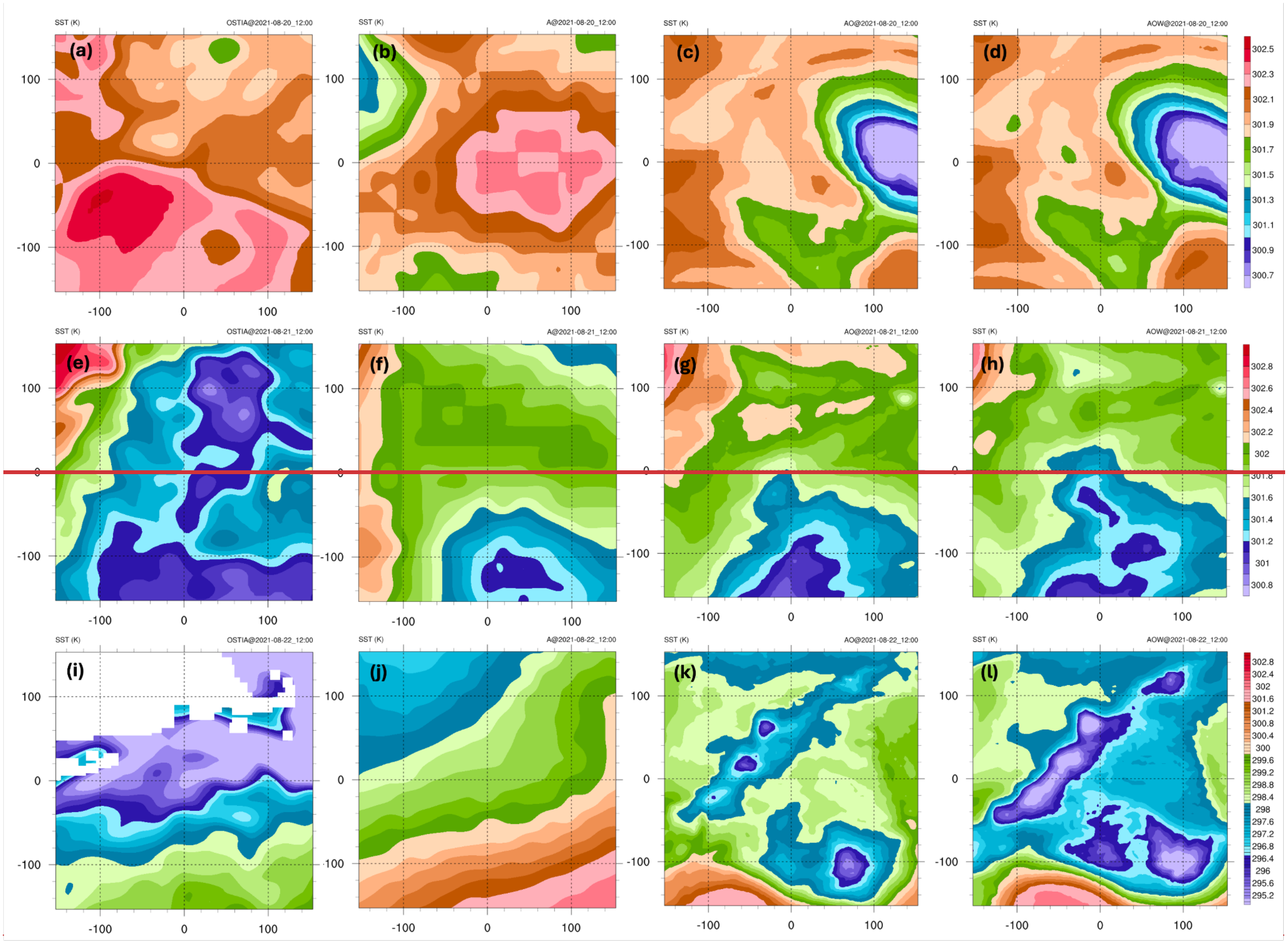

~~**Figure 9. Distribution of SST in a 300 km × 300 km storm-centered coordinate at 12 UTC on August 20th (top row), 12 UTC on August 21st (middle row), and 12 UTC on August 22nd (bottom row). The first column shows SST derived from OSTIA, the second column presents SST values from 'A', the third column displays SST from 'AO', and the fourth column shows SST from 'AOW' simulation.**~~

~~**TABLE 2. Temporally averaged root mean square error (RMSE) and Pearson product–moment coefficient of linear correlation (r) for SST in each simulation compared to OSTIA SST observations from 12 UTC on 20th August to 12 UTC 23rd August, 2021.**~~

~~Experiment~~	~~RMSE~~	~~Pattern Correlation~~
~~A~~	~~0.631~~	~~0.992~~
~~AO~~	~~0.564~~	~~0.991~~
~~AOW~~	~~0.577~~	~~0.990~~

~~TABLE 3. Spatially averaged SST (K) derived from A, AO, AOW, and OSTIA observation in a 300 km x 300 km storm-centered coordinate at 12 UTC 20 August, 12 UTC 21 August, and 12 UTC 22 August.~~

~~Experiment~~	~~08-20_12:00~~	~~08-21_12:00~~	~~08-22_12:00~~
~~A~~	~~302.01~~	~~301.81~~	~~299.37~~
~~AO~~	~~301.79~~	~~301.83~~	~~298.47~~
~~AOW~~	~~301.76~~	~~301.70~~	~~297.70~~
~~OSTIA~~	~~302.15~~	~~301.43~~	~~296.76~~

4.~~2.2~~4 Ocean Surface Waves

This section assesses how accurately our model simulates ocean surface waves ~~In this section, we examine the accuracy of modelled ocean surface waves throughout the evolution of~~during Hurricane Henri at ~~the~~ two NDBC buoy~~s.~~ locations. During Henri's primary development, ~~the storm's main development stage, station~~buoy 41001 was directly in the paths of the eyewall, while ~~experienced the passage of the eye and the high winds and waves associated with the eyewall. Meanwhile, station~~ 41002 was positioned approximately ~~was positioned about~~ 120 km to the left of the storm's cent~~re~~er during its earlier stages (Fig. 8a). ~~closest approach in the early development stage.~~ The fully coupled experiment ~~reasonably~~ successfully captures the general temporal trends of wind speed at both sites~~locations~~ (Figs. ~~10~~8b-c). However, a slower simulated storm translation speed, particularly between 06:00 and 12:00 UTC on 21 August, led to a delay of roughly 12 hours in both wind speed and wave height peaks. Furthermore, the model overestimates significant wave height by about 1–2.5 m at both locations during peak conditions (Figs. 8d–e).~~due to the slower translation speed of the modelled storm, particularly from 06 UTC to 12 UTC on 21st August, the wind speed peaks are approximately 12 hours later than observed at the two locations. Consequently, the wave peak times at both locations are similarly delayed. The modelled magnitude of significant wave height is about 1-2.5 m higher than observed during peak times (Figs. 10d-e).~~ At station 41001, this overestimation is primarily attributable to discrepancies in wind speed. For station 41002, an ~~e difference in wind speed between observed and modelled ones generally accounts for the difference in significant wave height. On the other hand, at station 41002, an~~ additional contributing factor is the model's faster simulated translation speed— ~~that may contribute to the difference between observed and modelled significant wave height is the faster translation speed following the storm's slow movement from 06 UTC on 20th to 00 UTC on 21st August. Specifically, the translation speed of modelled storm is approximately~~ 6.3 m s^{-1} compared to the observed ~~, whereas the observed speed is approximately~~ 4.8 m s^{-1} between ~~during the period from~~ 00:00 ~~UTC~~ and ~~to~~ 06:00 UTC on 21st August. It is well-established that increased forward motion enhances wind speed and wave growth on a storm's right side, leading to higher waves (Chen et al., 2013). While the model accurately reproduces wave direction at station 41001, it fails to capture the sharp directional shift observed at station 41002 between 06:00 and 09:00 UTC on 21 August (Figs. 8f-g). This discrepancy may stem from the model's increased wave height and wavelength, which can suppress rapid directional changes. Despite these biases in wave height magnitude and timing, the model generally provides a reasonable representation of wave behavior at both locations and successfully captures key trends in storm-induced wave dynamics during Hurricane Henri.

Understanding the accuracy of modeled ocean surface waves, particularly their directional characteristics, is crucial because previous investigations into TC wind impacts on offshore wind turbines (e.g., Sanchez Gomez et al., 2023; Wei et al., 2017; Itiki et al., 2023) have often overlooked the complexities of wind–ocean–wave interactions. This oversight, common in atmosphere-only or empirical models, significantly limits accurate risk prediction for offshore infrastructure by failing to capture both direct and indirect impacts. For instance, Ma and Sun (2023) demonstrated that under extreme wind-wave conditions, such as those in hurricanes, coupling between wind and wave dynamics significantly increases the aerodynamic loads on offshore wind turbines. This coupling markedly amplifies the variability of those loads, suggesting that traditional decoupled models may underestimate the structural demands during such severe events.

Figure 9 shows that wind and wave alignment varies considerably over time, with periods of near co-alignment interspersed with misalignments. The directional divergence is site-specific, highlighting the influence of localized impact depending on locations relative to the storm center. ‘AOW’ captures key characteristics of directional interactions, reproducing the timing and magnitude of misalignment trends reasonably well (Figs. 9 bottom panel). Notably, the simulations reflect the directional sensitivity at both sites, suggesting fidelity in representing storm-induced wave generation and propagation, implying that the fully coupled modeling system provides a more realistic representation of the complex environmental loads on offshore wind turbines, particularly under extreme conditions like TCs.

Figure 10 illustrates simulated ocean surface wave conditions and 10-m wind vectors from 'AOW' experiment at 12:00 UTC on 22 August. Consistent with prior studies (e.g., Chen et al., 2013; Wright et al., 2001), TC-induced wave fields typically exhibit asymmetry, with the highest significant wave heights occurring in the front-right quadrant. This pattern is clearly evident in our simulation, as Henri moves northwest, producing the largest waves in its right and front-right quadrants (Fig. 10a). The storm's motion further enhances wave growth on the right side due to a longer fetch (Figs. 10a-b). Significantly, directional misalignment between wind and waves is apparent across most storm quadrants, except on the right side where both wind and waves are aligned, also consistent with previous findings (Fig. 10d). This widespread misalignment as well as aligned directions highlight the complex atmosphere-wave interactions that necessitate careful consideration in offshore wind load assessments.

~~On the right side of the storm’s path, the wind speed is amplified because the storm’s forward motion adds to the wind speed. In this context, a faster moving storm can lead to stronger wind forcing, which increases wave energy and promotes greater wave growth, resulting in higher waves (Chen et al., 2013). While the fully coupled experiment effectively captures the wave direction at station 41001, it does not resolve the sharp directional change observed at station 41002 between 06 UTC and 09 UTC on 21st August. This lack of sharp directional change could be due to the model’s increased wavelength and height as previously described, which prevent the observed rapid shifts in wave direction. Despite some biases in wave features, including magnitude and timing of peak wave height, the overall performance of the modelled waves at the two NDBC locations are reasonable and demonstrates the model’s ability to capture general trends in storm induced wave behaviour during Hurricane Henri.~~

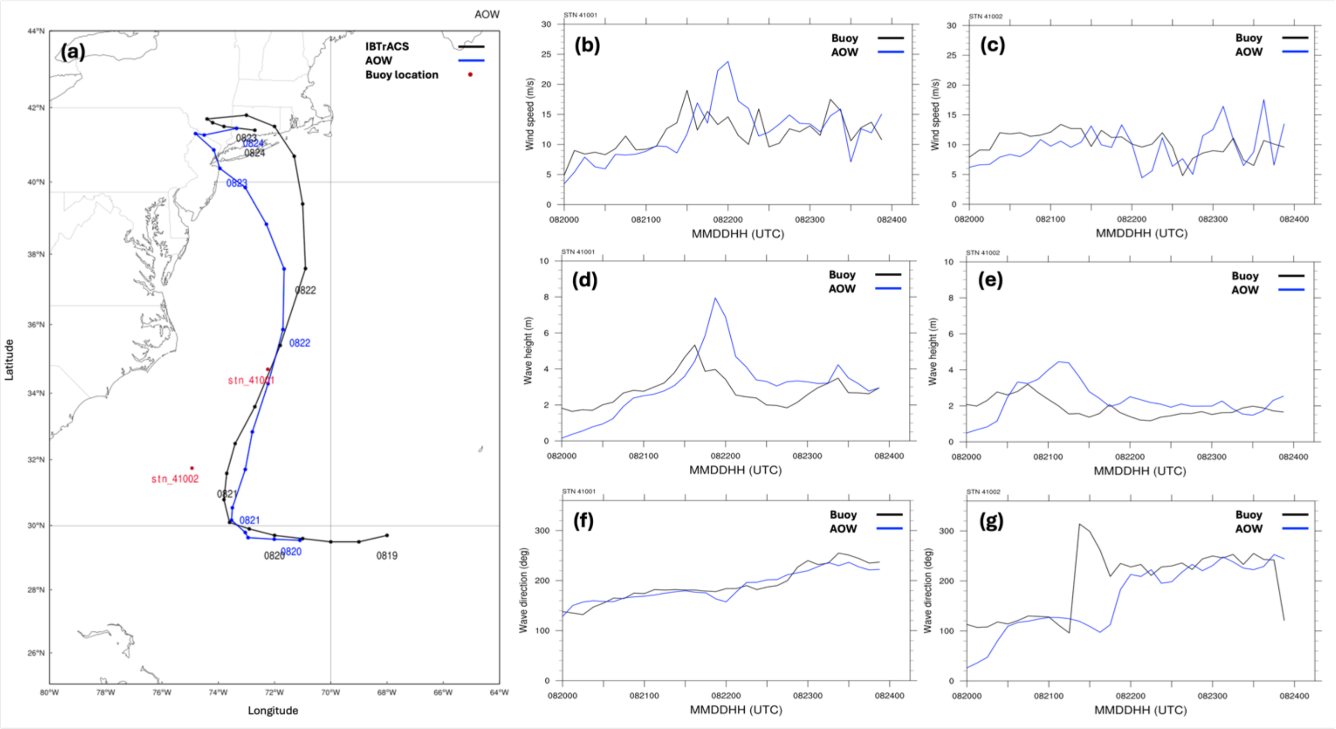

Figure 8. Comparison of the 'AOW' simulation (blue) with observations (black) for Hurricane Henri from 00 UTC 20 to 00 UTC 24 August 2021: (a) track, (b–c) wind speed (m/s), (d–e) significant wave height (m), and (f–g) wave direction. Panels (b), (d), and (f)

show data from station 41001, while (c), (e), and (g) show station 41002.

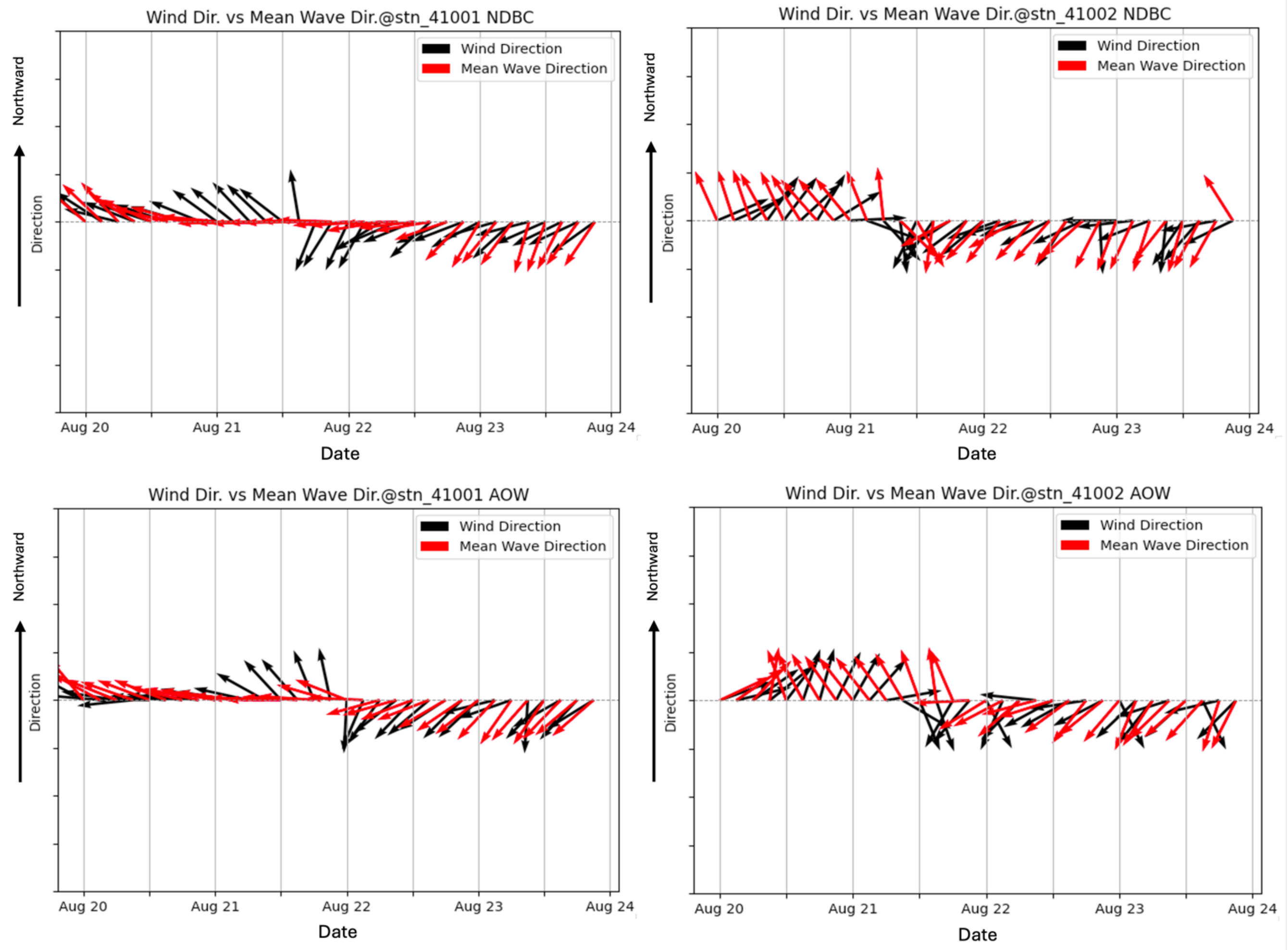

Figure 9. Time series comparison of surface wind direction and mean ocean surface wave direction at two NDBC buoy stations, 41001 (left column) and 41002 (right column), derived from NDBC buoys (top panel) and experiment 'AOW' (bottom panel).

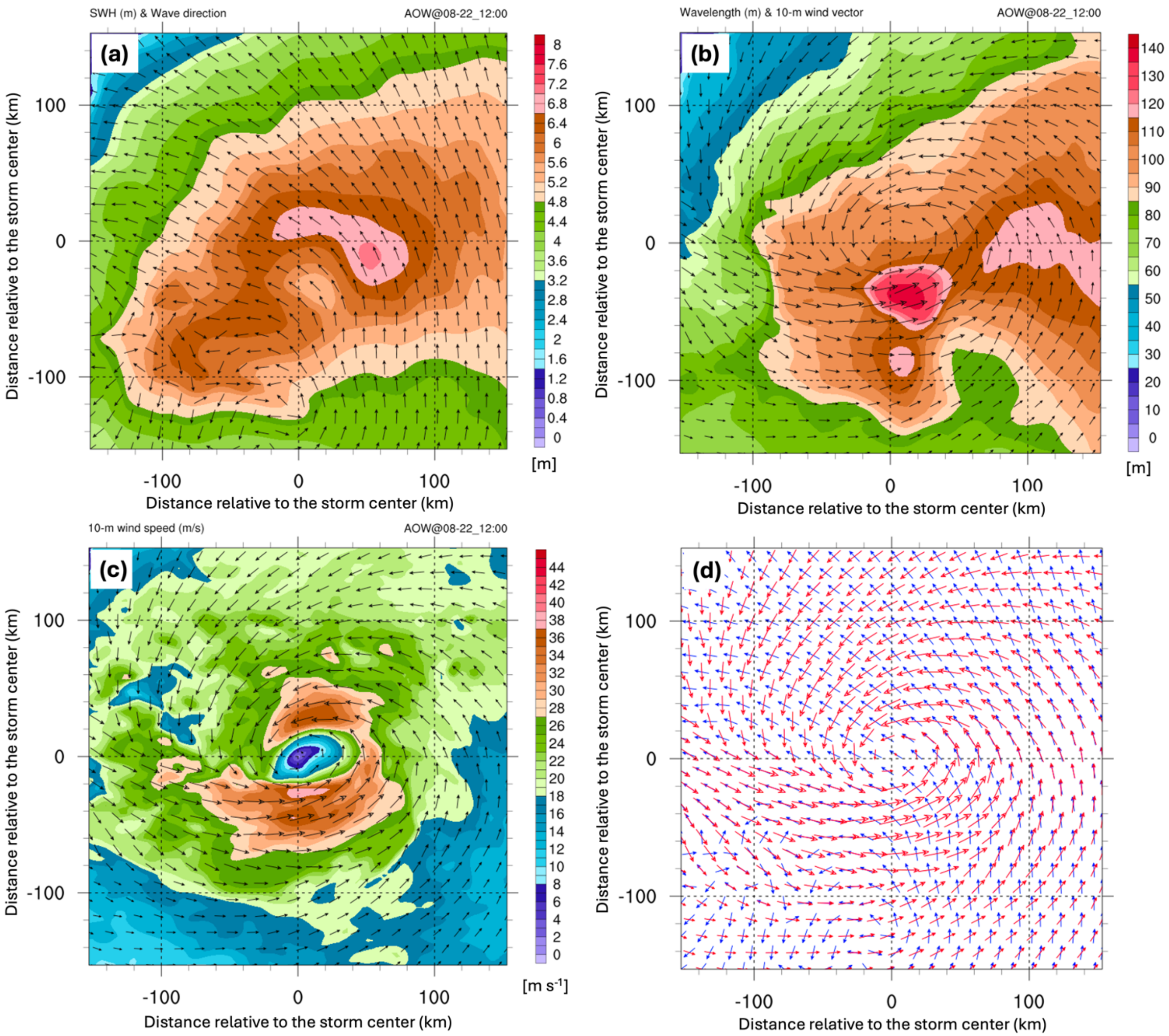

Figure 10. The fully coupled model output at 12 UTC on 22 August 2021 includes: (a) significant wave height (shaded; in meters) and wave direction, (b) mean wavelength (shaded; in meters) and 10-m wind, (c) 10-m wind speed (shaded; in m/s) and vectors, and (d) wave (blue) and wind (red) vectors. All plots are in a 300 × 300 km storm-centered domain, with a 20 m/s reference wind vector shown in panels (b) and (c).

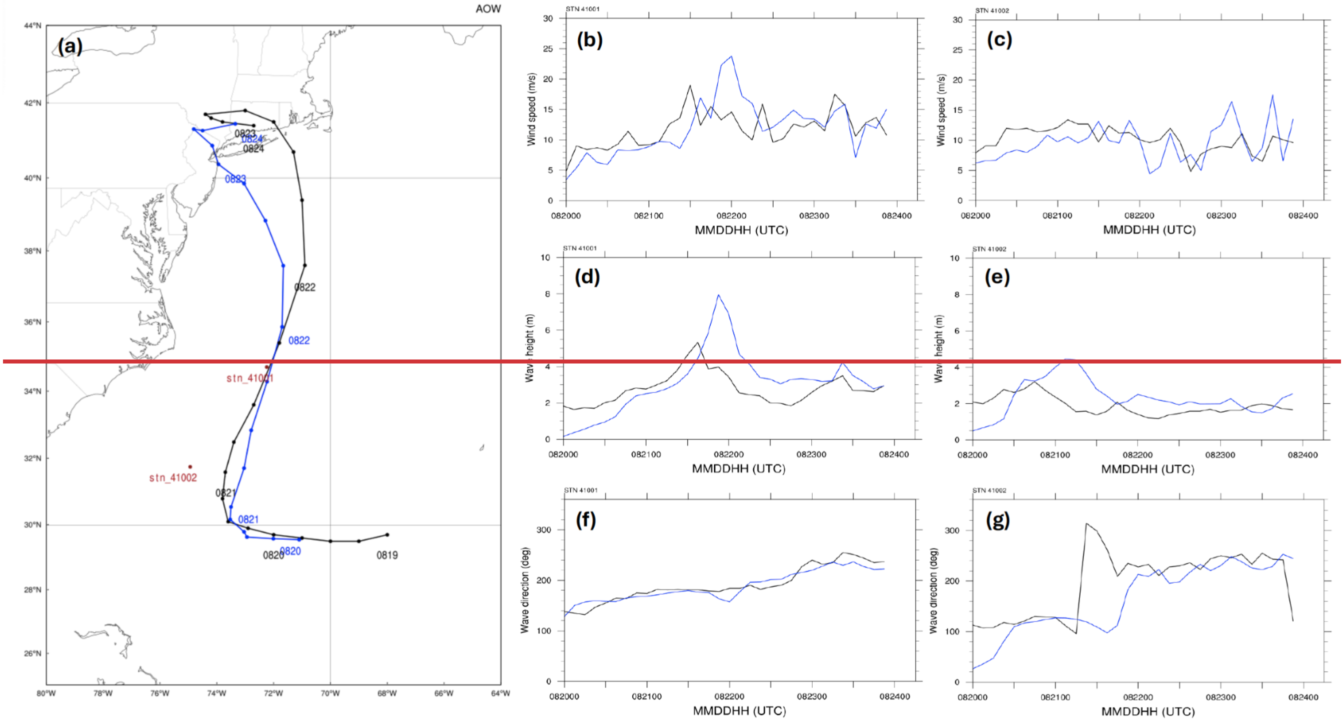

~~**Figure 10. Comparison of 'AOW' simulated in blue (a) track, (b)-(c) wind speed (m/s), (d)-(e) significant wave height (m), and (f)-(g) wave direction of Hurricane Henri with the observations in black from station 41001 (b),(d),(f) and station 41002 (c),(e),(g) during the period from 00 UTC on 20 August to 00 UTC on 24th August 2021.**~~

5~~4.3~~ Mechanisms Underlying the Improvement in the Fully Coupled Experiment

C~~So far we have learned that, c~~ompared to experiments 'A' and 'AO', 'AOW' reduces the overestimation of storm intensity (~~not only reduces the overestimation of storm intensity (represented by the~~ minimum SLP;~~,~~ Fig. 3) and~~but also~~ improves the storm-scale wind structure (Fig. 4), PDF distribution ~~and wind speed distribution~~ (Fig. 5), and profiles (Fig. 6) ~~compared to observations~~ from the near surface to the upper troposphere. ~~for Hurricane Henri (2021).~~ To understand~~examine the mechanisms behind~~ these improvements, we analyze ~~first analyse~~ SST and surface enthalpy flux ~~of~~in 'AOW' ~~and~~ versus 'AO' to assess the role of ~~compare them with those of 'AO' to examine ocean surface~~ wave-induced processes in Henri's evolution. Experiment 'A' is excluded since it is atmosphere-only and lacks ~~and their influence on the evolution of Henri. We opted out of experiment 'A' in this analysis, as it is an atmosphere standalone simulation and does not consider~~ atmosphere-ocean interactions.

Because ~~Since both~~ 'AO' and 'AOW' ~~simulations~~ have very similar storm tracks and ~~comparable~~ translation speeds, we can ~~are able to~~ isolate surface processes—SST, enthalpy flux, and surface roughness length (Z_0)—to evaluate their impact on storm intensity and evolution. In 'AOW', ocean surface waves affect Z_0, which regulates momentum, heat, and moisture exchange at the air–sea interface. In uncoupled simulations like 'AO', Z_0 depends solely on wind speed (e.g., via~~the surface properties,~~

~~including effects of SST, enthalpy flux, and surface roughness length on storm dynamics and evaluate how these factors contribute to differences in storm intensity and evolution. First, from a momentum transfer perspective, ocean surface waves characterize the surface roughness length (Z_0) of the ocean and regulate the exchange of momentum, in addition to heat and moisture, between the atmosphere and ocean. Without coupling the waves and the atmosphere, Z_0 or drag coefficient (C_d) is calculated solely based on wind speed (e.g.,~~ Charnock formulation’s formular where Z_0 is solely relying on the surface wind speed), ignoring wave effects. This limits capturing dynamic air–sea interactions during TCs, where sea state significantly influences momentum transfer and storm development. Focusing on 12 UTC, 22 August—about 12 hours before landfall when both simulations reach peak minimum SLP—reveals notable differences in Z_0 distribution (Fig. 11). In ‘AO’, the distribution and strength of Z_0 closely follow the surface wind speed through the Charnock relation. In contrast, ‘AOW’ simulation shows a different Z_0 pattern (e.g., Taylor and Yelland, 2001; Drennan et al., 2005; Shimura et al., 2017), with reduced values driven by wave dynamics, highlighting the significant role of waves in modulating air–sea momentum and energy exchange (Figs. 11a–b, e–f). Prior studies have shown that drag coefficient (C_d) saturates or even decreases once wind speeds exceed approximately 30-35 m s^{-1}, largely due to wave processes which dampen momentum transfer to the ocean (e.g., Donelan et al., 2004; Powell et al., 2003). Since surface roughness length (Z_0) is directly correlated with C_d via Monin-Obukhov theory, this saturation implies a corresponding weakening or plateauing of surface roughness.

The influence of ocean surface waves extends beyond modifying Z_0. Although ‘AOW’ exhibits stronger winds, it also shows lower SST and reduced surface enthalpy flux compared to ‘AO’ (Figs. 7l,p, and 11c-d). The primary driver of SST cooling under TCs is ocean vertical mixing. Storm-induced surface winds generate frictional stress, which drives upper-ocean currents and promotes evaporation. Vertical shear in these currents produces turbulence that mixes cooler subsurface water into the mixed layer, reducing SST (e.g., Zhou et al., 2023). This process occurs in both ‘AO’ and ‘AOW’. However, ‘AOW’ introduces additional vertical mixing through wave dynamics. As surface winds generate waves, momentum is transferred into the ocean. Breaking waves inject momentum deeper, enhancing shear and mixing. Long period, large wave height non-breaking waves that are generated by TCs further deepen the vertical mixing, amplifying SST cooling. These wave-induced processes in ‘AOW’ lead to cooler SSTs and lower enthalpy fluxes than in ‘AO’ (Fig. 11). Additionally, the reduced Z_0 in ‘AOW’ corresponds to a lower C_d resulting in less surface roughness and higher near-surface wind speeds due to the inclusion of wave effects.

~~). As a result, ‘AO’ might not accurately capture the dynamic interactions between the lower atmosphere and ocean surface during TCs where wave effects and varying sea surface conditions significantly impact momentum transfer and overall system evolution. We chose the time of 12 UTC on 22nd August 2021 to investigate these interactions in detail, focusing on how the inclusion of wave dynamics in the fully coupled experiment ‘AOW’ alters the estimate of surface roughness length and the subsequent effects on momentum and heat exchange during the hurricane's intensification phase. The timing is particularly significant, as it marks the moment when the simulated storms from both ‘AO’ and ‘AOW’ reached their peak minimum SLP, occurring about 12 hours prior to landfall. As shown in Fig. 11, ‘AO’ and ‘AOW’ simulate very different distributions of Z_0,~~

~~clearly demonstrating that ‘AO’ is solely a function of surface wind speed, while the Z_0 distribution of ‘AOW’ is distinct from the surface wind distribution. This implies that wave dynamics play a crucial role in shaping Z_0 (Figs. 11a,b,e,f).~~

~~The impact of including ocean surface waves is not limited to just the representation of Z_0. 'AOW' is associated with stronger winds, but lower SST, and surface enthalpy flux compared to ‘AO.’ The primary process responsible for cooling SST under TCs is ocean vertical mixing, as discussed. During such events, the storm's surface winds create stress on the ocean surface through friction, generating ocean currents in the mixed layer and momentum flux at the bottom of the atmosphere, leading to evaporation from the ocean surface. In addition to the evaporative cooling, vertical velocity shear of the currents in the upper ocean leads to turbulence, which mixes and entrains colder water from below the mixed layer, and reduces SST (e.g., Zhou et al., 2023). This process is represented in both 'AO' and 'AOW.' However, the inclusion of wave dynamics in 'AOW' adds additional vertical mixing through the following processes: the storm's surface winds build waves at the sea surface, and the momentum transfer from the atmosphere to the ocean grows and propagates these waves. When the waves break, momentum is transferred downward into the ocean currents, leading to vertical shear and thus vertical mixing. On the other hand, mixing induced by non-breaking waves penetrates much deeper, leading to a further reduction in SST, as previously discussed. This additional wave dynamics included in ‘AOW’ results in greater cooling in SST, leading to a reduced surface enthalpy flux compared with ‘AO’ (Fig. 11). The reduced Z_0 in ‘AOW’ corresponds to a lower C_d, meaning that the roughness – primarily due to the inclusion of waves – is less, which leads to higher wind speeds at the surface.~~

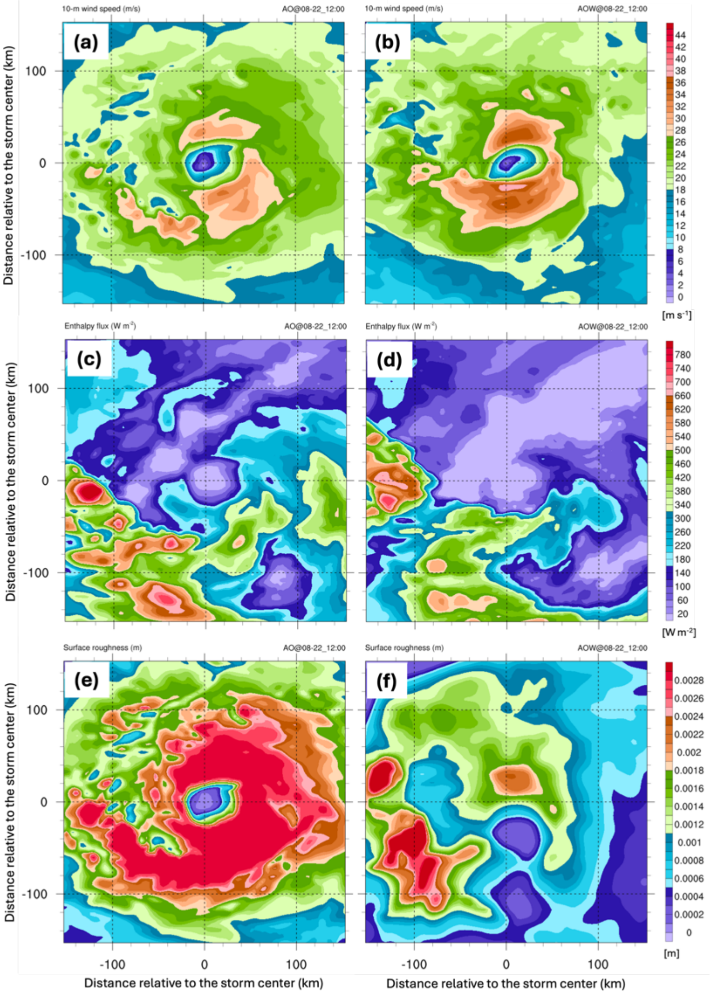

Figure 11. Distribution of (a)-(b) 10-m wind speed (m s^{-1}), (c)-(d) surface enthalpy flux (W m^{-2}), and (e)-(f) surface roughness length (m) derived from the experiment ‘AO’ (left column) and the experiment ‘AOW’ (right column) at 12 UTC on 22 August 2021. All distributions are displayed in a 300 km × 300 km storm-centered coordinate.

An important question remains regarding the discrepancy between minimum SLP and maximum wind speed in ‘AO’ and ‘AOW.’ simulations. Although ‘AO’ produces a lower minimum SLP, it shows weaker maximum wind speeds than ‘AOW’—despite higher surface enthalpy and momentum fluxes at peak intensity ~~Specifically, while ‘AO’ shows more intense (i.e., lower) minimum SLP than ‘AOW’, its maximum wind speed is weaker compared to ‘AOW’ at this time~~ (12 UTC on 22nd August; Fig. 3b-c and Figs. 11a-b). ~~despite being linked to greater surface enthalpy and momentum flux.~~ As discussed, this is due in part to the~~‘AO’ is linked to~~ higher Z_0 in ‘AO’, resulting from the absence of wave dynamics. . Increased Z_0 leads to greater frictional drag, reducing near-surface wind speeds. This enhanced friction contributes to stronger subgradient winds, where actual wind speeds fall below those expected from gradient wind balance. The imbalance between forces in the boundary layer is described by the agradient force (AF), defined as:

~~due to the absence of active wave dynamics in the simulation, resulting in reduced surface wind speeds from increased frictional drag. This can lead to stronger subgradient winds, where the actual wind speed is lower than what would be expected from the gradient wind balance. The relationship between tangential circulation and radial inflow in the boundary layer is described by the agradient force (Montgomery and Smith, 2014; Smith et al., 2009), which is defined as the difference between pressure gradient force and the sum of centrifugal and Coriolis forces in the form of~~

$$Agradient\ Force\ (AF) = -\frac{1}{\rho}\frac{\partial p}{\partial r} + \frac{V_t^2}{r} + fV_t \tag{3}$$

where p is pressure, r is the radial distance from the TC center, V_t is the tangential wind speed, ρ is air density, and f is the Coriolis parameter. Near the surface, both 'AO' and 'AOW' deviate from gradient wind balance due to friction, which reduces V_t, weakening both the Coriolis and centrifugal forces. With the pressure gradient force unchanged, this creates a negative agradient force ($AF < 0$), driving radial inflow. This inflow forms part of the storm's secondary circulation. Its strength can indicate the degree of deviation from gradient wind balance—stronger inflow implies greater subgradient winds. Table 4 clearly shows that 'AO' is associated with a stronger surface pressure gradient force, which, along with a higher Z_0, creates more favorable conditions for enhanced mass flux inflow. On the other hand, 'AO' exhibits weaker absolute angular momentum (AAM), defined as:

$$M = rV_t + \frac{1}{2}fr^2 \tag{4}$$

As shown in Equation 4, AAM is closely tied to the storm's rotational wind structure.Therefore, to better understand the discrepancy between 'AO' and 'AOW'—specifically why 'AO' has a stronger pressure gradient but weaker winds—we analyze the AAM budget, following Zhang and Marks (2015) and Zhao et al. (2022). The AAM budget equation used is:

$$\frac{\partial\langle M\rangle}{\partial t} = -\langle V_r\rangle\frac{\partial\langle M\rangle}{\partial r} - \langle w\rangle\frac{\partial\langle M\rangle}{\partial z} - \langle V_r'\frac{\partial M'}{\partial r}\rangle - \langle w'\frac{\partial M'}{\partial z}\rangle + F_r \tag{5}$$

where V_r and w denote radial wind speed and vertical wind component, respectively. Brackets $\langle\ \rangle$ denote azimuthal averages, and primes indicate deviations from the mean. The left-hand side represents the time tendency of azimuthally averaged AAM. The right-hand side includes contributions from mean radial advection, mean vertical advection, radial eddy transport, vertical eddy transport, and friction/residual term F_r. We hypothesize that the higher Z_0 in 'AO'—a result of the simplified Charnock relation—enhances angular momentum dissipation and reduces wind speeds despite a stronger pressure gradient. Figure 12 presents the AAM tendency, mean radial advection, mean radial eddy transport, and F_r terms over the period from 00 UTC to 12 UTC on 22 August 2021, during which both storms underwent steady intensification. The results indicate that the mean radial advection (Figure 12b, f) and F_r (Figure 12d, h) terms are particularly influential in determining the AAM tendency and tend to oppose each other. Within 100 km of the storm center, substantial AAM dissipation is observed in the F_r term for both simulations (Figure 12d, h), aligning spatially with regions of elevated Z_0. However, this dissipation is much more pronounced in ‘AO’ (Figure 12d), suggesting that its higher Z_0 values may unrealistically amplify angular momentum loss, leading to weaker surface winds despite lower minimum SLP. These findings highlight the crucial role of air-sea interactions, particularly those induced by waves and related processes, in accurately simulating the wind structure of TCs within the marine boundary layer which impact offshore wind turbines.

Table 4. Spatially averaged metrics within 10–60 km of the storm center, vertically integrated through the boundary layer up to 1.2 km above the ground level, at 12 UTC on 22 August 2021. PGF indicates pressure gradient force and is calculated at mean sea level.

Experiment	BL inflow mass flux ($kg\ m^{-3}$)	BL vertical mass flux ($kg\ m^{-3}$)	BL AAM ($m^2\ s^{-1}$)	PGF ($m\ s^{-2}$)
AO	1.93×10^4	1.34×10^3	1.55×10^{10}	-1.52×10^2
AOW	1.80×10^4	1.33×10^3	1.61×10^{10}	-1.46×10^2

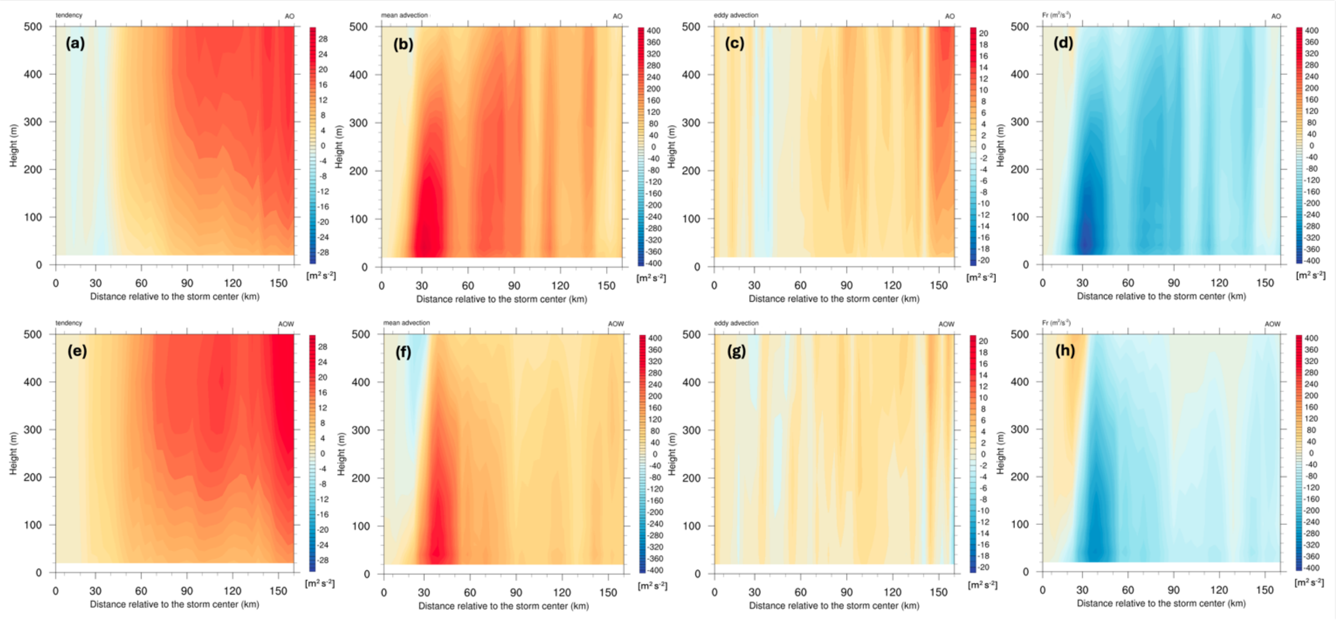

Figure 12. The radius-height plots of the terms in azimuthally averaged absolute angular momentum budget (a) time tendency term, (b) mean advection term, (c) eddy transport term, and (d) friction and residual term in ‘AO’ during the time from 00 UTC to 12 UTC 22 August 2021. The bottom panels (e)-(h) are the same as the top panels but for ‘AOW.’

~~where P is air pressure, r represents radius from the TC centre, V_t refers to tangential wind speed, and ρ is air density. Near the surface, both ‘AO’ and ‘AOW’ deviate from gradient wind balance due to the effects of friction. Friction reduces the~~

~~tangential wind speed, thereby weakening both Coriolis and centrifugal forces, while the pressure gradient force remains unchanged (negative agradient force: AF < 0). This imbalance results in a net inward force, driving inflow in the lower atmospheric layers (the secondary circulation). The magnitude of this inflow can be seen as an indicator of the deviation from the gradient wind balance, with stronger inflow corresponding to a greater degree of subgradient wind. The azimuthally averaged radial wind speed clearly shows that the enhanced inward flow towards the storm centre in the boundary layer in 'AO' compared with the 'AOW' (Fig. 12). In the boundary layer, stronger radial inflow transports additional absolute angular momentum (AAM) toward the storm's core, although friction disrupts the perfect conservation of AAM. As air moves inward, its radius decreases, causing tangential wind speeds to increase (as per the conservation of AAM). While friction within the boundary layer slows the tangential winds, the winds still strengthen near the core due to the influx of air masses. This increase in wind speed amplifies the outward centrifugal force, which is primarily counteracted by a greater inward pressure gradient force, resulting in a lower central pressure in the storm's core. In 'AO', even though the simulated storm is associated with stronger radial inflow through the process described above, the tangential winds along the storm centre are unable to increase relative to 'AOW' due to the additional friction effects over the ocean (Figs. 11 and 12). This extra friction in 'AO' is caused by an unrealistically calculated , which is only a function of surface wind speed. As surface wind speeds up, it generates more friction or drag on the ocean surface, which can further disrupt the conservation of AAM in 'AO.' As a result, the additional frictional dissipation of AAM in 'AO' leads to a reduction in the amount AAM available to drive wind's acceleration. Consequently, the wind speeds in 'AO' do not increase as much as expected despite the enhanced radial inflow. This explains the slower rate of intensification observed in 'AO' compared with its fully coupled counterpart, 'AOW' during the period from 06 UTC to 12 UTC on 22nd August. Note that as both simulated storms move through the baroclinic zone at this time, they may experience vertical wind shear. This can disrupt the typical inflow-outflow structure of tropical storms, leading to anomalous inflow at upper levels observed in Fig. 12.~~

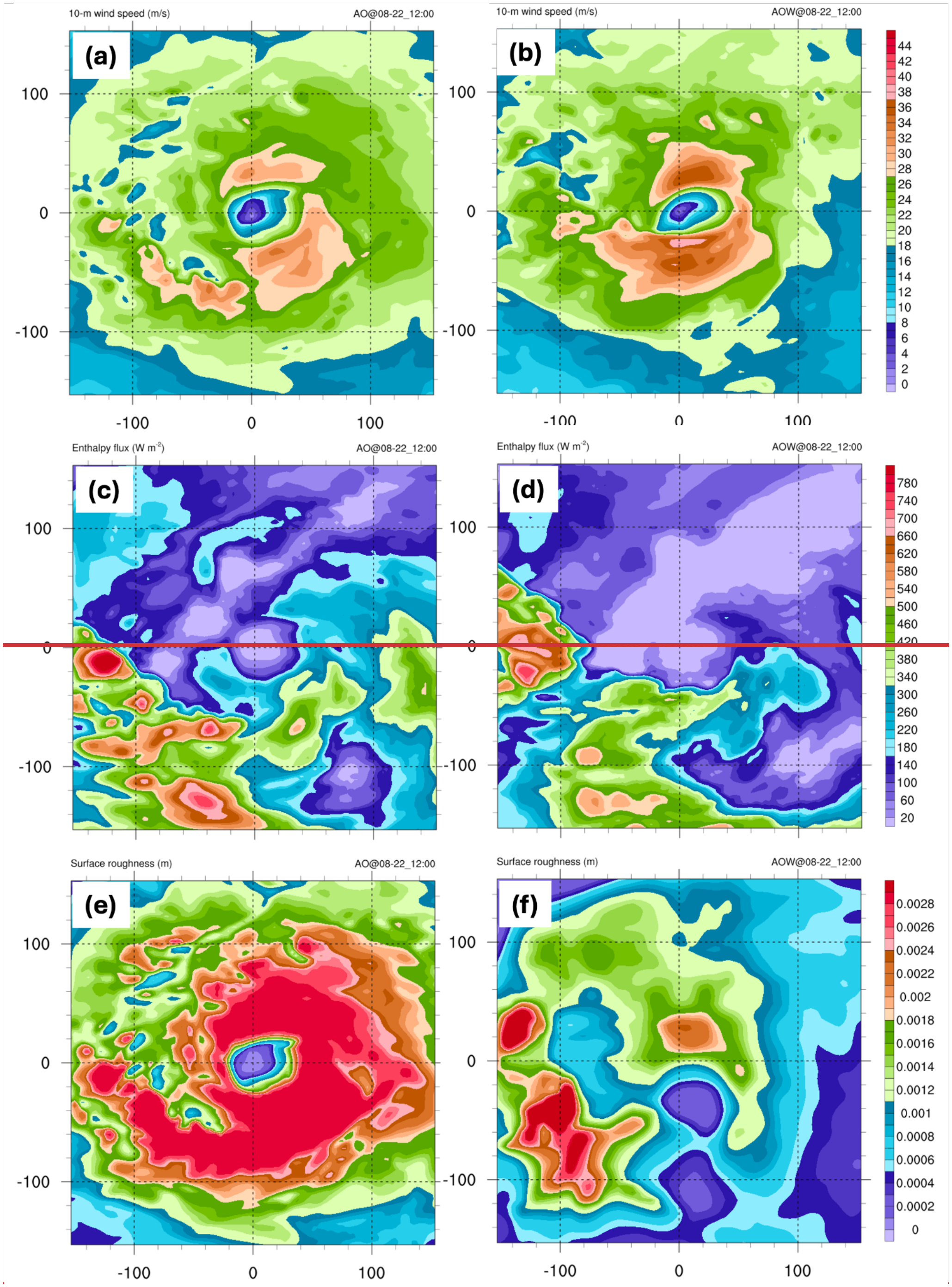

~~**Figure 11. Distribution of (a)-(b) 10-m wind speed (m s-1), (c)-(d) surface enthalpy flux (W m-2), and (e)-(f) surface roughness length (m) derived from the experiment 'AO' (left column) and the experiment 'AOW' (right column) at 12 UTC on 22nd August 2021. All distributions are displayed in a 300 km × 300 km storm-centred coordinate.**~~

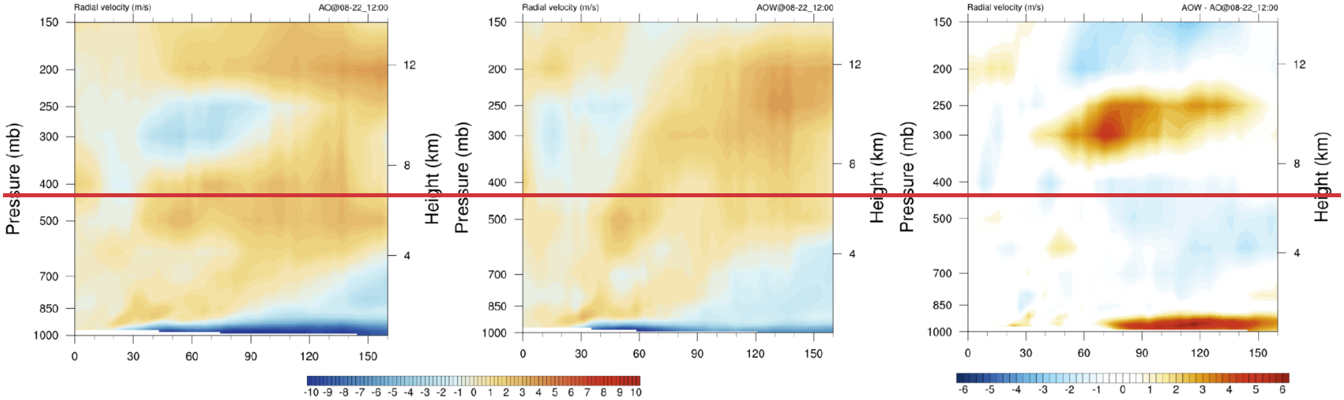

~~**Figure 12. The azimuthally averaged radial wind speed (m s^{-1}) for the (a) experiment 'AO', (b) experiment 'AOW', and (c) difference between 'AOW' and 'AO' at 12 UTC on 22nd August 2021.**~~

~~5 Implication for Potential Risks to Offshore Wind Energy~~

~~As the global demand for renewable energy continues to rise, offshore wind energy has emerged as a promising solution in the transition toward sustainable power generation. However, this opportunity comes with potential risks, particularly from TCs, which can generate extreme sea surface wave conditions, high wind speeds, and significant shear and veer between the ocean surface and hub heights (Wang et al., 2024a,b). Loads on offshore structures can arise from both aerodynamic and hydrodynamic forces and both act simultaneously on a turbine during a TC. In a design context, factors such as sustained wind speed, its relationship to wind gusts, the assumed vertical profile (shear) of the boundary layer, and wave heights and periods are crucial for calculating loads and are generally well understood. However, properties of the wind profile, including veer, as well as the temporal variability and directional dependence of wind and wave loads, remain less understood and are often not fully accounted for (Sanchez Gomez et al., 2023; Wang et al., 2024b).~~

~~5.1 Wind Veer~~

~~Wind veer is defined as the rate of change in wind direction with altitude (e.g., Churchfield and Sirnivas, 2018; Sanchez Gomez et al., 2023). Although the International Electrotechnical Commission (IEC) standards outlines the atmospheric conditions for weather extremes, including TCs, to guide the design of onshore (61400-1 IEC, 2019a) and offshore (61400-3 IEC, 2019b) wind turbines, wind veer is not accounted for in current design specifications (Sanchez Gomez et al., 2023). This omission remains despite its potential on turbine performance (Bardal et al., 2015; Gao et al., 2021) and loads (Churchfield and Sirnivas, 2018; Kapoor et al., 2020; Robertson et al., 2019; Sanchez Gomez et al., 2023). Large changes in wind direction with increasing altitude, driven by extreme events, can be destructive for wind turbines. For instance, a disruption in the grid connection caused by these extreme events may prevent the turbines from yawing into the wind, or the wind direction may change too quickly for the yaw control system to respond effectively, resulting in increased mechanical loads on the turbine components and~~

~~potential damage to the structure. To evaluate the wind veer simulated by ‘A’, ‘AO’, and ‘AOW’ simulations, we estimated wind veer by calculating the difference in wind direction at multiple hub heights ranging from 100 m to 200 m in 10-m intervals relative to the bottom (z = 30 m) of the turbine rotor layer. These results were then compared with dropsonde observations at three different locations relative to the storm centre (~91 km to the left: yellow circle - called point A, ~40 km to the right: green circle - called point B, and ~104 km to the right: red circle - called point C), as shown in Fig. 3d.~~

~~Firstly, the observations show that wind veer varies along the radius of the storm, with the veer noticeably increasing as it approaches the centre of Henri around 00 UTC on 22 August. For example, at 150 m hub height, wind veer is 0.028°/m at point A (to the left of the centre), 0.09°/m at point B (the closest point to the centre), and 0.06°/m at point C (to the right of the centre). In addition, it is apparent that wind veer is greater on the right side of the storm compared to its left side counterpart at all hub height levels (Figs. 13a-c). All three simulations significantly underestimate the wind veer, especially on the right side of the storm (Figs. 13b-c). Furthermore, the greater veer observed on the right side of the storm in the dropsonde data is not clearly captured in any of the simulations. Nevertheless, all three simulations do reasonably capture the general trend that wind veer increases as it approaches the centre of the storm. Azimuthally averaged wind veer at 150 m relative to 30 m at 00 UTC on 22nd August, shown in Fig. 13d, clearly displays that the wind veers associated with the simulated storms gradually decrease with radius in all three simulations. Among the three simulations, ‘AOW’ better matches the magnitude of the veer at all levels at the three dropsonde locations although it still largely underestimates the values (Fig. 13). The largest veer across the radius is seen in ‘AOW,’ consistent with the Figs. 13a-c.~~

~~Wind veer and shear can be influenced by several factors, with atmospheric stability, surface friction, and subsequent dynamic and thermodynamic processes, such as both mechanical- and buoyancy-driven turbulence and vertical mixing (e.g., Englberger and Lundquist, 2020; Murphy et al., 2020), all of which play key roles. For example, in stable atmospheric conditions, wind veer and shear are typically more pronounced within the boundary layer, as stratification inhibits vertical mixing. In contrast, under unstable conditions, enhanced turbulence promotes mixing, which can reduce the magnitude of wind veer and shear by redistributing momentum. Additionally, surface friction slows near-surface winds, reducing their speed and altering their direction, which creates a vertical gradient in wind speed and direction that contributes to wind veer and shear. In the light of this, we examine these factors to understand how the three simulations differ in simulating these properties and how they affect the representation of wind veer. Over the ocean, surface enthalpy flux represents the heat and moisture exchanged at the atmosphere-ocean interface, with a lower flux suggesting a more stable lower boundary layer, while a higher flux is associated with a less stable one. Regarding turbulence, turbulent kinetic energy (TKE) is commonly used as a proxy for turbulence in the atmospheric boundary layer, representing the energy associated with turbulent motions. Thus, we use TKE to assess the intensity of turbulence in the simulated storms. Figure 14 indicates horizontal distributions of surface roughness length, surface enthalpy flux, and TKE at 30 m above the ground for all three simulations at 00 UTC on 22nd August. Consistent with our previous findings, Z_0 in 'A' and 'AO' exhibit similar magnitudes and distributions, as both are driven by surface wind. In contrast, Z_0 in 'AOW' is significantly weaker and displays a distinct spatial distribution, characterized by ocean wave processes (Figs. 14a-c). Similarly, the surface enthalpy flux in 'AOW' is the weakest among the three, aligning with our previous findings~~

~~(Figs. 14d-f). In other words, ‘AOW’ is in a condition where decreased surface roughness and weaker surface enthalpy flux act to suppress turbulent mixing. In relatively unstable atmospheric conditions, such as in 'A' and 'AO,' turbulence is more pronounced due to buoyancy-driven mixing, which tends to redistribute momentum more evenly. Further, stronger Z_0 leads to greater velocity shear between the atmosphere near the surface and above. This shear creates turbulent eddies that mix the atmosphere. Therefore, more surface friction implies that the wind near the surface slows down more, creating stronger turbulence that mixes the boundary layer. Figure 14 supports this idea, demonstrating that the experiments ‘A’ and ‘AO’ are associated with greater surface enthalpy, stronger Z_0, and higher TKE compared to those in ‘AOW.’ Strong turbulence generated by both mechanically and thermodynamically tends to reduce wind veer by mixing momentum, while weaker turbulence likely allows the veer to persist within the boundary layer (e.g., Sanchez Gomez and Lundquist, 2020; Stull 1988). Thus, the weaker turbulence linked to the lower Z_0 in ‘AOW’ may restrict vertical mixing near the hub heights and below, allowing the wind veer to remain more pronounced and closer to the observed values compared to the other two simulations. It is important to note that the 3 km grid spacing used in the atmospheric model is still too coarse to accurately resolve fine-scale turbulence processes. For instance, Li et al. (2021) highlighted that mesoscale models are incapable of properly capturing small-scale features such as roll vortices, which are large turbulent eddies commonly found in a hurricane's boundary layer. Furthermore, Müller et al. (2024) discussed how the lower wind veer values simulated in mesoscale modeling during Typhoon Megi, compared to those reported by Sanchez Gomez et al. (2023), could be attributed to the higher resolved wind veer variability in large eddy simulations (LESs). This limitation likely contributes to misrepresenting wind veer magnitude (underestimations) in all three simulations when compared to the observations. Nevertheless, this finding underscores the ability to capture critical atmosphere-ocean interactions, such as cold wakes, momentum transfer, surface stress, and boundary layer dynamics, particularly in the context of wind veer assessment. This suggests that relying solely on atmospheric-only models to quantify wind veer, as previously studied, may lead to inaccuracies and underestimations, underscoring the importance of incorporating atmosphere-ocean-wave interactions in future simulations.~~

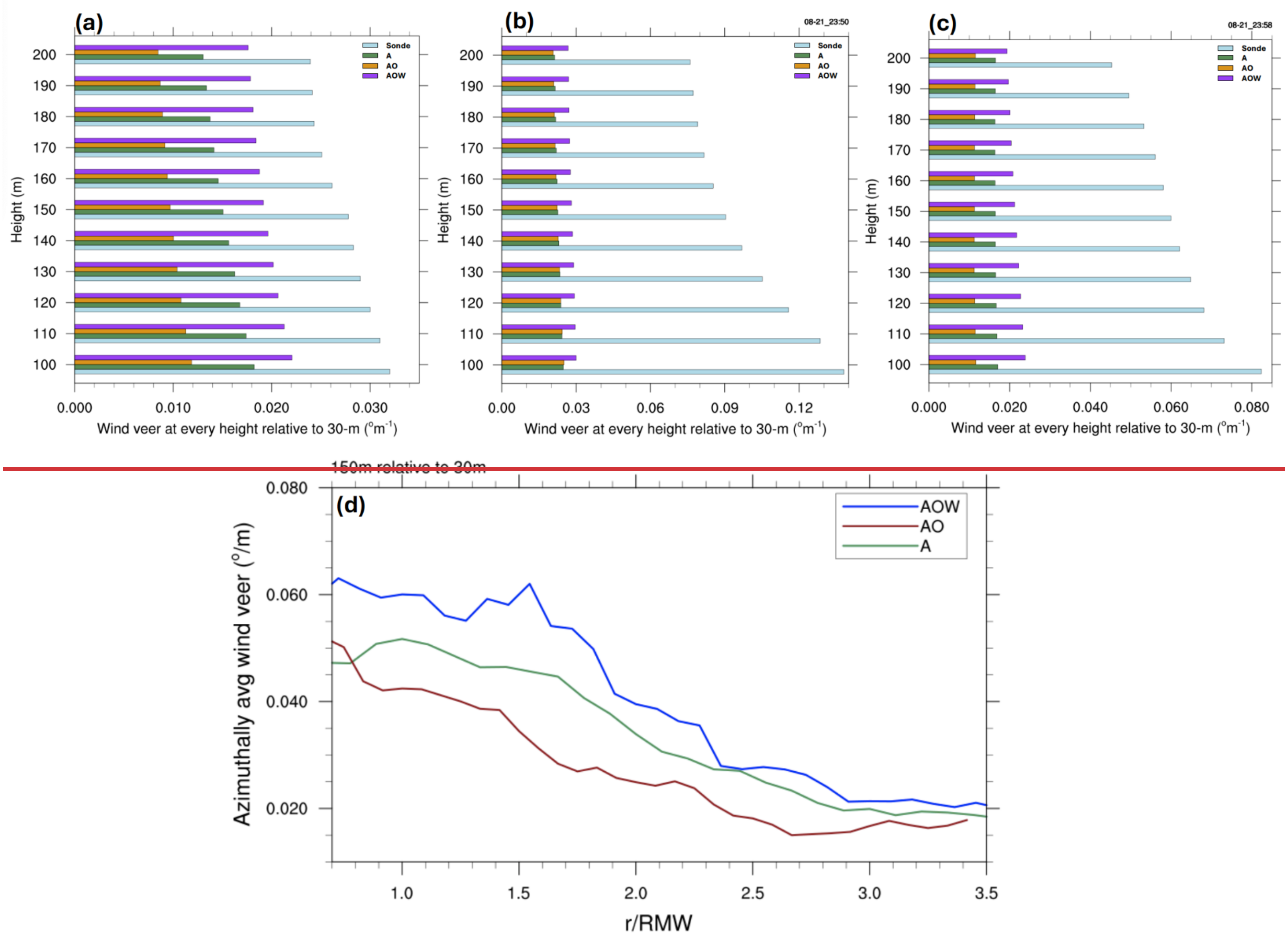

~~**Figure 13. Wind veer at multiple hub heights (ranging from 100 m to 200 m in 10-m intervals) relative to the bottom of the turbine rotor layer (z = 30 m) for (a) point A, (b) point B, and (c) point C. Point A is represented by a yellow dot, point B by a green dot, and point C by a red dot in Fig. 3d. (d) Azimuthally averaged wind veer (° m^{-1}) for the experiments 'A', 'AO', and 'AOW' at 00 UTC on 22nd August 2021. In (d), RMW denotes the radius of maximum wind, and r represents the radius relative to the storm centre.**~~

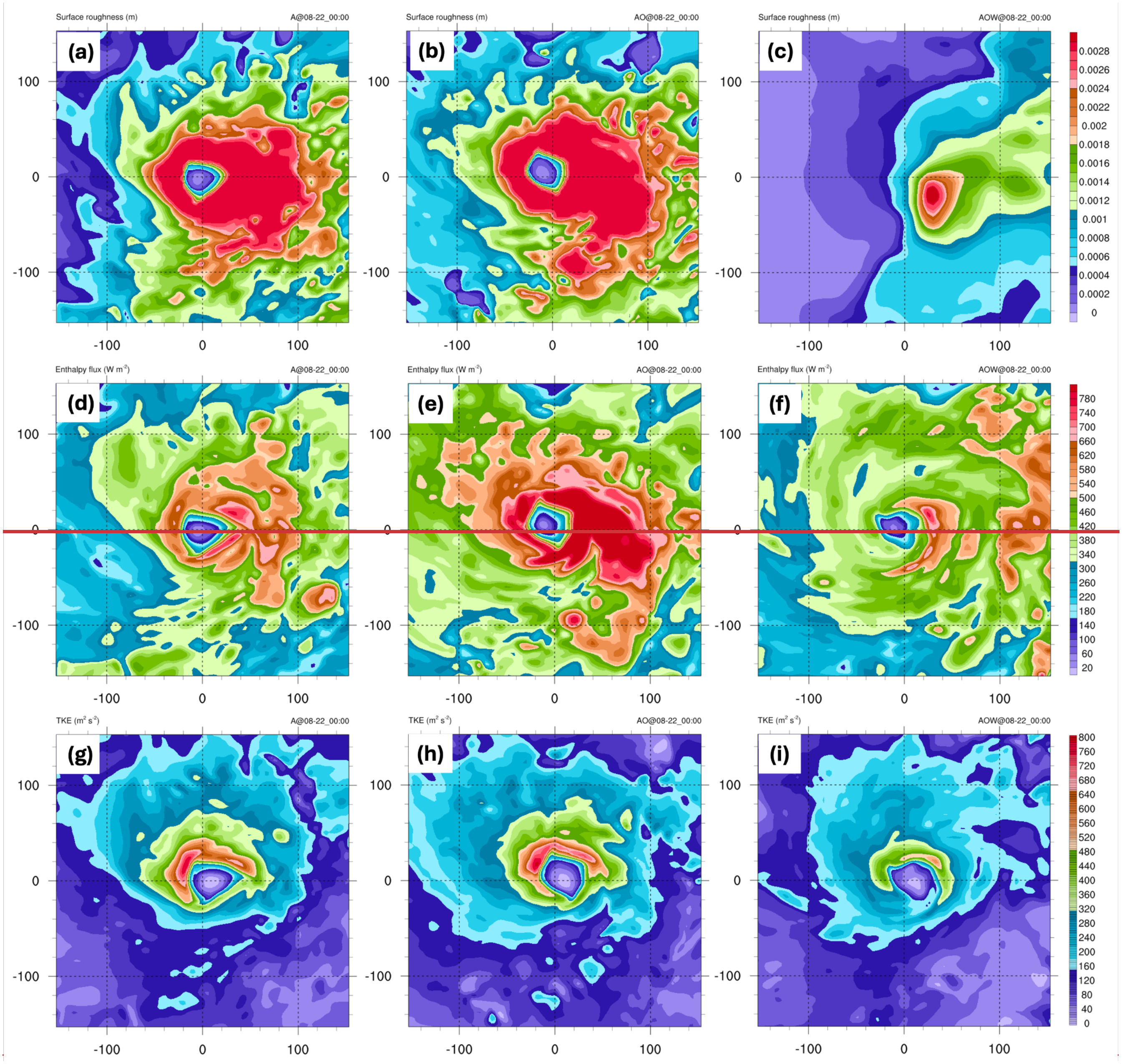

~~Figure 14. Distribution of surface roughness length (m; upper panel), surface enthalpy flux ($W m^{-2}$; middle panel), and turbulent kinetic energy ($m^2 s^{-2}$; middle panel) for the experiments 'A' (left column), 'AO' (middle column), and 'AOW' (right column) are shown at 00 UTC on 22nd August 2021.~~

~~5.2 Wind-Wave Misalignment~~

~~Wind-wave misalignment is another critical risk for offshore infrastructure that atmospheric-only models cannot estimate given the lack of interaction between the atmosphere and ocean surface. Wind-wave misalignment can cause increased structural~~

~~loads on offshore wind turbines (discussed below), leading to fatigue damage and reduced operational lifespan. Figure 15 displays ocean surface wave information, including significant wave height, wave direction, and wavelength and 10-m wind vector associated with the simulated in 'AOW' at 12 UTC on 22nd August. Previous studies have shown that the storm-induced wave field around a hurricane is asymmetric, with the highest waves, as measured by significant wave height, typically observed in the front-right quadrants of the storm (e.g., Chen et al., 2013; Wright et al., 2001). This typical characteristic is also evident in our simulation, showing the highest significant wave heights in the right and front-right quadrants (Fig.15a). Henri was heading northwest at 12 UTC on 22nd August 2021. In a moving storm, the waves to the right of the storm tend to grow over time (Chen et al., 2013). This happens because the waves on the right side have a longer distance to travel and grow, compared to the waves on the left side of the storm (Figs. 15a-b). In addition, directional misalignment of winds and waves is evident on all sides of the storm, except the right side, consistent with prior study (Chen et al., 2013; Figs. 15d). This misalignment is clearly represented in Fig. C1, which illustrates the time series comparison between surface wind direction and mean wave direction at two NDBC buoy stations, 41002 and 41002. The figure highlights how the wave directions deviate from the wind direction, as clearly observed in both NDBC buoys and the 'AOW' simulation, indicating complex interactions at play.~~

~~These findings have significant implications for offshore wind energy operations and maintenance. When wind and wave directions are not aligned (i.e., when they come from different directions), this creates substantial relative motion between different parts of the wind turbine, specifically between the root (base) and the hub. This misalignment can lead to increased movement or strain between these components. In contrast, when wind and waves are aligned, they combine in a way that generates the highest impact velocities. This indicates that the forces acting on the turbine are stronger when the wind and waves are moving in the same direction. In such conditions, with the two aligned, the turbine faces more severe impacts and is at a higher risk of failure. Some studies have examined wind fields brought by TCs and their impacts on offshore wind turbines (e.g., Sanchez Gomez et al., 2023; Wei et al., 2017; Itiki et al., 2023). However, most of these studies use either atmospheric only models or empirical, parametric models that do not fully capture the complex interactions between wind and wave forces during extreme events. This limitation makes it challenging to accurately predict the operational risks faced by offshore turbines located in the hurricane belt. To assess this aspect, the models that incorporate atmosphere, ocean, and waves components, are essential. Our fully coupled model with the three components can provide a realistic representation of wind and wave behaviours, helping to predict wind-wave misalignment effectively. This allows for better assessment of the forces acting on offshore wind turbines, enabling more informed design decisions and improved operational strategies to enhance the longevity and reliability of wind turbine infrastructure.~~

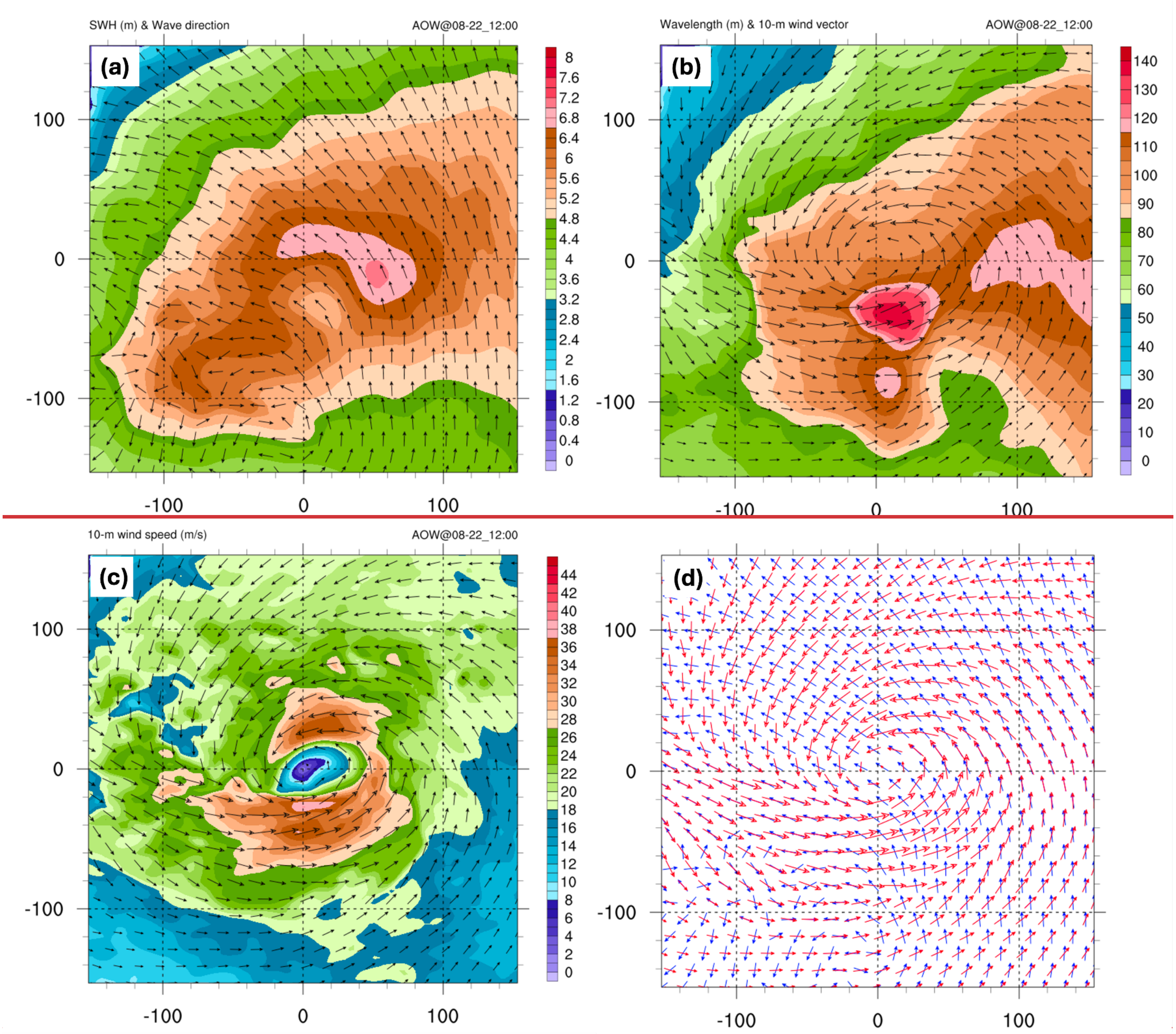

~~Figure 15. The fully coupled model simulated the following at 12 UTC on 22nd August 2021: (a) significant wave height (shaded; in meters) and wave propagation direction (vector), (b) mean wavelength (shaded; in meters) and 10-m wind (vector; in m/s), (c) 10-m wind speed (shaded; in m/s) and wind vector (in m/s), and (d) wave propagation direction vector (blue) and 10-m wind vector (red). The figures are displayed in a 300 km by 300 km storm-centered coordinate system. A reference wind vector of 20 m/s is shown in panels (b) and (c).~~

6 Summary and Discussion

Previous studies of TC wind fields and their impacts on offshore wind turbines have primarily relied on atmosphere-only or empirical models, which neglect critical interactions among the atmosphere, ocean, and waves. This limitation hampers the accuracy of risk assessments for offshore wind infrastructure, particularly in hurricane-prone regions. ~~In t~~This study~~, we~~ developed a fully coupled model~~l~~ing system (C-WFS) utilizing WRF, FVCOM, and SWAN to simulate ~~realistically capture~~ atmosphere-ocean-wave feedback on TC development and assess ~~explore its~~ implications for offshore infrastructure. U~~, such as offshore wind turbines. We evaluated the performance of this coupled modeling system u~~sing Hurricane Henri (2021) as a case study, chosen for ~~selected for~~ its impact on the ~~to the densely populated~~ U.S. Northeast and available airborne observations, we ran t~~nearby offshore wind lease area, as well as the extensive airborne observations available. T~~hree experiments of ~~with~~ increasing complexity: ~~in atmosphere-ocean-wave coupled exchange processes —~~'A', 'AO', and 'AOW.'~~—~~ These were evaluated against observations. A~~were conducted and validated against a diverse range of observations, including IBTrACS, airborne Doppler radar, dropsonde data, as well as both in-situ and satellite-based SST and wave measurements. The results show that, while a~~ll simulations ~~ed storms~~ overestimated intensity in terms of minimum SLP, but the fully coupled ~~simulation~~ 'AOW' reduced~~s~~ this bias ~~overestimation~~ during ~~both the~~ development and weakening stages. ~~Improvements are also evident in the 3-D storm structure, where~~ 'AOW' also better captured 3D storm structure, especially low-level winds critical to coastal and offshore energy infrastructure. This improvement is attributed to wave-induced ocean mixing (cooling SST) and reduced surface roughness, resulting in more realistic wind fields and lower frictional loss of angular momentum. In contrast, ‘AO’, which lacks wave coupling, exhibited excessive surface roughness from simplified wind only dependent parameterization, causing greater frictional dissipation and weaker tangential winds despite a deeper central pressure. These results highlight the importance of including wave dynamics and incorporating dynamics and therodymaic feedback among all three components for accurate TC intensity and structural forecasts.

The model also captures wind-wave misalignment and alignment, key processes often overlooked but crucial for evaluating structural loads, fatigue, and operational risks. Together, these enhancements yield a more realistic representation of storm evolution, intensity, and structure, underscoring the importance of fully coupled modeling systems for accurate risk assessments and the development of resilient offshore wind infrastructure.

While this study applied C-WFS framework to ~~more accurately represents wind profiles across the entire atmosphere, including at low altitudes, where the actual risks to offshore wind energy infrastructure occur. The enhanced performance of the fully coupled model is primarily attributed to ocean wave-induced mixing, which leads to further cooling of the SST. Additionally, the reduced surface roughness length and lower drag coefficient associated with atmosphere-ocean-wave interactions in 'AOW' simulation help maintain a more realistic dynamical representation of the storm structure. In contrast, excessive friction and surface roughness length driven by simplified parameterization (i.e., Charnock relation), in 'AO' simulation, result in increased frictional dissipation of AAM as surface winds strengthen. This additional frictional dissipation, caused by the unrealistically driven surface roughness length over the ocean, weakens tangential wind acceleration, thereby limiting the intensification of the storm during its peak (from 06 UTC to 12 UTC on 22nd August 2021). As a result, 'AO' shows weaker storm wind speeds despite having a more intense minimum SLP compared to 'AOW' during this period. This suggests that incorporating wave dynamics in 'AOW' plays an important role in accurately simulating TC behaviour, ultimately enhancing predictive capabilities for storm intensity and structure.~~

~~Additionally, the fully coupled 'AOW' experiment is characterized by weaker surface enthalpy, leading to a more stable atmospheric boundary layer, reduced surface roughness, and lower TKE, all resulting from an improved representation of dynamic and thermodynamic processes through coupled interactions. This leads to a more realistic simulation of wind veer, with values closer to observations compared to the other two simulations. This finding indicates that, depending on location, the coupling of ocean and waves can significantly affect wind veer, which is not considered in the current IEC standard (Sanchez Gomez et al. 2023). Moreover, the model effectively captures wind-wave misalignment in comparison to buoy observations. This misalignment poses a critical risk to offshore infrastructure, which atmospheric-only and atmosphere-ocean coupled models are unable to predict.~~

~~Although we used~~ Category 1 Hurricane Henri and highlighted the role of air-sea interactions in TC structure and intensity, it has not yet been applied to stronger storms or included sea spray effects, both of which are current limitations we are actively addressing. A key motivation behind this work is to better understand how coupled dynamics modulate TC wind fields across different intensities, particularly in regions with offshore wind farms, where storm structure and intensity can directly affect turbine loading, resilience, and operational risk.

~~to validate the newly developed fully coupled model (C-WFS) and to highlight the impact of coupling processes on the intensity, structure, and evolution of TCs, the same framework has also been tested for higher-category hurricanes, including Laura (2020), a Category 4 storm that underwent rapid intensification. The results reveal similar trends, with ocean waves contributing to a decrease in hurricane intensity. However, consistent with prior research (e.g., Yamaguchi et al., 2017; Zhao et al., 2022), the atmospheric-only model tends to underestimate the intensity of high-category TCs, particularly for those with minimum SLP near or below 940 hPa. As a result, the fully coupled model further underestimates the intensity of these high-category storms due to additional wave-induced ocean mixing and subsequent cold wakes. Some previous studies (e.g., Zhao et al., 2017, 2022; Zweers et al., 2015) suggested a promising remedy for this issue, such as incorporating sea spray parameterization. For instance, Zhao et al. (2017, 2022) successfully reproduced the intensities of Typhoons Megi (2010) and Haiyan (2013), both Category 5 equivalent super typhoons, using a fully coupled model that incorporated sea spray parameterization. They demonstrated that sea spray increases the enthalpy flux at the atmosphere-ocean interface, leading to a warmer boundary layer and a more unstable surface layer, which, in turn, provide positive feedback for TC intensification. On the other hand, a recent study (Barr and Chen, 2024) examined the role of sea spray in TC dynamics, showing that its effects are dependent on the storm's intensity. For weaker TCs, such as Category 1 storms, sea spray tends to inhibit intensification due to evaporative cooling in the boundary layer, acting as negative feedback. However, as a TC strengthens (e.g., Category 2 or higher), increased spray production begins to contribute positively by warming the boundary layer and enhancing deep convection near the eyewall. This transition highlights spray's dual role: initially opposing intensification in weaker storms but eventually supporting rapid intensification in stronger ones, particularly major hurricanes. While this study is highly informative and pioneering in demonstrating spray's dual role, its hypothesis is based on only four TCs, limiting the~~

~~generalizability of its conclusions. The precise impact of sea spray on TC structure and intensity remains an open question, warranting further research across a broader range of TC events. In this study, sea spray parameterization is not included in the C-WFS modelling system. However, as part of our ongoing research, we are integrating sea spray into the system to investigate its impact on TC behaviour across various storm intensities. Advancing this work represents a crucial step toward improving TC simulations and deepening our understanding of the associated enhancements.~~

Another open question is how the ~~aspect that remains unclear is the impact of the~~ horizontal resolution of ~~the~~ ocean components influences TC development in coupled models. While it is well established that finer atmospheric resolution improves storm intensity forecasts ~~on TC development within the atmosphere-ocean coupled modelling framework. While the sensitivity of the atmospheric model's resolution to TC representation is well-established, with general consensus suggesting that reducing horizontal grid spacing improves the accuracy of storm intensity predictions~~ (e.g., Gentry and Lakmann, 2010; Taraphdar et al., 2014; Prein et al., 2015), the effects of ocean resolution are less ~~is~~ understood. Higher-resolution ocean grids can better resolve mesoscale and submesoscale features such as eddies and fronts, which influence SST patterns, air-sea fluxes, and upper-ocean mixing—factors critical to storm intensity and evolution (Zhang et al., 2023). These processes modulate SST cooling and ocean heat content redistribution during storm passage. Unlike traditional nested-grid approaches (e.g., in COAWST), C-WFS uses an unstructured mesh that smoothly transitions across resolutions, avoiding boundary artifacts. This flexibility makes C-WFS particularly well suited to explore how ocean resolution affects coupled dynamics and TC behavior—an area we aim to investigate in future work.

In parallel, this modeling framework presents a valuable opportunity to assess whether current IEC (2019a, 2019b) standards for wind conditions, such as wind shear, veer, and turbulence are adequate for regions prone to TCs. We are currently performing a comprehensive analysis using this fully coupled model to characterize the representation of these wind parameters, potentially informing revisions to design criteria that improve the structural resilience and reliability of offshore wind turbines under TC-induced loading conditions.

~~about how the resolution of ocean components influences TC development. Higher ocean resolution allows for a more detailed representation of mesoscale and submesoscale features (e.g., eddies and fronts affecting SST patterns, Zhang et al., 2023) and their associated atmosphere-ocean interactions, such as heat fluxes, momentum transfer, and upper-ocean mixing processes. These features likely play a critical role in modulating storm-induced SST cooling, redistributing ocean heat content, and influencing the energy supply to TCs. As previously discussed, C-WFS employs an unstructured mesh grid, enabling seamless transitions between coarse and fine resolutions. This approach removes the need for nested grids, commonly used in existing fully coupled models (e.g., COAWST), which can introduce boundary artifacts. Consequently, C-WFS is uniquely equipped to investigate how varying horizontal ocean resolutions affect coupling dynamics and storm development—an area that will be thoroughly explored in future studies.~~

Code and data availability. The WRF model (Version 4.5.1) is described by Skamarock et al. (2019), and its code is publicly available from https://github.com/wrf-model/WRF (University Corporation for Atmospheric Research, 2019). The code for FVCOM (Version 4.3.1., Chen et al., 2003, 2013) for ocean circulation model is publicly available at https://github.com/FVCOM-GitHub/fvcom. The SWAN (Version 41.01, Booij et al., 1999) is a third-generation spectral wave model developed at Delft University of Technology that computes random, short-crested wind-generated waves in coastal regions and inland waters (http://swanmodel.sourceforge.net/). HYbrid Coordinate Ocean Model (HYCOM; Cummings and Smedstad, 2014) analysis data used for ocean model forcing is available at http://hycom.org/dataserver/. NCEP provides Global Forecast System (GFS; NCEP, 2015) data, which is used as atmospheric forcing data, available at https://www.nco.ncep.noaa.gov/pmb/products/gfs/. The OSTIA (Good et al., 2020) global sea surface temperature provides daily maps of foundation sea surface temperature at 0.05 ° × 0.05 ° available from https://data.marine.copernicus.eu/product/SST_GLO_SST_L4_REP_OBSERVATIONS_010_011/description. The NCL and Python codes for performing analysis and visualization are available at https://www.ncl.ucar.edu/ and https://www.python.org/downloads/, respectively. All simulation data are available from the authors upon request.

~~Appendix A: Radial profile of wind speed from the airborne Doppler radar and the three model simulations~~

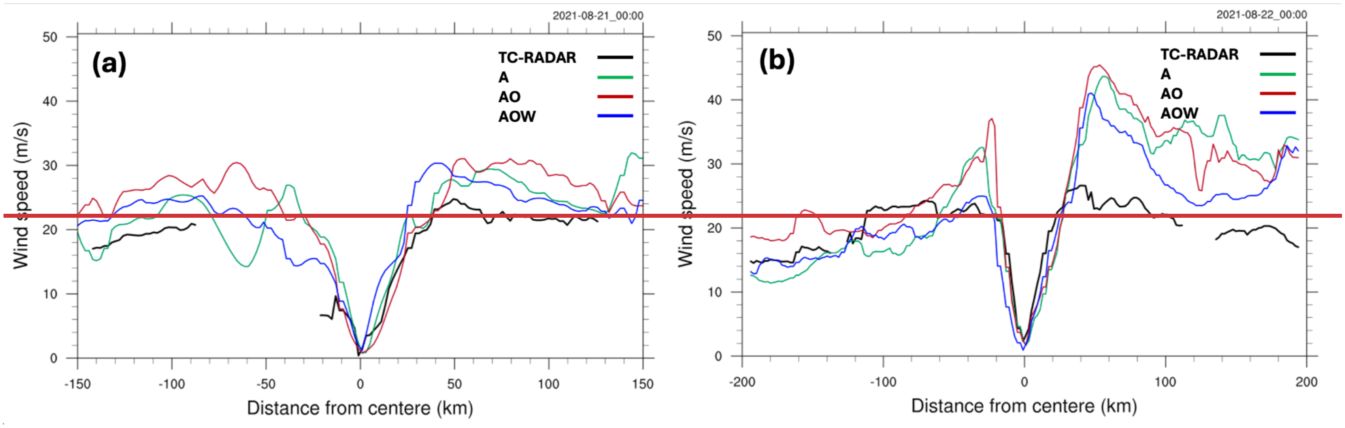

~~**Figure A1. Radial profiles of wind speed from the airborne Doppler radar and the three model simulations are shown in Figure 7 for (a) 00 UTC on 21st and (b) 22nd August 2021. The profiles are presented at the 1-km level along the line from A to B, as indicated in Figure 4.**~~

~~Appendix B: Averaged SST and surface enthalpy flux for 'AO' and 'AOW' in storm-centred coordinate~~

~~Figure B1 displays the time series of spatially- averaged SST and surface enthalpy flux in a 300 km x 300 km storm-centred coordinate. Both the time series reveal differences between the two coupled simulations, indicating that 'AOW' is associated with cooler SSTs that are closer to the observation, as well as lower surface enthalpy flux over the entire simulation period. This greater cooling of SSTs observed in 'AOW' partly explains the reduction in intensity. SST is reduced by the storm through wave-induced vertical mixing and vertical mixed layer depth bringing cold water upward, which in turn reduces TC intensification. Wang et al. (2024b) discussed wave-induced mixing primarily caused by wave breaking and non-breaking wave orbital motion (non-breaking wave). Through their comprehensive literature review, they suggested that wave breaking-induced mixing typically has a limited impact on SST and heat fluxes near the surface, and thus on TC intensity. In contrast,~~

~~non-breaking wave-induced mixing penetrates much deeper, enhancing vertical mixing and mixed-layer depth, which ultimately contributes to a greater reduction in TC intensification. Given this discussion, the inclusion of the non-breaking wave feature in ‘AOW’ may play an important role in moderating the thermal structure of the upper ocean, influencing the exchange of heat and moisture fluxes between the ocean and the atmosphere, and ultimately improving the intensity and structure of Henri.~~

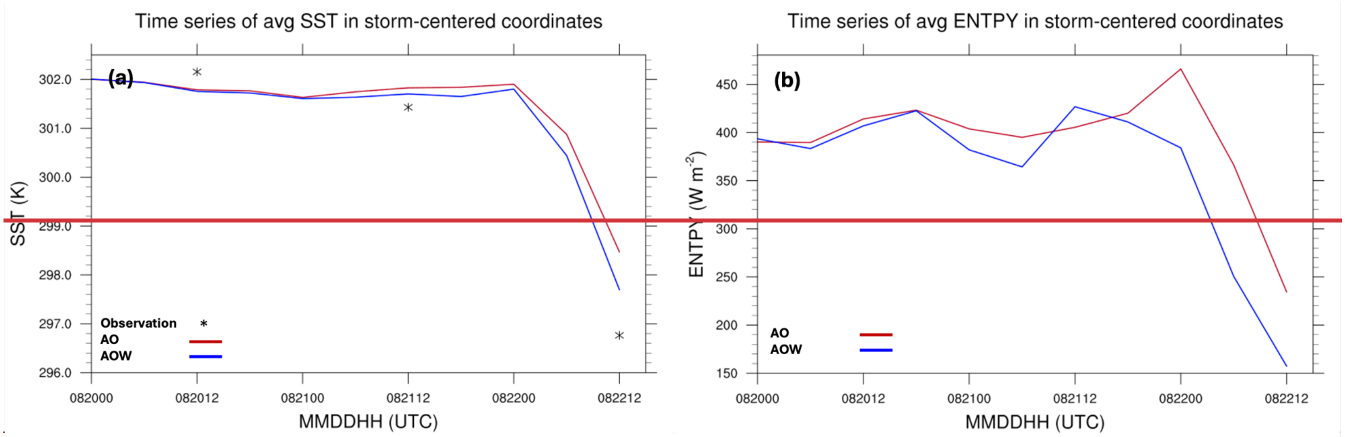

~~**Figure B1. Time series of spatial averaged (a) SST and (b) surface enthalpy flux in a 300 km × 300 km storm-centered coordinate. Data is derived from OSTIA observation (asterisks), experiment ‘AO’ (red lines), and experiments ‘AOW’ (blue lines).**~~

~~Appendix C: Simulated and observed surface wind direction and mean ocean wave direction~~

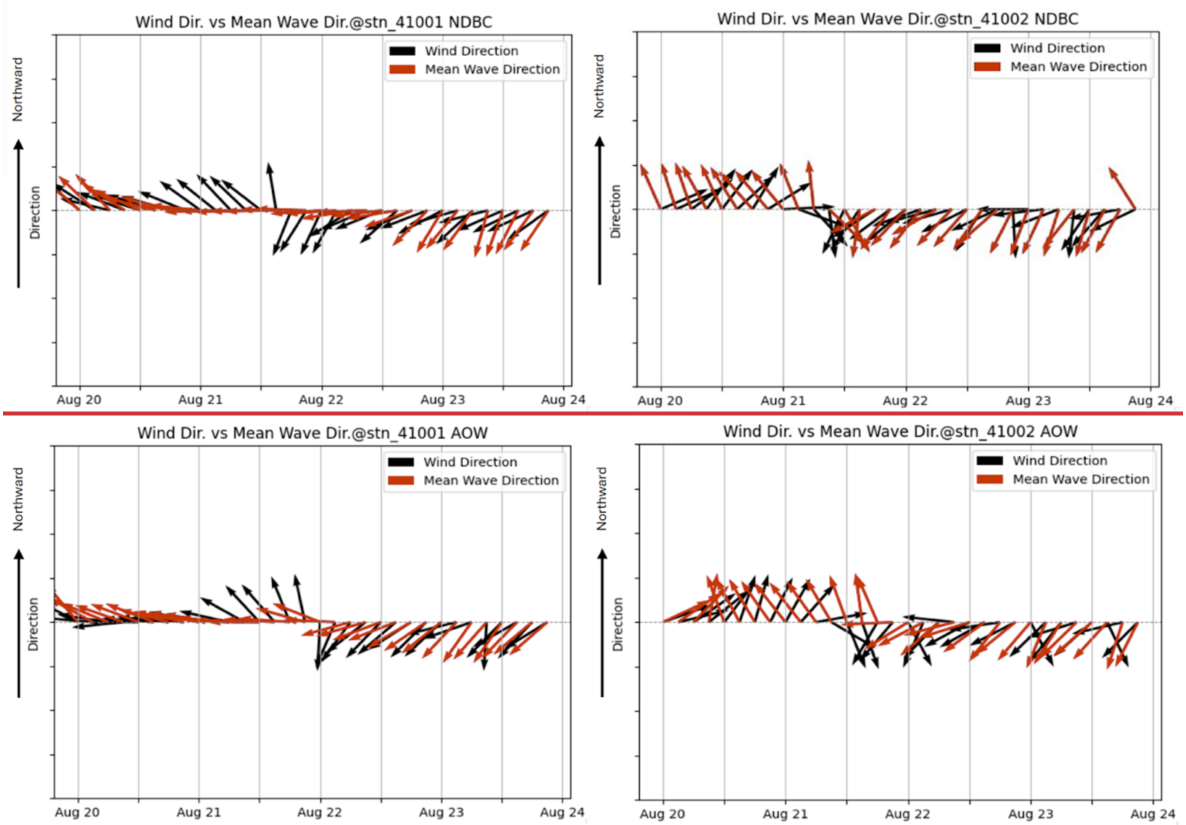

~~**Figure C1. Time series comparison of surface wind direction and mean ocean surface wave direction at two NDBC buoy stations, 41001 (left column) and 41002 (right column), derived from NDBC buoys (top panel) and experiment 'AOW' (bottom panel).**~~

Author contribution. Conceptualization, Formal analysis, Validation, Visualization: CJ, JW, PX, CH, WP; Data curation, Investigation, Software: CJ, JW, CH, MB, GN; Funding acquisition, Resources, Supervision: JW, PX, WP; Methodology: CJ, CH, WP; Project administration: JW, PX; Writing – original draft: CJ, JW, PX, WP; Writing – review & editing: CJ, JW, PX, CH, MB, GN.

Competing interests. The authors declare that they have no competing interests.

Acknowledgements. This study is supported by the Wind Energy Technologies Office (WETO) of the U.S. Department of Energy (DOE) Office of Energy Efficiency and Renewable Energy. The WRF model was made available by the National Center for Atmospheric Research, which is sponsored by NSF. High-Performance Computing support from the Theta cluster operated by Argonne Leadership Computing Facility (ALCF) and Kestrel operated by National Renewable Energy Laboratory (NREL).

References

Aijaz, S., Ghantous, M., Babanin, A. V., Ginis, I., Thomas, B., and Wake, G.: Nonbreaking wave-induced mixing in upper ocean during tropical cyclones using coupled hurricane-ocean-wave modeling, J. Geophysi. Res. 122(5), 3939–3963, 2017.

Akinsanola, A. A., Jung, C., Wang, J., & Kotamarthi, V. R.: Evaluation of precipitation across the contiguous United States, Alaska, and Puerto Rico in multi-decadal convection-permitting simulations, Scientific Reports, 14(1), 1238, 2024.

Arthur, W. C.: A statistical–parametric model of tropical cyclones for hazard assessment, Nat. Hazards Earth Syst. Sci., 21, 893–916, https://doi.org/10.5194/nhess-21-893-2021, 2021.

Barr, B. W. and Chen, S. S.: Impacts of seastate-dependent sea spray heat fluxes on tropical cyclone structure and intensity in fully coupled atmosphere-wave-ocean model simulations, Journal of Advances in Modeling Earth Systems, 17, e2024MS004550. https://doi.org/10.1029/2024MS004550, 2024.

Babanin, A. V.: On a wave-induced turbulence and a wave-mixed upper ocean layer, Geophys. Res. Lett. 33(20), 1–6, https://doi.org/10.1029/2006GL027308, 2006.

~~Bardal, L. M., Saetran, L. R., and Wangsness, E.: Performance test of a 3MW wind turbine – Effects of shear and turbulence, Energy Procedia, 80, 83–91. https://doi.org/10.1016/j.egypro.2015.11.410, 2015.~~

~~Bender, M. A., Ginis I., and Kurihara Y.: Numerical simulations of tropical cyclone–ocean interaction with a high-resolution coupled model, J. Geophys. Res., 98 , 23245–23263, 1993.~~

Booij, N., Ris, R. C., and Holthuijsen, L. H.: A third-generation wave model for coastal regions. Part I: Model description and validation, J. Geophys. Res., 104, 7649–7666, doi:10.1029/98JC02622, 1999.

Charnock, H., 1955: Wind stress on a water surface. Quart. J. Roy. Meteor. Soc., 81, 639–640.

~~Cavaleri, L., Fox-Kemper, B., and Hemer, M.: Wind waves in the coupled climate system, Bull. Amer. Meteor. Soc., 93, 1651–1661, https://doi.org/10.1175/BAMS-D-11-00170.1, 2012.~~

Chen, C., Liu, H., and Beardsley, R. C.: An unstructured grid, finite-volume, three-dimensional, primitive equations ocean model: Application to coastal ocean and estuaries, J. Atmos. Oceanic Technol., 20, 159–186, https://doi.org/10.1175/1520-0426(2003)020<0159:AUGFVT>2.0.CO;2, 2003.

Chen, C., Beardsley, R. C., and Cowles, G.: An unstructured grid, finite-volume coastal ocean model: FVCOM user manual, Tech. Rep. SMAST/UMASSD-13-0701, 416 pp, 2013.

~~Chen, F., and Dudhia, J.: Coupling an advanced land-surface/ hydrology model with the Penn State/ NCAR MM5 modeling system. Part I: Model description and implementation, Mon. Wea. Rev., 129, 569-585, 2001.~~

Chen, P., Zhang, Z., Li, Y., Ye, R., Li, R., and Song, Z.: The two-parameter Holland Pressure Model for tropical cyclones, J. Mar. Sci. Eng. 2024, 12(1), 92; https://doi.org/10.3390/jmse12010092, 2024.

Chen, S. S., Price, J. F., Zhao, W., Donelan, M. A., and Walsh, E. J.: The CBLAST-hurricane program and the next-generation fully coupled atmosphere–wave–ocean models for hurricane research and prediction, Bull. Am. Meteorol. Soc. 88(3), 311–318, 2007.

Chen, S. S., Zhao, W., Donelan, M. A., and Tolman, H. L.: Directional wind–wave coupling in fully coupled atmosphere–wave–ocean models: Results from CBLAST-Hurricane, J. Atmos. Sci. 70(10), 3198–3215, 2013.

~~Churchfield, M. J., and Sirnivas, S.: On the effects of wind turbine wake skew caused by wind veer, In 2018 wind energy symposium. American Institute of Aeronautics and Astronautics. https://doi.org/10.2514/6.2018-0755, 2018.~~

~~Cione, J. J., and Uhlhorn, E. W.: Sea surface temperature variability in hurricanes: Implications with respect to intensity change, Mon. Wea. Rev., 131, 1783–1796, 2003.~~

~~Craig, P. D. and Banner, M. L.: Modeling wave-enhanced turbulence in the ocean surface layer, J. Phys. Oceanogr. 24(12), 2546–2559, 1994.~~Craig, A., Valcke, S., and Coquart, L.: Development and performance of a new version of the OASIS coupler, OASIS3-MCT_3.0, Geosci. Model Dev., 10, 3297–3308, https://doi.org/10.5194/gmd-10-3297-2017, 2017.

Creasey, R. L., and Elsberry, R. L.: Tropical cyclone center positions from sequences of HDSS sondes deployed along high-altitude overpasses. Wea. Forecasting, 32, 317–325, https://doi.org/10.1175/WAF-D-16-0096.1, 2017.

~~Craig, A., Valcke, S., and Coquart, L.: Development and performance of a new version of the OASIS coupler, OASIS3-MCT_3.0, Geosci. Model Dev., 10, 3297–3308, https://doi.org/10.5194/gmd-10-3297-2017, 2017.~~

Cummings, J. A. and Smedstad, O.M.: Ocean data impacts in global HYCOM, J. Atmos. Ocean. Technol., 31 (8), pp. 1771-1791, 10.1175/JTECH-D-14-00011.1, 2014.

DeMaria, M.,Knaff, J. A., and Sampson, C.: Evaluation of long-term trends in tropical cyclone intensity forecasts, Meteor. Atmos. Phys., 97, 19–28, 2007.

DeMaria, M., Sampson, C. R., Knaff, J. A., & Musgrave, K. D.: Is tropical cyclone intensity guidance improving? Bulletin of the American Meteorological Society, 95(3), 387–398. https://doi.org/10.1175/bams-d-12-00240.1, 2014.

Donelan, M. A. et al. On the limiting aerodynamic roughness of the ocean in very strong winds. Geophys. Res. Lett. 31, L18306, 10.1029/2004GL019460, 2004.

Drennan, W. M.; Graber, H. C.; Hauser, D.; Quentin, C. On the wave age dependence of wind stress over pure wind seas, J. Geophys. Res. Oceans, 108, 8062, 2003.

Drennan, W. M., Taylor, P. K., and Yelland, M. J., "Parameterizing the sea surface roughness," J. Phys. Oceanogr. 35(5), 835–848, 2005.

Dyer, A. J., and Hicks, B. B.: Flux-gradient relationships in the constant flux layer, Quart. J. Roy. Meteor. Soc., 96, 715–721, 1970.

Emanuel, K. A.: An air-sea interaction model of the tropical cyclones. Part I: Steady-State Maintenance, Journal of the Atmospheric Sciences, 43(6), 585-605. https://doi.org/10.1175/1520-0469(1986)043<0585:AASITF>2.0.CO;2, 1986.

~~Englberger, A., and Lundquist, J. K.: How does wind veer affect the veer of a wind-turbine wake? Journal of Physics: Conference Series, 1452 (2020) 012068, doi:10.1088/1742-6596/1452/1/012068, 2020.~~

Fan, Y., Ginis, I., and Hara, T.: The effect of wind–wave–current interaction on air–sea momentum fluxes and ocean response in tropical cyclones, J. Phys. Oceanogr., 39, 1019–1034, 2009.

~~Fan, Y., Ginis, I., and Hara, T.: Momentum flux budget across air–sea interface under uniform and tropical cyclone winds, J. Phys. Oceanogr., 40, 2221–2242, 2010.~~

Fischer, M. S., Reasor, P. D., Rogers, R. F., and Gamache, J. F.: An analysis of tropical cyclone vortex and convective characteristics in relation to storm intensity using a novel airborne doppler radar database, Monthly Weather Review, 150 (9), 2255 – 2278, https://doi.org/https: //doi.org/10.1175/MWR-D-21-0223.1, 2022

~~Gao, L., Li, B., and Hong, J.: Effect of wind veer on wind turbine power generation, Physics of Fluids, 33(1), 015101. https://doi.org/10.1063/5.0033826, 2021.~~

Gentry, M. S., and Lackmann, G. M.: Sensitivity of simulated tropical cyclone structure and intensity to horizontal resolution, Mon. Wea. Rev., 138, 688–704, 2010.

Ghantous, M., and Babanin, A. V.: One-dimensional modeling of upper ocean mixing by turbulence due to wave orbital motion, Nonlinear Proc. Geophys., 21(1), 325–338, doi:10.5194/npg-21-325-2014, 2014a.

Ghantous, M., and Babanin, A. V.: Ocean mixing by wave orbital motion. Acta Physica Slovaca, 64(1), 1–57, doi:10.2478/apsrt-2014-0001, 2014b.

Good, S., Fiedler, E., Mao, C., Martin, M. J., Maycock, A., Reid, R., Roberts-Jones, J., Searle, T., Waters, J., While, J., and Worsfold, M.: The current configuration of the OSTIA system for operational production of foundation sea surface temperature and ice concentration analyses, Remote Sens. 12, 720, doi:10.3390/rs12040720, 2020.

Hong, S.-Y. and Lim, J.-O.: The WRF single-moment 6-class microphysics scheme (WSM6), J. Korean Meteor. Soc., 42, 129-151, 2006.

Hong, S.-Y., Noh, Y., and Dudhia, J.: A new vertical diffusion package with an explicit treatment of entrainment processes, Mon. Wea. Rev., 134, 2318-2341, 2006.

Iacono, M. J., Delamere, J. S., Mlawer, E. J., Shephard, M. W., Clough, S. A., and Collins, W. D.: Radiative forcing by long-lived greenhouse gases: Calculations with the AER radiative transfer models, J. Geophys. Res., 113, D13103, 2008.

IEC: Wind turbines - part 1: Design requirements (No. IEC 61400-1:2019), 2019a.

IEC: Wind turbines – part 3: Design requirements for offshore wind turbines (No. IEC 61400-3-1:2019), 2019b

Itiki, R., Manjrekar, M., Di Santo, S. G., Itiki, C.: Method for spatiotemporal wind power generation profile under hurricanes: US-Caribbean super grid proposition, Renew. Sust. Energ. Rev., 173, Article 113082, 2023.

Jimenez, P., Dudhia, J. , Gonzalez-Ruoco, J. F., Navarro, J., Montavez, J. P., and Garcia-Bustamente, E.: A revised scheme for the WRF surface layer formulation, Mon. Wea.Rev., 140, 898–918, 2012.

~~Kapoor, A., Ouakka, S., Arwade, S. R., Lundquist, J. K., Lackner, M. A., Myers, A. T., Worsnop, R. P., and Bryan, G. H.: Hurricane eyewall winds and structural response of wind turbines, Wind Energy Sci., 5, 89-104, https://doi.org/10.5194/wes-5-89-2020, 2020.~~

Knapp, K. R., Kruk, M. C., Levinson, D. H., Diamond, H. J., and Neumann, C. J.: The international best track archive for climate stewardship (ibtracs) unifying tropical cyclone data. Bulletin of the American Meteorological Society, 91 (3), 363–376, 2010.

~~Knutson, T. and Coauthors: Tropical cyclones and climate change, Nature Geoscience, 3(3), 157-163. https://doi.org/10.1038/ngeo779, 2010.~~

~~Knutson, T., and Coauthors: Tropical cyclones and climate change assessment: Part I: Detection and attribution, Bull Amer. Meteor. Soc., 100, 1987–2007, https://doi.org/10.1175/BAMS-D-18-0189.1, 2019.~~

~~Knutson, T., and Coauthors: Tropical cyclones and climate change assessment: Part II: Projected response to anthropogenic warming, Bull. Amer. Meteor. Soc., 101, E303–E322, https://doi.org/10.1175/BAMS-D-18-0194.1, 2020~~

Komen, G. J., Hasselmann K. , and Hasselmann K.: On the existence of a fully developed wind-sea spectrum, J. Phys. Oceanogr., 14, 1271–1285, doi:10.1175/1520-0485(1984)014<1271:OTEOAF>2.0.CO;2, 1984.

Kouadio, K., Bastin, S., Konare, A., and Ajayi, V. O.: Does convection-permitting simulate better rainfall distribution and extreme over Guinean coast and surroundings? Climate Dynamics, 55, 153–174. https://doi.org/10.1007/s00382-018-4308-y, 2020.

Ma, T. and Sun, C.: Large Eddy Simulation of Combined Wind-wave Loading on Offshore Wind Turbines, arXiv [preprint], arXiv:2310.03407, 2023.

~~Lane, E. M., Restrepo, J. M., and McWilliams, J. C.: Wave–current interaction: A comparison of radiation-stress and vortex-force, J. Phys. Oceanogr. 37, 1122–1141, 2007.~~

~~Li, X., Pu, Z., and Gao, Z.: Effects of roll vortices on the evolution of hurricane harvey during landfall, J. Atmos. Sci., 76, 1847–1867, https://doi.org/10.1175/JAS-D-20-0270.1, 2021.~~

~~Liu, J., Curry, J. A., Clayson, C. A., and Bourassa, M. A.: High-resolution satellite surface latent heat fluxes in North Atlantic hurricanes, Mon. Wea. Rev., 139, 2735–2747, 2011.~~

Madsen, O. S., Poon, Y. K., and Graber, H. C.: Spectral wave attenuation by bottom friction: Theory, Proceedings of the International Conference on Coastal Engineering, No. 21, 492-506, 1988.

Mellor, G.: On theories dealing with the interaction of surface waves and ocean circulation, J. Geophys. Res. 121(7), 4474–4486, https://doi.org/10.1002/2016JC011768, 2016.

~~Mogensen, K. S., Magnusson, L., and Bidlot, J.-R.: Tropical cyclone sensitivity to ocean coupling in the ECMWF coupled model, J. Geophys. Res. Oceans, 122, 4392–4412, https://doi.org/10.1002/2017JC012753, 2017.~~

~~Montgomery, M. T., and Smith, R. K.: Paradigms for tropical cyclone intensification, Australian Meteorological and Oceanographic Journal, 64, 37–66. https://doi.org/10.22499/2.6401.005, 2014.~~

~~Müller, S., Larsén, X. G., and Verelst, D. R.: Tropical cyclone low-level wind speed, shear, and veer: sensitivity to the boundary layer parameterization in the Weather Research and Forecasting model, Wind Energ. Sci., 9, 1153–1171, https://doi.org/10.5194/wes-9-1153-2024, , 2024.~~

~~Murphy, P., Lundquist, J. K., and Fleming, P.: How wind speed shear and directional veer affect the power production of a megawatt-scale operational wind turbine, Wind Energ. Sci., 5, 1169–1190, 2020 https://doi.org/10.5194/wes-5-1169-2020, 2020.~~

Nakanishi, M. and Niino, H.: Development of an improved turbulence closure model for the atmospheric boundary layer, J. Meteor. Soc. Japan, 87, 895–912, doi:http://dx.doi.org/10.2151/jmsj.87.895, 2009.

National Data Buoy Center (NDBC), NOAA: National Data Buoy Center (NDBC) Moored Buoy and C-MAN Station Data, UCAR/NCAR - Earth Observing Laboratory, DOI: https://doi.org/10.26023/V640-H29S-MR0S, 2008.

National Centers for Environmental Prediction (NCEP), National Weather Service, NOAA: U.S. Department of Commerce, Research Data Archive at the National Center for Atmospheric Research, Computational and Information Systems Laboratory, https://doi.org/10.5065/D65D8PWK, 2015.

~~Olabarrieta, M., Medina, R., and Castanedo, S.: Effects of wave-current interaction on the current profile, Coastal Eng. 57(7), 643–655, 2010.~~

Olson, J. B., Kenyon, J. S., Angevine, W. M., Brown, J. M., Pagowski, M., and Sušelj, K.: A description of the MYNN-EDMF scheme and coupling to other components in WRF-ARW, NOAA Tech. Memo. OAR GSD, 61, 37 pp., https://doi.org/10.25923/n9wm-be49, 2019.

Paulson, C. A.: The mathematical representation of wind speed and temperature profiles in the unstable atmospheric surface layer, J. Appl. Meteor., 9, 857–861, 1970.

Powell, M. D., Vickery, P. J. & Reinhold, T. A. Reduced drag coefficient for high wind speeds in tropical cyclones. Nature 422, 279–283, 2003.

Prein, A. F., Langhans, W., Fosser, G., Ferrone, A., Ban, N., Goergen, K., Keller, M., Tölle, M., Gutjahr, O., Feser, F., et al.: A review on regional convection-permitting climate modeling: Demonstrations, prospects, and challenges, Reviews of Geophysics, 53, 323–361, https://doi.org/10.1002/2014RG000475, 2015.

~~Perrie, W., Ren, X., Zhang, W., and Long, Z.: Simulation of extratropical Hurricane Gustav using a coupled atmosphere-ocean-sea spray model, Geophys. Res. Lett. 31(3), L03110, https://doi.org/10.1029/2003GL018571, 2004.~~

~~Perrie, W., Andreas, E. L., Zhang, W., Li, W., Gyakum, J., and McTaggart-Cowan, R.: Sea spray impacts on intensifying midlatitude cyclones, J. Atmos. Sci. 62(6), 1867–1883, 2005.~~

~~Prakash, K. R., Pant, V., and Nigam, T.: Effects of the sea surface roughness and sea spray-induced flux parameterization on the simulations of a tropical cyclone, J. Geophys. Res. 124(24), 14037–14058, https://doi.org/10.1029/2018JD029760, 2019.~~

Pringle, W. J. and Kotamarthi, V. R.: Coupled ocean wave-atmosphere models for offshore wind energy. Argonne, IL. https://doi.org/10.2172/1829093, 2021.

~~Qiao, F., Yuan, Y., Yang, Y., Zheng, Q., Xia, C., and Ma, J.: Wave-induced mixing in the upper ocean: Distribution and application to a global ocean circulation model, Geophys. Res. Lett. 31(11), L11303, https://doi.org/10.1029/2004GL019824, 2004.~~

Qing, Y. and Wang, S.: Multi-decadal convection-permitting climate projections for China’s Greater Bay Area and surroundings, Clim Dyn. https://doi.org/10.1007/s00382-021-05716-w, 2021.

Rappaport, E. N., and Coauthors: Advances and challenges at the National Hurricane Center, Wea. Forecasting, 24, 395–419, 2009.

~~Richter, D. H. and Stern, D. P.: Evidence of spray-mediated air-sea enthalpy flux within tropical cyclones, Geophys. Res. Lett. 41(8), 2997–3003, https://doi.org/10.1002/2014GL059746, 2014.~~

~~Robertson, A. N., Shaler, K., Sethuraman, L., and Jonkman, J.: Sensitivity analysis of the effect of wind characteristics and turbine properties on wind turbine loads, Wind Energy Science, 4(3), 479–513. https://doi.org/10.5194/wes-4-479-2019, 2019.~~

Roldán M., Montoya R. D., Rios J. D., Osorio A. F.: Modified parametric hurricane wind model to improve the asymmetry in the region of maximum winds, Ocean Eng. 280, 114508. doi: 10.1016/j.oceaneng.2023.114508, 2023.

~~Sanchez Gomez, M., and Lundquist, J. K.: The Effects of Wind Veer During the Morning and Evening Transitions, Journal of Physics: Conference Series, 1452 (2020) 012075, doi:10.1088/1742-6596/1452/1/012075, 2020.~~

Sanchez Gomez, M., Lundquist, J. K., Mirocha, J. D., and Arthur, R. S.: Investigating the physical mechanisms that modify wind plant blockage in stable boundary layers, Wind Energ. Sci., 8, 1049–1069, https://doi.org/10.5194/wes-8-1049-2023, 2023.

Shanahan, T. and Fitzgerald, B.: Wind–Wave Misalignment in Irish Waters and Its Impact on Floating Offshore Wind Turbines. Energies, 18(2), 372; https://doi.org/10.3390/en18020372, 2025.

Shimura, T., Noh, Y., and Hara, T.: Long-term impacts of ocean wave-dependent roughness on global climate systems, J. Geophy. Reasrch: Oceans, 122(3), 1995-2011, https://doi.org/10.1002/2016JC012621, 2017.

~~Schade, L. R., and Emanuel K. A.: The ocean's effect on the intensity of tropical cyclones: Results from a simple coupled atmosphere–ocean model, J. Atmos. Sci., 56, 642–651, 1999.~~

Skamarock, W.C., Klemp, J.B., Dudhia, J., Gill, D.O., Liu, Z., Berner, J., Wang, W., Powers, J.G., Duda, M.G., and Barker, D.M.: A description of the advanced research WRF model version 4; National Center for Atmospheric Research: Boulder, CO, USA, 2019; p. 145, 2019.

Smagorinsky, J.: General circulation experiments with the primitive equations, part I: the basic experiment Monthly Weather Review, 91 (1963), pp. 99-164, 1963.

~~Smith, J. A.: Wave–current interactions in finite depth, J. Phys. Oceanogr. 36(7), 1403–1419, 2006.~~

~~Smith, R. K., Montgomery, M. T., and Van Sang, N.: Tropical cyclone spin-up revisited. Quarterly Journal of the Royal Meteorological Society, 135(642), 1321–1335. https://doi.org/10.1002/qj.428, 2009.~~

Smith, A. B.: 2010–2019: A landmark decade of U.S. billion-dollar weather and climate disasters. NOAA, https://www.climate.gov/news-features/blogs/beyond-data/2010-2019-landmark-decade-us-billion-dollar-weather-and-climate, 2020.

~~Stull, R. B.: An Introduction to Boundary Layer Meteorology, Kluwer, Dordrecht, https://doi.org/10.1007/978-94-009-3027-8, 1988.~~

~~Sullivan, P. P. and McWilliams, J. C.: Dynamics of winds and currents coupled to surface waves, Annu. Rev. Fluid Mech. 42(1), 19–42, 2010.~~

Sun, X., Xue, M., Brotzge, J., McPherson, R. A., Hu, X.-M., and Yang, X.-Q.: An evaluation of dynamical downscaling of Central Plains summer precipitation using a WRF-based regional climate model at a convection-permitting 4 km resolution, Journal of Geophysical Research: Atmosphere, 121, 13801–13825. https://doi.org/10.1002/2016JD024796, 2016.

Taylor, P. K., and Yelland, M. J.: The dependence of sea surface roughness on the height and steepness of the waves, J. Phys. Oceanogr., 31, 572–590, 2001.

Wada, A. and Usui, N.: Impacts of oceanic preexisting conditions on predictions of Typhoon Hai-Tang in 2005, Advances in Meteorology, 2010, 756071, 2010.

~~Tsartsali, E. E., Haarsma, R. J., Athanasiadis, P. J., Bellucci, A., de Vries, H., Drijfhout, S., de Vries, I. E., Putrahasan, D., Roberts, M. J., Sanchez Gomez, E., and Roberts, C. D.: Impact of resolution on the atmosphere–ocean coupling along the Gulf Stream in global high resolution models, Clim. Dyn. 58(11–12), 3317–3333, 2022.~~

~~Wada, A. and Usui, N.: Impacts of oceanic preexisting conditions on predictions of Typhoon Hai-Tang in 2005, Adv. Meteorol. 2010, 756071, 2010.~~

~~Walsh, K. J. E., and Coauthors: Hurricanes and climate: The U.S. CLIVAR working group on hurricanes, Bull. Amer. Meteor. Soc., 96(6), 997−1017, https://doi.org/10.1175/BAMS-D-13-00242.1, 2015.~~

~~Walsh, K. J. E., and Coauthors: Tropical cyclones and climate change, WIREs Climate Change, 7, 65−89, https://doi.org/10.1002/wcc.371, 2016.~~

~~Wang, J., Deskos, G., Pringle, W. J., Haupt, S. E., Feng, S., Berg, L. K., Churchfield, M., Biswas, M., Musial, W., Muradyan, P., Hendricks, E., Kotamarthi, R., Xue, P., Rozoff, C. M., and Bryan, G.: Impact of tropical and extratropical cyclones on future U.S. offshore wind energy. Bulletin of the American Meteorological Society, 1506–1513. https://doi.org/10.1175/bams-d-24-0080.1, 2024a.~~

~~Wang, J., Hendricks, E., Rozoff, C. M., Churchfield, M., Zhu, L., Feng, S., Pringle, W. J., Biswas, M., Haupt, S. E., Deskos, G., Jung, C., Xue, P., Berg, L. K., Bryan, G., Kosovic, B., and Kotamarthi, R.: Modeling and observations of North Atlantic cyclones: Implications for U.S. Offshore wind energy. Journal of Renewable and Sustainable Energy, 16(052702). https://doi.org/10.1063/5.0214806, 2024b.~~

Warner J. C., Armstrong, B., He, R., Zambon, J. B.: Development of a coupled ocean–atmosphere–wave–sediment transport (COAWST) modeling system. Ocean Model 35:230–244. doi:10.1016/j.oceanmod.2010.07.010, 2010.

Webb, E. K.: Profile relationships: The log-linear range, and extension to strong stability, Quart. J. Roy. Meteor. Soc., 96, 67–90, 1970.

Wei, J., Jiang, GQ., and Liu, X.: Parameterization of typhoon-induced ocean cooling using temperature equation and machine learning algorithms: an example of typhoon Soulik (2013), Ocean Dynamics 67, 1179–1193. https://doi.org/10.1007/s10236-017-1082-z, 2017.

Wright, C. W., and Coauthors: Hurricane directional wave spectrum spatial variation in the open ocean, J. Phys. Oceanogr., 31, 2472–2488, 2001.

Wu, L., Rutgersson, A., Sahlée, E., and Guo Larsén, X.: Swell impact on wind stress and atmospheric mixing in a regional coupled atmosphere-wave model, Journal of Geophysical Research: Oceans, 121, 4633–4648. https://doi.org/10.1002/2015JC011576, 2016.

Xu, X., Voermans, J. J., Zhang, W., Zhao, B., Qiao, F., Liu, Q., Moon, I.-J., Janekovic, I., Waseda, T., and Babanin, A. V.: Tropical cyclone modeling with the inclusion of wave-coupled processes: sea spray and wave turbulence, Geophys. Res. Lett., 50, e2023GL106536, https://doi.org/10.1029/2023GL106536, 2023.

~~Yablonsky, R. M., and Ginis, I.: Limitation of one-dimensional ocean models for coupled hurricane–ocean model forecasts, Mon. Wea. Rev., 137, 4410–4419, doi:10.1175/2009MWR2863.1, 2009.~~

~~Y~~Yamaguchi, M., Ishida, J., Sato, H., and Nakagawa, M.: WGNE intercomparison of tropical cyclone forecasts by operational nwp models: A quarter century and beyond, Bulletin of the American Meteorological Society, 98(11), 2337–2349. https://doi.org/10.1175/bams-d-16-0133.1, 2017.

Zambon, J. B., He, R., and Warner, J. C.: Investigation of Hurricane Ivan using the coupled ocean–atmosphere–wave–sediment transport (COAWST) model, Ocean Dynamics, 64(11), 1535–1554. https://doi.org/10.1007/s10236-014-0777-7, 2014.

Zambon, J. B., He, R., Warner, J. C., and Hegermiller, C. A.: Impact of SST and surface waves on Hurricane Florence (2018): A coupled modeling investigation. Weather and Forecasting, 36(5), 1713–1734. https://doi.org/10.1175/WAF-D-20-0171.1, 2021.

Zhang, J. A. and Marks, F. D.: Effects of horizontal diffusion on tropical cyclone intensity change andXd structure in idealized three-dimensional numerical simulations, Monthly Weather Review, 143, 3981–3995, https://doi.org/10.1175/mwr-d-14-00341.1, 2015.

Zhang, S., Yuan, Y., and Zheng, Q.: Modeling of the eddy viscosity by breaking waves, Acta Oceanol. Sin. 26(6), 116–123, 2007.

Zhang, S., Xu, S., Fu, H., Wu, L., Liu, Z., Gao, Y. et al.: Toward earth system modeling with resolved clouds and ocean submesoscales on heterogeneous many-core HPCs, Nat. Sci. Rev. 10(6), nwad069, 2023.

~~Zhao, B., Wang, G., Zhang, J. A., Liu, L., Liu, J., Xu, J., et al.: The effects of ocean surface waves on tropical cyclone intensity: Numerical simulations using a regional atmosphere-ocean-wave coupled model, Journal of Geophysical Research: Oceans, 127, e2022JC019015. https://doi.org/10.1029/2022JC019015, 2022.~~

Zhao, B., Qiao, F., Cavaleri, L., Wang, G., Bertotti, L., and Liu, L.: Sensitivity of typhoon modeling to surface waves and rainfall. Journal of Geophysical Research: Oceans, 122(3), 1702–1723. https://doi.org/10.1002/2016jc012262, 2017.

Zhao, B., Wang, G., Zhang, J. A., Liu, L., Liu, J., Xu, J., et al.: The effects of ocean surface waves on tropical cyclone intensity: Numerical simulations using a regional atmosphere-ocean-wave coupled model, Journal of Geophysical Research: Oceans, 127, e2022JC019015. https://doi.org/10.1029/2022JC019015, 2022.

Zhou, X., Hara, T., Ginis, I., D'Asaro, E., and Reichl, B. G.: Evidence of langmuir mixing effects in the upper ocean layer during tropical cyclones using observations and a coupled wave-ocean model, Journal of Geophyiscal Research, 2(10), ttps://doi.org/10.1029/2023JC020062, 2023.

~~Zhu, T., and. Zhang, D.-L: The impact of the storm-induced SST cooling on hurricane intensity, Adv. Atmos. Sci., 23, 14–22, 2006.~~